ALMA MATER STUDIORUM
UNIVERSITÀ DI BOLOGNA

Facoltà di Scienze M.F.N.
Scuola di Dottorato in Scienze Matematiche, Fisiche ed Astronomiche
Dipartimento di Astronomia

UNIVERSIDAD DE CANTABRIA

Facultad De Ciencias
Departamento de Física Moderna

PhD Thesis

Origin and Nature of Radio-Loud Broad Absorption Line Quasars

A multi-wavelength study

Gabriele Bruni

DOTTORATO DI RICERCA IN ASTRONOMIA - Ciclo XXIV
Settore Concorsuale di afferenza: 02/C1
Settore Scientifico disciplinare: FIS/05

PhD COORDINATOR: Prof. Lauro Moscardini
ADVISORS: Prof. Daniele Dallacasa
Prof. José Ignacio González-Serrano
SUPERVISOR: Dott. Karl-Heinz Mack

Esame Finale Anno 2012

This thesis work has been done under the joint PhD program between the Università di Bologna and the Universidad de Cantabria.

This research has been carried out as part of the activities of the Istituto di Radioastronomia (INAF-Bologna, Italy) and of the Instituto de Física de Cantabria (IFCA-Santander, Spain)

Contents

Summary

The origin of Broad Absorption Line Quasars (BAL QSOs) is still an open issue. Accounting for $\sim$ 20% of the QSO population, these objects present broad absorption lines in their optical spectra generated from outflows with velocities up to 0.2 c. There is still no consensus about the origin of the absorbing gas in BAL QSOs, the mechanism which accelerates it, or the relationship between BAL QSOs and the quasar population as a whole.

Nowadays, the hypotheses about their nature are principally related to orientation or evolutionary scenarios. In the first one, absorption lines are produced by outflows originated by the accretion disk, basically present in all QSOs, but seen only when they intercept the line of sight. In the second hypothesis, BAL QSOs would be young or recently re-fueled QSOs, still ejecting their dust cocoon. In this case orientation would not play a role, since the absorption features would be produced by spherically ejected matter.

In this work we present the results of a multi-frequency study of a Radio-Loud BAL QSO sample, and a comparison sample of Radio-Loud non-BAL QSOs, both selected from the Sloan Digital Sky Survey (SDSS). We performed observations in the radio band, to sample the SED in the GHz range and study the characteristics of the synchrotron emission, aiming at collecting indications about the age and the orientation of the central radio source, as well as the polarisation properties. The comparison with the non-BAL QSO sample allows us to conclude that no particular orientation is present in BAL QSOs. Nevertheless, similar fractions of GHz-peaked sources in the two sample (36$\pm$12% *vs* 23$\pm$8%) does not seem to suggest a young age for BAL QSOs, and this conclusion is favoured by the presence, in some cases, of low-frequency, presumably old components in the radio spectrum.

Through the VLBI technique, it was possible to study the pc-scale radio-morphology of half the sample. About 80% of sources present a resolved structure, with projected linear sizes comprised between tens and hundreds of pc. This fraction is comparable with previous results from literature. The missing flux density with respect to observations at kpc-scale resolution suggests a low frequency, diffuse component in some cases. The variety of morphologies does not support a particular orientation.

We also investigated the dust grey-body emission at mm-wavelengths, to verify whether BAL QSOs are dust-rich, physical condition requested by the evolutionary model. Only 7% of the sources present a clear dust contribution at 250 GHz. Not being dust rich, BAL QSOs should not present an high star-

formation rate. Thus, again, they should not be a particularly young class of objects.

Finally, using a sample of optically-bright Radio-Loud and Radio-Quiet QSOs, we collected spectra in the Near-Infrared band, to estimate the central black hole mass, the Eddington ratio, and the Broad Line Region radius, in order to underline differences induced by the Radio-Loud phase. From an analysis of the SDSS DR7 QSO catalogue, the Eddington ratio is the only physical quantity found to be significantly different in Radio-Loud BAL QSOs, 26% of these objects being super-Eddington, while only 13% of Radio-Quiet BAL QSOs show the same property. Even a bigger difference has been found between BAL and non-BAL QSOs as a whole (13% *vs* 2%).

Resumen

El origen de los cuásares con líneas anchas de absorción (BAL QSOs, del acrónimo en inglés Broad Absorption Line Quasars) es un tema todavía en discusión. Representando aproximadamente un 20% de la población de QSOs, estos objetos muestran líneas de absorción muy anchas en su espectro óptico/UV que están generadas por flujos de material que emerge con velocidades de hasta $0.2c$. No existe consenso sobre el origen de este gas causante de las absorciones, ni del mecanismo que lo acelera, o de la relación entre los cuásares BAL y el resto de la población de cuásares.

Actualmente, las hipótesis sobre su naturaleza están relacionadas principalmente con la orientación o con escenarios evolutivos. En la primera, las líneas de absorción estarían producidas por flujos emergentes originados en el disco de acrecimiento asociado al agujero negro central del QSO, pero que se observarían solamente cuando interceptan la línea de visión. En un escenario evolutivo, sin embargo, los cuásares BAL serían objetos jóvenes o re-abastecidos que todavía estarían expeliendo su envoltura de gas y polvo. En este caso, la orientación no jugaría ningún papel y las absorciones estarían producidas por materia eyectada radialmente.

En este trabajo se presentan los resultados de un estudio multifrecuencia de una muestra de cuásares BAL emisores en radio. Se ha seleccionado una muestra de comparación de cuásares no-BAL emisores en radio también. Ambas muestras se han seleccionado a partir del Sloan Digital Sky Survey (SDSS). Se han realizado observaciones en radio de ambas muestras, para estudiar su distribución espectral de energía (SED) en el rango del GHz y estudiar las características de la emisión sincrotrón. El objetivo es obtener estimaciones de la edad de la radiofuente, la orientación de la radiofuente central, y obtener medidas de polarización.

La comparación con la muestra de objetos no-BAL nos permite concluir que no existe una orientación preferida o predominante en los cusáres BAL. Por otro lado, sin embargo, la fracción similar de fuentes con pico en 1 GHz ($36 \pm 12\%$ vs. $24 \pm 8\%$) no parece sugerir que los BALs sean más jóvenes. Esta conclusión está apoyada por la presencia, en algunos casos, de componentes de baja frecuencia, supuestamente viejas, en sus radio espectros.

Utilizando técnicas VLBI (Very Large Baseline Interferometry) ha sido posible estudiar asímismo la morfología, a la escala del parsec, de la mitad de la muestra. Sobre un 80% de las fuentes observadas muestran estructura resuelta con tamaños proyectados de entre decenas y centenares de parsecs.

Esta fracción es comparable con otros resultados de otros autores. La variedad de morfologías observada no parece apoyar la idea de orientaciones preferentes.

Se investigó también en este trabajo la emisión de cuerpo gris a longitudes de onda milimétricas con el fin de determinar si los cuásares BAL pudieran ser ricos en polvo, requisito indispensable para apoyar un escenario evolutivo. Solamente un 7% de las fuentes observadas presentan una clara contribución por polvo a 250 GHz. Al no ser ricos en polvo, los cuásares BAL no deberían presentar un alto ritmo de formación estelar, así pues, concluimos que no deben ser una clase de objetos particularmente jóvenes.

Finalmente, se han estudiado dos muestras de BALs, brillantes en el rango óptico, la primera consistente en cuásares emisores en radio y la segunda, de comparación, en objetos no emisores en radio. Se obtuvieron espectros en el infrarrojo cercano para estimar la masa del agujero negro central, sus luminosidades, sus cocientes de Eddington, el tamaño de la Broad Line Region (BLR) con el fin de buscar diferencias que podrían estar inducidas en la fase de radioemisión. Después de este análisis y junto con un análisis del catálogo SDSS DR7 de cuásares, encontramos que el único parámetro que distingue a los radio cuásares BAL es el cociente de Eddington. Un 23% de los objetos emisores en radio son super-Eddington, mientras que sólo un 13% de los no emisores en radio lo son. Un diferencia aún mayor se encuentra entre cuásares BAL y no BAL (13% vs. 2%).

Chapter 1

AGN and Broad Absorption Line Quasars

1.1 Active Galactic Nuclei

Galaxies are conglomerates of stars, bound together by force of gravity. With a size comprised between a few kpc and tens of kpc, they can count from 10^7 to 10^{14} stars. The latter describe orbits around the central bulge (nucleus) of the galaxy, sometimes forming a disk-shaped structure (spiral galaxies), sometimes distributing in a spherical geometry (elliptical galaxies). Dust and interstellar medium are also present and spread in the entire volume. Recent studies introduce a further mass component, dark matter, necessary to explain the complex dynamic of the stars around the nucleus.

A small fraction of galaxies present an extreme bolometric luminosity ($L \sim 10^{11-14}$ $L_\odot$), not ascribable to the simple integration of the stellar emission, that would account only for a luminosity of $L \sim 10^{11}$ $L_\odot$: this impressive quantity of electromagnetic energy is produced in the central region of the galaxy, the nucleus, thus galaxies with this characteristic are said to harbour an Active Galactic Nucleus (AGN, see Fig 1.2 for an example spectrum). Their discovery dates back to 1908, when E.A. Fath observed the first optical spectrum of a Seyfert galaxy, presenting strong emission lines. After that, other similar galaxies were found, and classified by Seyfert as a distinct class (1943). In 1969 M. Smith defined the class of *Quasi-stellar Sources* (Quasars, QSOs hereafter) describing them as objects *'characterized by their star-like optical appearance and by emission-line spectra exhibiting large redshifts. They are not clearly associated with other objects on the sky, such as galaxies or clusters of galaxies'*. Some of them showed an associated radio-emission, and thus had already been detected in the first important radio surveys of the '60s (3C, PKS).

Seyfert and Quasar galaxies were the first classes of AGN to be discovered, but later other objects were found to share some of the observational characteristics of the formers, such as broad and narrow-line radio galaxies, ultraluminous infrared galaxies (ULIRGs) and low-ionization nuclear emission-line regions (LINERs).

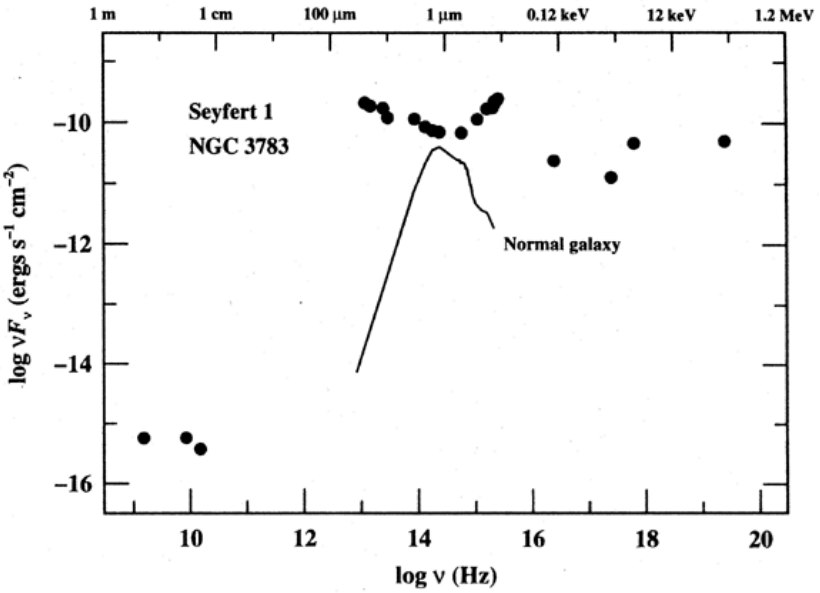

Figure 1.1: Spectral Energy Distribution (SED) from radio to γ-ray energy of the Seyfert galaxy NGC 3783 (Alloin et al. 2011), compared with a template spectrum of a normal galaxy (Elvis et al. 1994).

1.1.1 The Unification Scheme

After two decades of observational campaigns, in the '90s the scientific community achieved designing a model that allows the explanation of the variety of AGNs found with a single scheme, in which a few variables like the line of sight, the mass of the central object, the accretion rate, and the magnetic field strength can give origin to the observational characteristics of these objects: the Unification Scheme (Urry & Padovani 1995, see Fig. 1.2). Nowadays it is commonly accepted that the central engine of AGN is driven by accretion on a super-massive black hole (SMBH), that can reach a mass of 10^{10} $M_{\odot}$. The matter, falling into the potential well, displaces on a disk, conserving its angular momentum and reaching high temperatures. Friction between layers of material lying on different orbits causes transport of angular momentum towards the marginal part of the disk, allowing accretion on the SMBH. Typically a luminosity near to the Eddington Limit can be produced with this mechanism, justifying the great luminosity of AGNs. The relation between the accretion rate and the produced luminosity, following the virial theorem, is the following:

$$L = \frac{GM\dot{M}}{2r} \tag{1.1}$$

where $\dot{M}$ is the accretion rate and r is the radius of the disk. The continuum emission of the disk covers the optical-UV range.

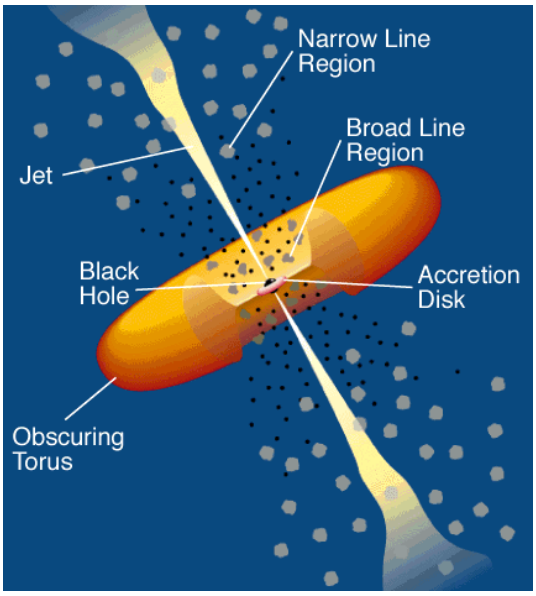

Figure 1.2: Sketch of the AGN unification scheme from Urry & Padovani (1995).

Superimposed to this emission, depending on the orientation of the AGN, broad emission lines can be found, emitted from the gas cloud system orbiting close to the central engine (the broad line region, BLR), thus with considerable orbital velocities. Typical dimensions for this region can be tens of light-days.

At the borders of the accretion disk and the BLR, an obscuring torus is supposed to be present, that when intercepted by the line of sight gives origin to the Seyfert II type of galaxies (lacking the broad emission line from the BLR). It is also supposed to attenuate the continuum emission from the accretion disk, like observed in Seyfert II. The geometry proposed for the torus foresees a maximum angle of $\sim 45°$ between the plane of the accretion disk and the external boundaries of the torus.

The Narrow Line Region (NLR) is responsible for the narrow emission lines found in the spectra of AGNs, and occupy a larger volume. This system of gas clouds can orbit as far as a fraction of kpc, thus with lower velocities than the BLR.

Finally a jet, responsable for the radio emission of the AGN, can be present in polar directions (see below for further details about radio-loud objects).

This combination of components, seen from different viewing angles, can produce the variety of the observed AGNs, for example: radio galaxies will be AGN seen from an equatorial point of view, while Blazars are seen from the pole, Seyfert II galaxies will be radio-quiet AGN seen through the torus, and Quasars will be radio-loud AGN seen with an angle comprised between $\sim 5° < \alpha <\sim 45°$ degrees from the pole, allowing to see the broad emission lines produced from the BLR.

The radio emission

Approximatively 10% of AGNs present non-thermal emission in the radio band, and thus are called *radio-loud*. This emission is due to a jet, starting from the inner region of the accretion disk, that is able to accelerate particles up to relativistic velocities. The jet is collimated by strong magnetic fields toward polar directions: charged particles moving along the field lines describe spiral trajectories (accelerated by the Lorentz force) and consequently emits radiation. This continuum emission is called synchrotron radiation and depends on the magnetic field strength, the density of charged particles (mainly electrons) and the energy distribution of these particles: assuming a power-law distribution $\propto E^p$ for the latter, the synchrotron emission spectrum will follow the law:

$$S(\nu) = \int_{E_1}^{E_2} S(E,\nu) \cdot n(E) dE \;\propto\; \nu^{\alpha} \tag{1.2}$$

where $n(E)$ is the energy distribution of the particles, integrated between the minimum (E_1) and the maximum (E_2) energy. The spectral index of the synchrotron emission (α) will be related to the same quantity relative to the particles through the relation:

$$\alpha = \frac{p-1}{2} \tag{1.3}$$

The jet-producing mechanism and dynamic are still under debate, but recent works (Mignone et al. 2010) achieved in simulating the AGN environment with numerical codes and can confirm that the magnetic field is essential for the production and the collimation processes.

The radio emission commonly observed in AGN can be much more complex than a simple power law: typically a turn-over frequency (ν_{peak}, see Fig. 1.3) between 0.5 and 10 GHz can be observed in radio sources with an age of a few thousands years, followed on the left-hand by a steepening of the spectrum. This particular shape is due to the Synchrotron Self Absorption process (SSA), consisting in the absorption of the radio photons by the same particle population responsable for the emission. Younger radio sources will have high turn-over frequencies, while in old radio sources a flattening can be visible in the MHz frequency range.

Also the break frequency (ν_{break} is related to the age of the sources: when the high energy particles fueling the emission have lost a significant fraction of their energy, the right-hand tail of the synchrotron emission become steeper, producing a 'knee' in the power law (Fig. 1.3).

Depending on the large structure of the magnetic field, a fraction of the total power can be polarized, generally linearly, perpendicularly to the direction of the field lines. The measured polarization can thus give a picture of the magnetic field in the jet.

As will be explained in chapter 2, radio emission from AGN can be a useful tool trying to understand the age and the orientation of the sources, and to probe the physical environment of these high-energy cosmic laboratories.

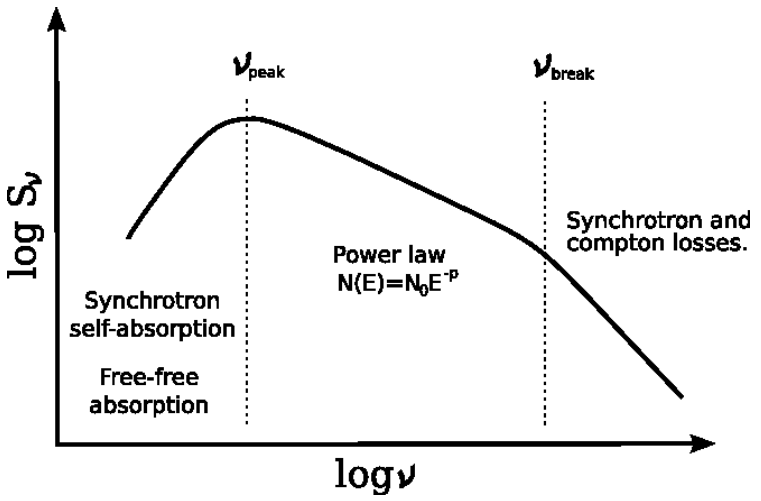

Figure 1.3: Example of synchrotron emission spectrum.

AGN outflows

Another type of ejection can be produced in AGN: outflows. They originate from the accretion disk and their production can be referable to three main processes: thermal pressure, radiation pressure or magnetic pressure. The first process can only account for the slowest outflows, produced in the external part of the disk, where the escape velocity from the central SMBH is lower. The high luminosity produced by the accretion can justify outflows in most of cases, through radiation pressure mechanism. In this way high velocity outflows can be sporadically produced when the luminosity exceeds the Eddington limit, but also at lower luminosities this can be an efficient launching mechanism thanks to the UV resonance spectral lines opacity (Line Driven winds, Castor et al. 1975). Finally, magnetic pressure is invoked when the previous mechanisms cannot be applied, since nowadays only qualitative predictions from magneto-hydrodynamic simulations are present in literature.

Outflows can be detected in the optical-UV or even X-ray spectrum as absorption lines, with a broadening related with the maximum velocity of the absorbing material. Many quasars show the presence of outflows in their spectra, but only in Broad Absorption Line (BAL) Quasars they can reach velocities up to 0.2 c (see Sec. 1.3).

1.2 Quasars

Quasars are AGN that present strong, broad emission lines in their spectrum, a large UV flux, and a radio emission in ∼10% of cases. Following the unification scheme, these objects are observed from a line of sight comprised between

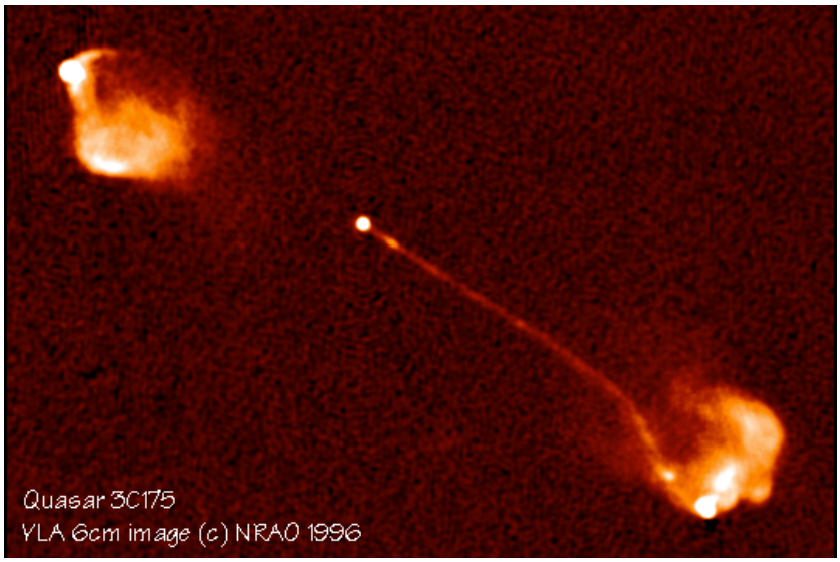

Figure 1.4: Radio image of the Quasar 3C173 obtained with the Very Large Array (VLA). The jet is visible as the collimated ejection of matter starting from the core. Two lobes are present, ending in hot-spots due to the interaction with the intergalactic medium. The overall linear size of the radio structure is 212 kpc, well above the typical size of galaxies of about tens of kpc. Image courtesy of NRAO/AUI.

$\sim 5°$ (otherwise they would be Blazars) and $\sim 45°$ (otherwise they would be torus-obscured) from the polar axis: in this range of angles it is possible to directly observe the central engine, thus the BLR and the optical-UV continuum emission from the accretion disk will dominate the spectrum. Since the first radio surveys, some of them were catalogued and became standard candles for radio astronomy, like 3C286 and 3C47, because of their stable and strong flux density. Morphologies in the radio band can vary from compact, young sources to extended ones, up to Mpc, presenting long jets and lobes terminating in hot-spots, due to the interaction with the intergalactic medium. Both Fanaroff-Riley I (FR I, core-dominated) and II (FR II, lobe-dominated) sources can be found (see Fig. 1.4 for an example of FR II quasar; the original radio-sources classification can be found in Fanaroff & Riley 1974).

Quasars are present in the local universe but also at cosmological distances, with redshifts up to ~ 6 (see Fig. 1.5). The number of known quasars, identified from their optical spectrum, has dramatically increased after the various releases of the Sloan Digital Sky Survey (SDSS), starting from year 2000. Nowadays $\sim$120,000 QSOs are known: given their powerful overall emission they can also be used as cosmological probes to study the high-redshift universe. For example, while in high-redshift QSOs only sharp absorption regions caused by neutral hydrogen are present, in local QSOs a Lyman α forest in the blue region of their optical spectrum can be detected, indicating the presence

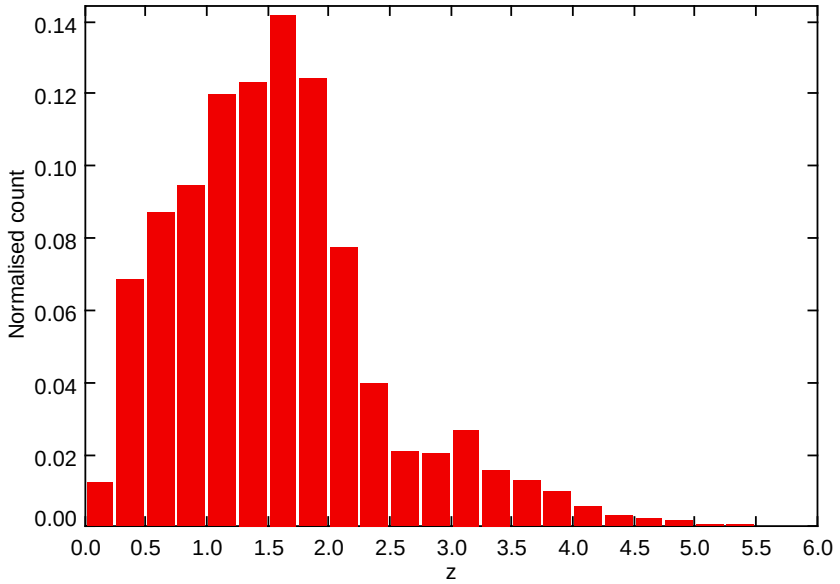

Figure 1.5: Redshift distribution for the QSOs from the SDSS DR7 Quasar Catalogue (Shen et al. 2011).

of ionized hydrogen clouds. This can be an indication of the re-ionization era supposed by cosmologists. Moreover, metal features in the spectra at cosmological distances suggest a population III class of stars to be present before the formation of the first galaxies.

In this work we will study 3 samples of intermediate-redshift QSOs, approximatively in the range 1.5-3. Thus we avoid any cosmological implication in the results.

1.3 BAL Quasars

Quasar outflows are manifested most spectacularly as broad absorption lines in the blue wings of prominent emission lines (e.g. CIV) in 10–20% of optically-selected quasars, tracing outflow velocities up to ∼0.2 c (Hewett & Foltz 2003). The absorption troughs can be highly structured, but are smooth compared with thermal line widths. About 20% of BALs are detached from the corresponding emission line by several thousand $km\ s^{-1}$ (Korista et al. 1993 for examples). The blue and red edges of the BAL absorption trough are often relatively abrupt, spanning ∼100s $km\ s^{-1}$.

These distinctive features would be hard to reconcile with absorption by individual clouds, but are consistent with the line of sight to a BAL quasar intersecting an outflow which is not entirely radial, e.g. an outflow which initially emerges perpendicularly to the accretion disk, and is then accelerated radially (Murray et al. 1995, Elvis 2000). NV 1240 Å BALs often absorb part of the Lyα emission line, so the BAL region must typically lie outside

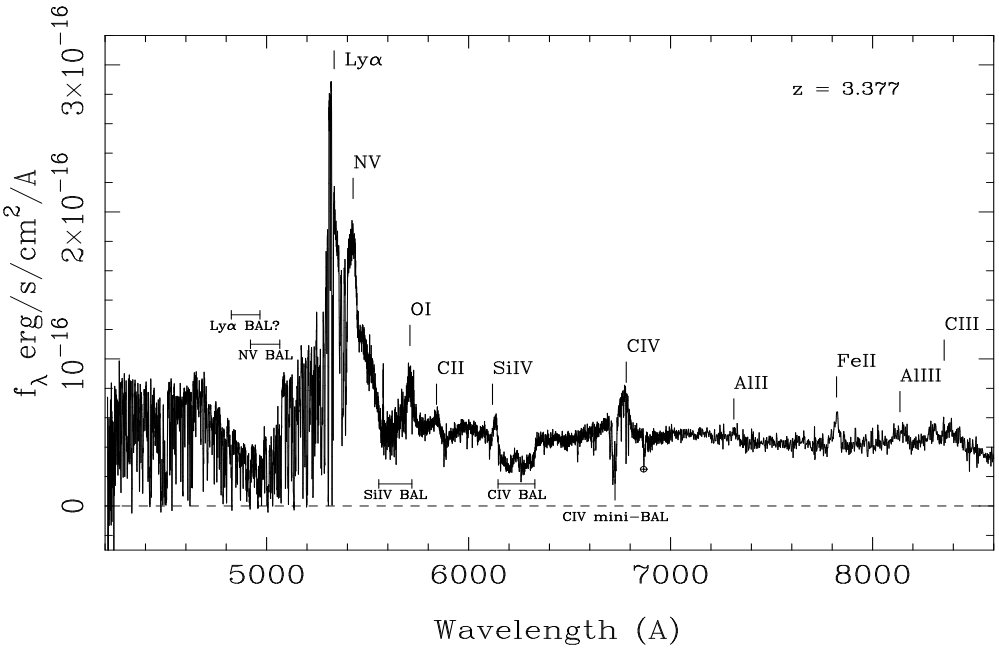

Figure 1.6: Medium-resolution spectrum of a BAL QSO from Benn et al. (2005). C IV and Si IV BALs are visible.

at least some of the broad emission-line region (BLR), i.e. > 0.1 pc from the quasar nucleus, but otherwise the distance is unknown within several orders of magnitude. BALs are generally saturated but non-black, implying partial covering of the nuclear regions (or infilling of the absorption troughs by scattered light). Saturation means that column densities cannot be measured directly from apparent absorption depths.

The most prominent BALs are due to high-ionisation species, particularly Li-like ions with one electron in the outer orbit: C IV, Si IV, N V. Quasars whose absorption is dominated by these are known as high-ionisation BALs (HiBALs). Some 15% of BAL quasars also show absorption by lower-ionisation species, such as Mg II and Al III, and are known as LoBALs. FeLoBALs are a small subset of the LoBALs showing absorption by Fe II and Fe III.

Absorbers similar to quasar BALs are seen in Seyfert 1 galaxies, albeit with lower outflow velocities, typically less than a few hundred $km\ s^{-1}$ (see contributions in Crenshaw, Kraemer & George 2002).

No self-consistent physical model yet exists for the acceleration of the outflowing gas in BAL quasars, or, if the filling factor is small (many small clouds), for its confinement. Possible mechanisms for the acceleration include radiation pressure, pressure from cosmic rays or centrifugally-driven magnetic disk winds (de Kool 1997). Radiation pressure is a popular candidate, but it is not clear how it can be sustained without over-ionising the gas.

BAL outflows are crucial for understanding the physics of AGN because:

- They probe the inner regions of the accretion disk, and probably play a role in the accretion process by helping to shed angular momentum;
- Many BAL quasars are super-Eddington accretors, offering a unique perspective on the changes in disk geometry (e.g. thickening) with accretion rate;
- The highly-energetic BAL outflows are probably related to other outflows seen in AGN (e.g. in radio galaxies).

Hypotheses about the nature of BAL quasars differ mainly in the emphasis placed on the role of orientation. On the one hand, BALs may be present in all quasars but are intercepted by only ∼10–20% of the lines of sight to the quasar (Weymann et al. 1991, Elvis 2000), e.g. within the walls of a bi-funnel centred on the nucleus. Alternatively, BALs may arise in a physically distinct population of quasars, e.g. newborn quasars shedding their cocoons of gas and dust, or quasars with unusually massive black holes, or with unusually high accretion rates (Briggs et al. 1984, Boroson & Meyers 1992).

Until recently, very few radio-loud BAL quasars were known. This changed with the advent of the FIRST Bright Quasar Survey (FBQS, Becker et al. 2001). Becker et al. (2001) estimated that BALs are four times less common amongst quasars with $\log R^* > 2$ (radio-loudness $R^* = S_{5\mathrm{GHz}}/S_{2500\ \mathring{A}}$, Stocke et al. 1992) than amongst quasars with $\log R^* < 1$. Hewett & Foltz (2003) note that optically-bright BAL quasars are half as likely as non-BALs to have $S_{1.4}$ GHz >1 mJy.

The reason for the dependence of the BAL fraction on R^* is unknown, but it may reflect the higher ratio of X-ray to UV luminosity in radio-louder objects, which could over-ionise the gas, reducing the velocity to which line-driven winds can be accelerated (Murray et al. 1995). Becker et al. (2000) found that radio-selected BAL quasars have a range of spectral indices, which suggests a wide range of orientations, contrary to the favoured interpretation for optically- selected quasars. Radio-Loud BALs tend to be compact in the radio, similar to GPS or CSS sources, and GPS/CSS sources are thought to be the young counterparts of powerful large-scale radio sources (O'Dea 1998, Montenegro-Montes et al. 2008a). This supports the alternative hypothesis that BALs represent an early phase in the life of quasars (Gregg at al. 2000).

In Boroson et al. (2002) scheme for the classification of AGN, based on a principal-component analysis of AGN properties, the different observed types correspond to different combinations of $L/L_{Eddington}$ (luminosity as a fraction of Eddington luminosity) and dM/dt (the accretion rate). BAL quasars occupy one corner of this space, with $L/L_{Eddington} \sim 1$, similar to narrow-line Sy1 galaxies, but with a much higher accretion rate. The BAL quasar accretion rates are similar to those of radio-loud quasars, but with larger $L/L_{Eddington}$ (and lower-mass black holes). In Boroson's scheme, the rare radio-loud BAL quasars may be objects with extremely high accretion rates.

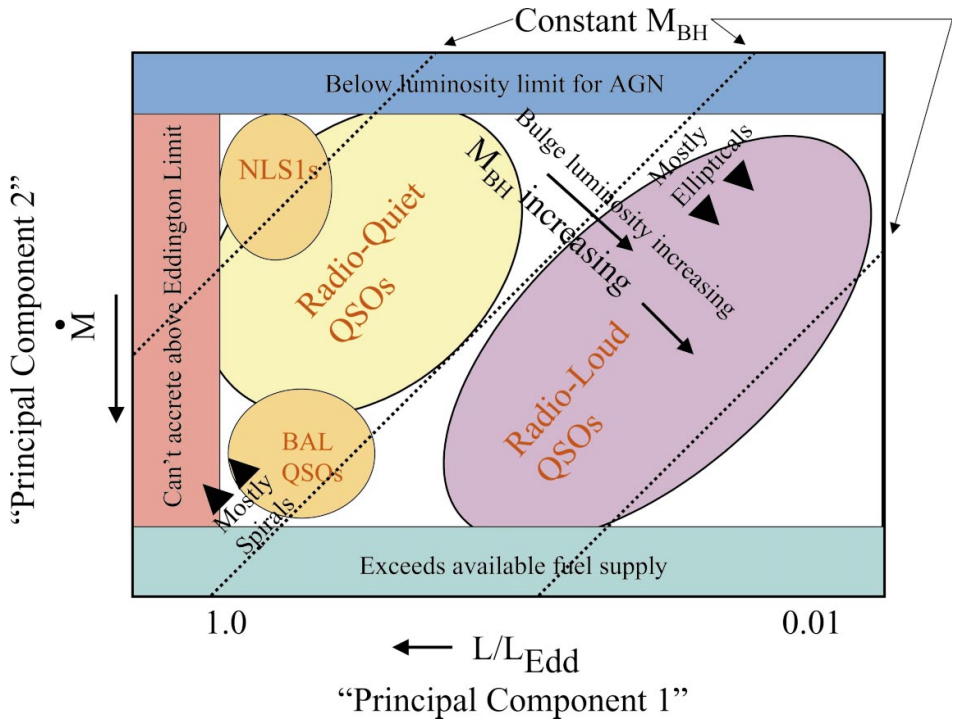

Figure 1.7: Boroson et al. (2002) scheme for the classification of AGN.

1.3.1 Proposed models

Three general scenarios have been put forward to explain the presence of BALs:

- in the *orientation model* proposed by Elvis (2000) BALs are produced by a funnel-shaped thin outflow, arising vertically from a narrow range of radii on the accretion disk and then bending outward to a cone angle of $\sim 60°$ by the effect of the radiation force. When viewed at certain angles this structure gives rise to the BALs. In this model, the covering factor of the outflow would be the same as the observed fraction of BAL QSOs, i.e. $\sim$20%. This model was proposed for radio-quiet QSOs, since at the time most of the BALs had been found in radio-quiet QSOs. Elvis (2000) suggests as a possible scenario for the radio loud BALs that the magnetic fields could recollimate the outflow near the point at which it would otherwise be accelerated radially to BAL velocities and instead accelerate the flow towards the poles.

- on the basis of radio variability arguments and on the groundwork by Punsly (1999a, 1999b), Zhou et al. (2006) and Ghosh & Punsly (2007) propose that some BAL QSOs, including both radio-loud and radio-quiet, are viewed nearly face-on, with the BAL outflows aligned within 15° of the polar direction. Punsly (1999b) remarks that the *bipolar wind model* does not preclude the coexistence of equatorial BAL winds.

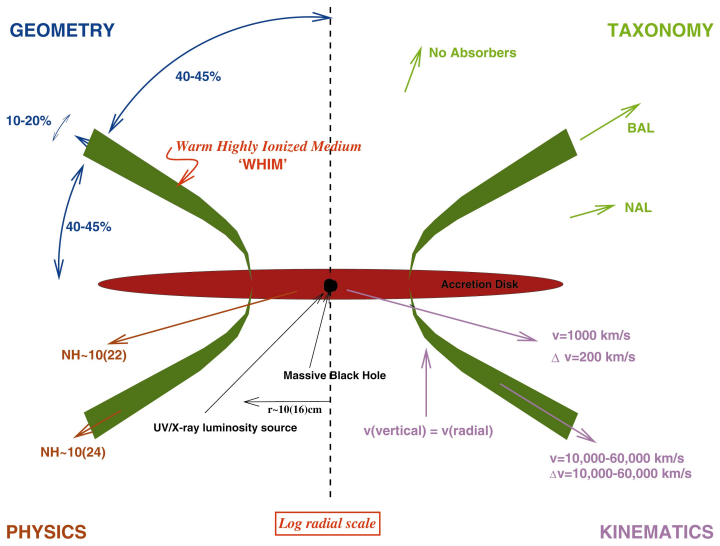

Figure 1.8: Sketch of the Elvis (2000) model. BALs are seen in the spectrum when the funnel-shaped outflow intercept the line of sight.

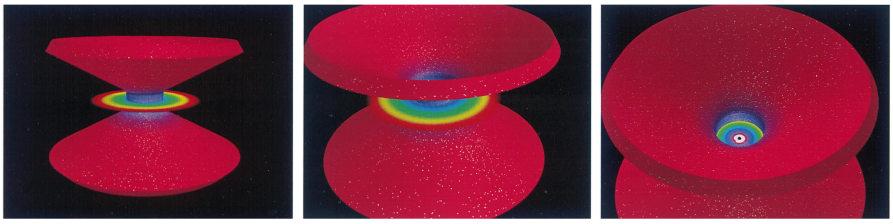

Figure 1.9: 3D rendering of the funnel-shaped outflows proposed by Elvis (2000).

- in the *evolutionary scheme*, the broad absorption troughs are produced during some specific period in the evolution of the quasar, perhaps as it transforms itself from a fully enshrouded object with a large infrared luminosity, through a BAL phase, into a normal quasar (e.g., Briggs et al. 1984; Lípari & Terlevich 2006). BAL QSOs could be newborn quasars in which strong nuclear starburst activity could be expelling their dusty cocoons. This hypothesis finds support in the radio, with a large fraction of radio-loud BAL QSOs, 2/3 showing spectral shapes and morphologies similar to Giga-Hertz-Peaked (GPS) or Compact Steep Spectrum (CSS) sources (Montenegro-Montes et al. 2008a), a class of radio sources interpreted as either young radio sources (Fanti et al. 1990) or radio sources frustrated by interaction with a dense environment (van Breugel et al. 1984).

1.3.2 Previous works from our group

Montenegro-Montes et al. (2008b) studied a sample composed of the 15 radio brightest BAL QSOs known until 2005, with flux densities $S_{1.4\ \mathrm{GHz}} > 15$ mJy. They measured radio flux densities in full polarization using both the 100-m Effelsberg telescope and the VLA, covering a wide spectral range, from 1.4 up to 43 GHz. Many of the radio characteristics of these sources were found to be prototypical of CSS or GPS sources, and a variety of spectral indices were present, allowing different orientations for the BAL producing outflow.

The low flux-density limit of this sample did not allow them to obtain significant polarization measurements, and only for a few sources VLBI follow up observations were possible with reasonable rms values (Montenegro-Montes et al. 2008b). A variety of morphologies, and hence orientations, were found, difficult to reconcile with a simple orientation scenario.

By the end of 2008 a new edition of the SDSS QSO catalogue was released, allowing to expand the original sample and to choose brighter objects, useful to plan a new observing campaign whose results are described in this thesis.

1.3.3 This thesis

To overcome the difficulties due to the low flux density of the previous sample, we defined a new sample with a brighter flux density limit, $S_{1.4\ \mathrm{GHz}} > 30$ mJy (see chapter 2). The sample is based on the correlation of the FIRST Catalogue (Faint Images of the Radio Sky at Twenty-cm; Becker et al. 1995; White et al. 1997) with the 4th SDSS Quasar Catalogue (Schneider et al. 2007) drawn from the 5th data release of the Sloan Digital Sky Survey (SDSS-DR5;Adelman-McCarthy et al. 2007). This sample is therefore more homogeneous than the one studied in Montenegro-Montes et al. (2008a).

We planned an observational campaign from cm up to mm-wavelengths, using single dishes and interferometers, both on local and global scale. Our target was the full sampling of the SED in the radio domain, to detect and

study the synchrotron emission (kpc-scale) and the morphology of BAL QSOs (pc-scale). In the mm-domain we tried to detect the grey-body dust emission, to infer dust abundancy with respect to non-BAL QSOs. Moreover, we obtained observing time at the TNG in 2008, to study RL vs RQ BAL QSOs through infrared spectroscopy.

The thesis outline is the following:

- In chapter two we present the RL BAL QSO sample, and the selection procedure adopted to discriminate BAL form non-BAL QSOs.
- In chapter three we show the radio spectra and polarization properties of the BAL and non-BAL sample, underlining all the possible differences related with orientation, age and dimensions.
- In chapter four a variability study is presented, realized using the Montenegro-Montes et al. (2008a) sample, implementing new data taken in 2009.
- In chapter five we present the results of the global VLBI campaign, that allowed us to resolve the brightest sources of the BAL QSO sample, and to study their morphology
- In chapter six the dust-detection experiment is reported, possible indicator of the age and of the physical conditions around the central AGN.
- In chapter seven we infer some properties of the central kpc through infrared spectroscopy, using a sample of optically bright RL and RQ BAL QSOs.

A brief summary of the conclusions from the different chapters is given in chapter eight, in order to insert in the AGN context the multi-wavelength observational properties of BAL QSOs found during this work.

Chapter 2

The BAL QSO sample and comparison sample

The BAL QSO sample comprises 25 QSOs from the fourth edition of the SDSS Quasar Catalogue (Schneider et al. 2007) with a FIRST radio counterpart having $S_{1.4} > 30$ mJy. This limit is twice as bright as the one used by Montenegro-Montes et al. (2008a) in their pilot sample. We made a two-step selection of BAL QSOs: (1) We applied an automatic algorithm using a constant continuum to select the QSOs with possible C IV absorption in their SDSS spectra. (2) We refined the identification of the BAL QSOs by interactively fitting the continuum and measuring the absorption index (AI), as defined by Trump et al. (2006), for all the candidate BAL QSOs from the previous step. We included in our BAL sample 2.1 any QSOs with AI>100 km s^{-1}. A comparison sample of non-BAL QSOs is listed in Table 2.2. The selection of the samples is described in more detail below.

The fourth edition of the SDSS Quasar Catalogue contains 77429 QSOs, of which 6226 have a FIRST radio source lying < 2 arcsec away, assumed to be the radio counterpart. 2158 of these lie in the redshift range $1.7<z<4.7$, allowing identification of C IV features on SDSS spectra. We made a two-step search for BALs in the spectra of the 536 of these with flux density limit $S_{1.4} >$ 30 mJy.

The first step in selection of the BAL QSOs was measurement of the intrinsic AI as defined by Hall et al. (2002):

$$\mathrm{AI} = \int_{0}^{25000} (1 - \frac{f(v)}{0.9}) \cdot C dv \tag{2.1}$$

where *f(v)* is the normalized flux density. The value of C is unity in contiguous intervals of width 450 km s^{-1} or greater, over which the quantity in parentheses is everywhere positive; otherwise $C = 0$. AI was computed in C IV using an automatic procedure in which equation 1 was applied using as continuum for the normalization the median value of the signal in the rest-frame spectral window 1440-1470 Å. Objects with AI > 0 were selected as possible BAL QSO candidates.

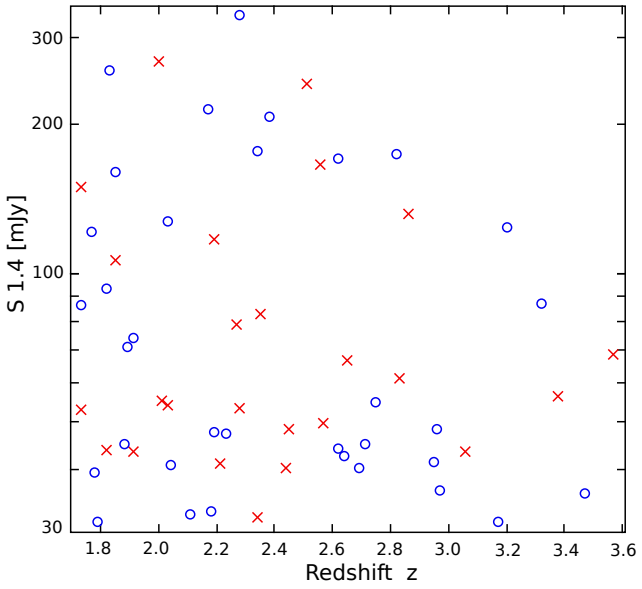

Figure 2.1: Distribution in flux density and redshift, of the QSOs in the BAL (crosses) and non-BAL (circles) samples.

Each of the 536 spectra were examined by eye to identify any obvious wrong classifications due to, e.g., a poor estimate of the continuum derived from noise peaks or other features within the used spectral window. As a result of this combined automated and visual selection we found 29 initial BAL QSO candidates.

Thirty of the QSOs with AI=0 were randomly selected to build the control sample, with the requirement that their position in the sky was convenient for scheduling purposes in the various observing runs, and the distribution in redshift matched as possible the BAL QSO sample.

These 59 QSOs form the sample of sources for which we obtained the multifrequency radio observations for this work.

The above selection procedure, using a constant continuum at a fixed wavelength, is appropriate to deal with large initial samples, but has two important caveats: (1) AI can be understimated if low-velocity absorption troughs are superimposed on the emission line, and (2) the assumption of a constant continuum on the region of interest may be inadequate for some sources. As a result, the control sample may include some QSOs which are more appropriately classified as BALs, and vice versa. We measured the AI of the 59 QSOs more accurately usning the following procedure. The continuum was obtained by interactively fitting the spectral region between the Si IV to the C IV emission lines (both included) with splines. After normalization with the fitted continuum, the Si IV AI was measured using Eq. 1 but with the more strict definition from Trump et al. (2006), in which parameter C is unity over a contiguous interval of 1000 km s^{-1} rather than the 450 km s^{-1} used by Hall et al. (2002).

Table 2.1: The sample of 25 radio-loud BAL QSOs studied in this paper. Columns 2-6 give the optical coordinates and redshifts from SDSS, the absorption index for the C IV line (width of at least 1000 km s^{-1}), the FIRST peak flux densities and the type.

Name	RA (J2000)	DEC (J2000)	z	AI (km s^{-1})	$S_{1.4}$ (mJy)	Type
0044+00	00 44 44.06	+00 13 03.5	2.28	1170[1]	53.1	Hi
0756+37	07 56 28.24	+37 14 55.6	2.51	330	239.4	Hi
0816+48	08 16 18.99	+48 23 28.4	3.57	260	68.3	H
0842+06	08 42 24.38	+06 31 16.8	2.45	2690[1]	48.1	H
0849+27	08 49 14.27	+27 57 29.7	1.73	540	52.8	Hi
0905+02	09 05 52.41	+02 59 31.5	1.82	130	43.5	Hi
0929+37	09 29 13.97	+37 57 43.0	1.91	2170	43.2	Hi
1014+05	10 14 40.35	+05 37 12.6	2.01	250	55.0	Hi
1040+05	10 40 59.80	+05 55 24.4	2.44	4920[1]	40.2	H
1054+51	10 54 16.51	+51 23 26.1	2.34	2220[1]	32.0	H
1102+11	11 02 06.66	+11 21 04.9	2.35	506	82.3	H
1103+11	11 03 34.79	+11 14 42.4	1.73	380	148.0	FeLo
1129+44	11 29 38.47	+44 03 25.1	2.21	1430	41.1	Hi
1159+01	11 59 44.82	+01 12 06.9	2.00	2260[1]	266.5	Hi
1159+06	11 59 01.75	+06 56 19.1	2.19	3645	116.6	FeLo
1229+09	12 29 09.64	+09 38 10.1	2.65	230	66.2	H
1237+47	12 37 17.44	+47 08 07.0	2.27	1300[1]	78.5	FeLo?
1304+13	13 04 48.06	+13 04 16.6	2.57	640	49.6	H
1327+03	13 27 03.21	+03 13 11.2	2.83	190	60.7	H
1335+02	13 35 11.90	+02 53 09.5	1.85	210	105.3	Hi
1337−02	13 37 01.40	−02 46 30.3	3.06	590	43.3	H
1404+07	14 04 33.01	+07 28 47.2	2.86	120	131.1	H
1406+34	14 06 53.84	+34 33 37.3	2.56	350	164.4	H
1603+30	16 03 54.15	+30 02 08.7	2.03	1355	53.7	H
1624+37	16 24 53.47	+37 58 06.6	3.38	1020[1]	56.1	H

Notes: [1] Balnicity index BI > 0 following Weymann et al. (1991).

Table 2.2: The sample of 34 comparison (non-BAL) QSOs studied in this paper. See caption of Tab. 2.1 for details.

Name	RA (J2000)	DEC (J2000)	z	AI (km s^{-1})	$S_{1.4}$ (mJy)
0014+01	00 14 27.93	+01 13 34.0	2.18	0	32.7
0029−09	00 29 49.46	−09 51 44.8	2.71	0	44.7
0033−00	00 33 04.32	−00 48 14.5	1.79	56	31.3
0103−11	01 03 28.72	−11 04 14.6	2.19	0	47.5
0124+00	01 24 01.75	+00 35 00.1	1.85	0	159.3
0125−00	01 25 17.19	−00 18 29.7	2.28	0	329.1
0152+01	01 52 10.35	+01 12 28.9	3.17	0	31.3
0154−00	01 54 54.37	−00 07 23.1	1.83	0	255.4
0158−00	01 58 32.52	−00 42 38.5	2.62	0	169.4
0750+36	07 50 19.55	+36 30 02.8	2.03	0	126.7
1005+48	10 05 15.98	+48 05 33.2	2.38	1	206.1
1322+50	13 22 50.55	+50 03 35.4	1.73	33	85.7
1333+47	13 33 25.06	+47 29 35.4	2.62	22	44.0
1401+52	14 01 26.15	+52 08 34.6	2.97	1	36.2
1411+34	14 11 55.24	+34 15 10.4	1.82	0	92.5
1411+43	14 11 52.77	+43 00 23.9	3.20	0	122.9
1502+55	15 02 06.53	+55 21 46.1	3.32	0	86.5
1512+35	15 12 58.36	+35 25 33.3	2.23	0	47.1
1521+43	15 21 49.61	+43 36 39.4	2.17	0	213.5
1528+53	15 28 21.68	+53 10 30.7	2.82	0	172.4
1554+30	15 54 29.40	+30 01 19.0	2.69	35	40.0
1634+32	16 34 12.77	+32 03 35.4	2.34	0	175.2
1636+35	16 36 46.41	+35 57 43.7	1.91	0	73.4
1641+33	16 41 48.07	+33 45 12.5	2.75	0	54.5
1728+56	17 28 52.61	+56 41 43.9	1.77	0	120.3
2109−07	21 09 26.41	−07 39 25.9	1.88	0	44.8
2129+00	21 29 16.61	+00 37 56.7	2.96	0	48.0
2143+00	21 43 24.37	+00 35 02.8	2.04	0	40.6
2238+00	22 38 43.57	+00 16 48.0	3.47	0	35.6
2244+00	22 44 59.44	+00 00 33.4	2.95	0	41.4
2248−09	22 48 00.70	−09 07 44.9	2.11	40	32.4
2331+01	23 31 32.84	+01 06 21.0	2.64	0	42.4
2346+00	23 46 24.56	+00 19 14.2	1.78	0	39.4
2353−00	23 53 30.21	−00 04 13.4	1.89	0	70.5

Of the total 59 QSOs, 25 have AI $>$ 100 km s^{-1} according to this definition, and these form the final BAL QSO sample. This sample is shown in Table 1, where optical coordinates, redshifts (both from SDSS), AI, and peak flux densities at 1.4 GHz from FIRST are given. In the last column we also provide the BAL type, determined by the ionized species producing the absorption features: high-ionization BAL QSOs, in which only an absorption trough blueward of the C IV emission line is detected, are indicated as 'Hi', objects with too high redshift to allow the inspection of the Mg II emission region are indicated as 'H', while objects showing both C IV and Mg II absorption trough, plus additional Fe II absorption features, are indicated as 'FeLo'. For one object (1237+47, indicated as 'FeLo?') Fe II absorption is visible, but the Mg II emission line falls at the edge of the spectrum, thus not allowing a clear absorption measurement.

Of the 29 QSOs initially selected as BAL QSOs, 1005+48, 1333+47, 1401+52, 1554+30, 2129+00, 2248−09, and 2331+01 have AI$<$100 km s^{-1}, and were therefore included in the comparison sample of non-BAL QSOs. In the opposite sense, three QSOs initially in the control sample have AI$>$100 km s^{-1} and were re-classified as BAL QSOs: 1103+11, 1335+02, and 1404+07. The comparison sample is listed in Table 2. Figure 1 shows the distribution of the 59 QSOs in redshift and $S_{1.4}$ flux density.

We note that the minimum velocity width we used for the selection of BAL QSOs, of 1000 km s^{-1}, although well above the maximum expected values for galactic halos, of $\sim$ 600 km s^{-1}, is half the value used in the classical definition of BAL QSOs by Weymann et al. (1991), which picks up the most extreme cases, and was based on radio-quiet QSOs. Although a sample of extreme BAL QSOs might better reveal the differences between the radio properties of BAL QSOs and a control sample of non-BAL QSOs, the fraction of BAL QSOs is lower among radio-selected samples than among optically selected ones, and moderate BALs should be included for several reasons. Firstly, in order to have a number of sources large enough for statistical studies. In addition, a more relaxed definition of broad absorption allows us to cover a wider range of outflow phenomena, including BALs with lower outflow velocities. These lower-velocity flows could be driven by different acceleration mechanisms, depending on the QSO radio luminosity (see Punsly 1999a and references therein, and Ghosh & Punsly 2007 for BAL QSO models and its relation to radio emission).

Using Weymann's Balnicity index (BI), defined as:

$$BI = -\int_{3000}^{25000} (1 - \frac{f(v)}{0.9}) \cdot C dv \tag{2.2}$$

that is the same as Eq. 1, except for the lower velocity limit, which should be of 3000 km s^{-1}, and the above mentioned wider absorption, $>$ 2000 km s^{-1}, we obtained BI $>$ 0 for 7 of the 25 BAL QSOs in this work, namely 0044+00, 0842+06, 1040+05, 1054+51, 1159+01, 1237+47 and 1624+37.

In Fig. 2.2 two spectra from the BAL QSO sample, fitted with a spline as

explained before, are shown. In the left hand spectrum two absorbing systems are present: the first is in the blue wing of the C IV emission line, while the second is detached and blueward. In the right hand spectrum the BAL is superimposed to the C IV emission line.

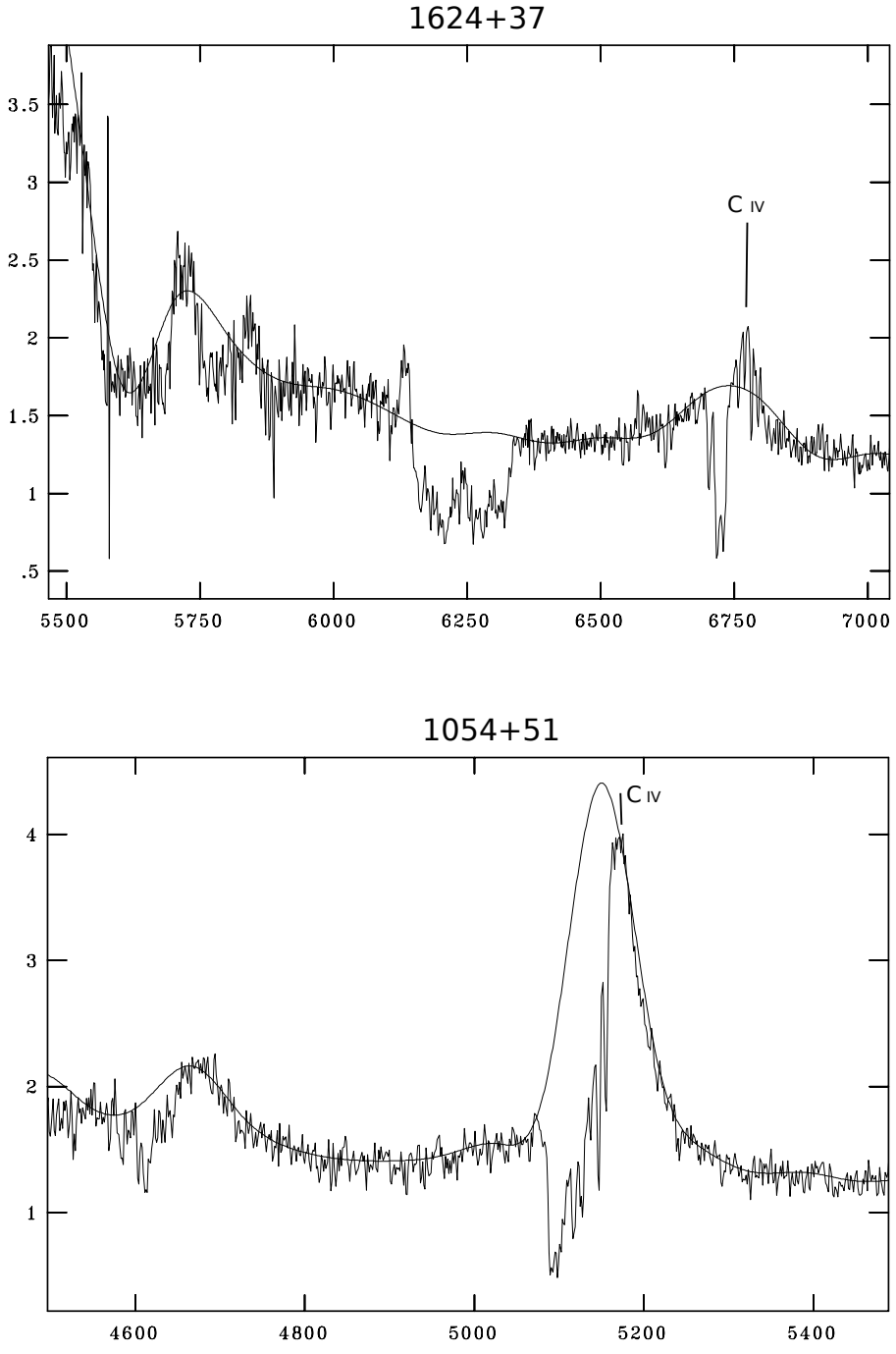

Figure 2.2: Two spectra from the BAL QSO sample (x-axis:Å; y-axis: $10^{-16} erg/cm^2/s/\mathring{A}$).

Chapter 3

Radio spectra and polarization properties

In this chapter we report the results of a statistical comparison between the radio properties of a subsample of radio-loud QSOs showing BAL-like features and a matched sample of radio-loud non-BAL QSOs, in order to test for consistency with the models discussed above. In particular, we measure the shape of the synchrotron spectra, the turn-over frequency and the polarisation properties, for the following reasons:

- The distribution of radio spectral indices constrains the distribution of orientations for a given population of radio sources (Orr & Browne 1982), since flatter spectral indices imply lines of sight closer to the radio axis. If the distribution of radio spectral indices of BAL QSOs were different from that of non-BAL QSOs, this would support the orientation hypothesis for the origin of BALs.

- The synchrotron turn-over frequency can be used to estimate the age of a source, assuming the source is not frustrated (recent studies of GPS and CSS sources tend to exclude the frustration scenario: Gupta et al. 2006, Morganti 2008). The age estimate is based on the observed correlation between linear size and turnover frequency of CSS and GPS radio sources (O'Dea & Baum 1997; Dallacasa et al. 2000). If BAL QSOs are found to be younger than the non-BAL QSOs in the comparison sample, the evolutionary hypothesis would be favoured.

- Polarisation properties provide clues about magnetic fields and particle densities in the environment of the active galactic nucleus. In particular, if a higher Rotation Measure is found for BAL QSOs, this may imply a denser environment.

Table 3.1: Summary of the observations.

Run	Date	Telescope	Frequencies (GHz)
1	14−23 Dec 07	Effelsberg	2.65, 4.85, 8.35, 10.5
2	10−15 Sep 08	Effelsberg	2.65, 4.85, 8.35, 10.5
3	1−5 Jul 09	Effelsberg	2.65, 4.85, 8.35, 10.5
4	21−27 Jul 09	VLA(C)	1.4, 4.86, 8.46, 22.5, 43.3

Table 3.2: Observing frequencies and beam sizes (half-power beam-width).

Telescope	Frequency (GHz)	Bandwidth (MHz)	$\theta_{\rm HPBW}$ (arcsec)
Effelsberg	2.65	80	265
Effelsberg	4.85	500	145
Effelsberg	8.35	1100	80
Effelsberg	10.5	300	65
VLA(C)	1.4	50	12.5
VLA(C)	4.86	50	3.9
VLA(C)	8.46	50	2.3
VLA(C)	22.5	50	0.9
VLA(C)	43.3	50	0.47

The cosmology adopted in this thesis assumes a flat universe and the following parameters: H_0=70 km s^{-1} Mpc^{-1}, Ω_Λ=0.7, Ω_M=0.3. The sign of the quoted spectral indices α is defined by $S_\nu \propto \nu^\alpha$.

3.1 Radio observations and data reduction

We observed the QSOs at frequencies ranging from 1.4 to 43 GHz, using the 100-m Effelsberg single dish and the VLA in full polarisation mode (Stokes I, Q and U images). Tables 3.1 and 3.2 summarise the different runs and observing setups.

3.1.1 Effelsberg 100-m telescope

Observations with the Effelsberg 100-m dish were carried out during 3 separate runs (see Table 3.1). All observations (for BAL QSOs and comparison QSOs) were carried out using cross-scans in azimuth and elevation at 2.65, 4.85, 8.35 and 10.5 GHz, with a cross-scan length of 4 times the beam size. On-source integration times were between 20 and 60 seconds per source and per frequency, depending on the expected source intensity.

During the data reduction, all scans were visually checked to remove radio-frequency interference, bad-weather effects (noisy scans due to heavy rain or clouds) or detector instabilities. The signals were fitted with a Gaussian to extract flux densities, following the standard reduction method for Effelsberg

data, using the CONT2 programme of the TOOLBOX[1] package. 3-σ upper limits were placed on the flux densities of undetected sources (Section 3.3).

The flux-densities were calibrated on the Baars et al. (1977) scale, via observations of 3C286. A calibration of the polarisation was carried out in the standard way, using observations of 3C286 to remove the effects of instrumental polarisation.

3.1.2 Very Large Array

In July 2009 we used the VLA to observe the BAL QSOs in the frequency range 1.4 to 43 GHz. We used five different receivers (L, C, X, K and Q band, corresponding to 1.4, 4.86, 8.46, 22.5 and 43.3 GHz) and imaged at all frequencies the QSOs in both the BAL QSO sample and the comparison sample. The integration times depended on band and source, and varied beween 4 and 15 minutes.

The highest angular resolutions reached in our work are lower than those reached by Montenegro-Montes et al. (2008a), since the latter used VLA in A configuration whereas that for this work we used configuration C at the VLA.

The flux-densities were calibrated on the Baars et al. (1977) scale, via observations of 3C286. 3C286 was also used as a phase calibrator. In addition, secondary phase calibrators were observed at regular time intervals (different for each band) and between 2 and 5 degrees from the target sources. At the highest frequencies (22 and 43 GHz) we switched between target and calibrator every 30 seconds ('fast-switching mode'), to improve the phase calibration.

The data were reduced with the 31DEC09 version of AIPS[2], and version 3.0 of CASA[3] was used to extract flux densities via an automated python script. We used the task IMSTAT to perform this calculation for the Stokes I, Q and U images. 3-σ upper limits were placed on the flux densities of undetected sources (Section 3.3).

The polarisations were calibrated using 3C286 as a strong unresolved source to determine the instrumental polarisation and the apparent polarisation angle.

3.1.3 Error determination

We followed the approach of Klein et al. (2003) for the determination of flux-density errors, considering three main contributions: (i) the fractional calibration error ΔS_{cal}, estimated from the dispersion of the observations of the flux density calibrators; (ii) the error introduced by noise, ΔS_n, which is estimated from the local noise around the source; and (iii) the confusion error ΔS_{conf} due to the possible presence of background sources within the beam area. When

[1] http://www.mpifr-bonn.mpg.de/english/radiotelescope/index.html

[2] http://www.aips.nrao.edu

[3] http://casa.nrao.edu

the beam has small dimensions, as in interferometric data, the last term can be neglected.

Thus the expressions for the total uncertainty of the Stokes parameters are given by equations 3.1 and 3.2 below for Effelsberg and the VLA, respectively:

$$\Delta S_i = \sqrt{(S_i \cdot \Delta S_{cal})^2 + \Delta S_{n,i}^2 + \Delta S_{conf,i}^2} \quad i = \mathrm{I, Q, U} \tag{3.1}$$

$$\Delta S_i = \sqrt{(S_i \cdot \Delta S_{cal})^2 + \Delta S_{n,i}^2 \cdot \frac{A_{src}}{A_{beam}}} \quad i = \mathrm{I, Q, U} \tag{3.2}$$

where A_{src} is the area of the aperture within which the source flux density is measured, and A_{beam} is the area of the synthesised beam. The expressions for the uncertainties of m (fractional polarisation) and χ (polarisation angle) can be found in Klein et al. (2003).

Typical values for the fractional calibration error are <10%, thus noise is often the dominant component of the total uncertainty.

3.2 Results and discussion

In Tables 3.3 and 3.4 we present our measurements of the flux-densities of the BAL QSOs and the comparison sample from 1.4 to 43 GHz. For sources which were resolved on the VLA images (see Section 4.1) we provide both the total flux densities and the flux densities of the individual components, where the components were well resolved and when reliable measurements were possible. At 1.4 GHz, if we made no measurements, we give in Tables 3.3 and 3.4 the FIRST integrated flux densities. In the last column of each table we give upper limits on the projected linear sizes of the unresolved sources, extracted from the highest-resolution VLA map with a significant detection. The sizes of resolved sources were obtained from whichever map presents the largest projected linear size.

We extended the SEDs to frequencies lower than 1.4 GHz using data from the literature (see Table 3.5). Flux densities and upper limits (when cut-out images were available) were collected from the following surveys: VLSS (74 MHz, Cohen et al. 2007), 6C (151 MHz, Hales et al. 1988), WENSS (325 MHz, de Bruyn et al. 2000), TEXAS (365 MHz, Douglas et al. 1996) and B3 (408 MHz, Ficarra et al. 1984).

3.2.1 Morphology

The radio morphologies of the QSOs in the two samples can be compared at the arcsec scale (a few-10 kpc at our median redshift) using the VLA maps, which have at all frequencies a higher resolution than the Effelsberg 100-m single-dish cross-scans. At 1.4 GHz, we complement our VLA data with those from FIRST data, obtained with a higher resolution. Maps of the resolved

Table 3.3: The measured flux densities (in mJy) for the sample of 25 radio-loud BAL QSOs. Flux densities at 1.4, 4.86, 8.46, 22 and 43 GHz are from the VLA; those at 2.6, 4.85, 8.35 and 10.5 GHz are from the Effelsberg telescope. Asterisked values are taken from the FIRST survey. Superscripts on the errors indicate the run number of the Effelsberg observations, according to the key in Table 3.1. Column 2 the specifies the component of the source being referred to (see Section 4.1): if no letter is present the total flux density is given. The last column gives the projected linear size (in kpc) of the resolved sources (in boldface) and the upper limits for unresolved sources (the latter taken from the highest-resolution map with at least a 3-σ detection).

Name	comp.	$S_{1.4}$	$S_{2.6}$	$S_{4.85}$	$S_{4.86}$	$S_{8.35}$	$S_{8.46}$	$S_{10.5}$	S_{22}	S_{43}	LS
0044+00		54.76±0.11*	54.8±2.9 [1]	30.9±1.0 [1]	34.2±1.8	24.0±1.0 [1]	25.5±0.6	26.9±3.9 [1]	9.5±2.7	4.9±1.8	<8
0756+37		213±14	266.0±3.1 [1]	209.6±2.6 [1]	226.2±2.0	131.5±3.0 [1]	142.1±1.8	113.6±5.2 [1]	56.2±2.4	<8.4	<8
0816+48		304±21	45.8±1.4 [1]	31.8±1.0 [1]	31.4±0.5	18.4±0.8 [1]	19.5±0.5	15.3±2.6 [1]	<5.7	-	**217**
0842+06		45.9±7.5	45.7±1.9 [1]	30.7±1.7 [1]	29.5±0.4	<54 [1]	20.9±0.5	15.4±4.6 [1]	6.9±1.4	-	<8
0849+27		67.08±0.30*	49.4±1.7 [1]	32.0±1.5 [1]	-	21.3±1.0 [1]	-	17.2±2.2 [1]	-	-	**173-382**
	A	7.84±0.15*	-	-	-	-	-	-	-	-	
	B	4.47±0.15*	-	-	-	-	-	-	-	-	
	C	53.95±0.15*	-	-	-	-	-	-	-	-	
	D	0.82±0.15*	-	-	-	-	-	-	-	-	
0905+02		32.8±8.5	87.0±3.5 [2]	47.8±2.7 [2]	-	27.9±1.1 [2]	28.5±1.4	<135 [2]	8.8±1.9	-	<8
0929+37		38.9±4.9	29.4±1.8 [2]	29.1±1.4 [2]	32.0±0.5	26.0±1.3 [2]	29.3±0.5	20.7±7.2 [2]	19.1±1.4	6.9±2.5	<8
1014+05		57.9±3.3	37.4±3.3 [3]	33.1±2.2 [3]	34.5±0.6	-	25.1±0.5	17.9±3.0 [3]	12.6±2.2	-	<8
1040+05		42.20±0.23*	-	-	37.2±1.4	-	5.2±0.4	-	-	-	<19
1054+51		38.8±3.4	32.1±1.9 [1]	16.7±1.1 [1]	15.9±0.5	8.6±0.7 [1]	9.5±0.6	7.9±3.2 [1]	<12.6	-	<19
1102+11		98.4±7.9	79.2±2.4 [3]	36.4±2.4 [3]	39.8±0.8	18.6±0.7 [2]	19.9±0.7	16.1±5.0 [2]	<4.2	-	<19
1103+11		250.43±0.21*	150.9±2.2 [1]	95.5±2.1 [1]	100.9±0.8	65.9±1.1 [1]	75.0±0.8	58.4±3.8 [1]	43.6±1.8	-	**69**
	A	76.14±0.15*	-	-	21.2±0.3	-	10.2±0.3	-	-	-	
	C	174.29±0.15*	-	-	79.7±0.7	-	64.8±0.7	-	-	-	
1129+44		42.1±7.4	72.1±1.6 [1]	41.3±1.5 [1]	38.5±2.5	23.9±6.6 [1]	26.6±1.7	19.5±3.9 [1]	3.1±1.2	-	<19
1159+01		264.4±9.8	-	-	146.1±1.3	-	176.6±2.2	-	169.2±2.8	-	<8
1159+06		159.5±3.1	109.5±5.3 [2]	60.2±2.5 [2]	58.5±1.1	35.8±1.6 [2]	37.6±0.7	26.2±3.3 [2]	4.6±2.3	-	<19
1229+09		81.3±6.6	35.8±1.5 [1]	15.4±2.3 [1]	17.3±0.5	15.7±6.3 [1]	-	7.5±2.4 [1]	<2.7	-	<32
1237+47		74.7±5.9	-	-	62.3±1.0	-	61.6±1.6	-	-	-	<19
1304+13		61.4±4.9	37.0±3.0 [3]	21.4±1.6 [3]	24.6±0.5	15±12 [2]	17.1±0.5	14.3±3.5 [2]	5.3±1.3	-	<8
1327+03		163±15	92.2±2.7 [1]	67.7±1.9 [1]	79.5±1.7	52.5±1.2 [1]	56.5±0.7	51.8±3.3 [1]	28.6±1.8	-	<8
1335+02		112.3±5.6	96.9±1.7 [1]	81.9±1.3 [1]	86.7±1.3	63.3±1.4 [1]	69.4±1.0	64.7±3.9 [1]	88.6±1.7	<10.5	<8
1337−02		47.2±5.3	67.3±3.2 [3]	42.3±2.7 [3]	42.9±0.8	-	16.4±0.5	-	-	-	<19
1404+07		187.8±3.6	225.9±2.6 [1]	209.4±2.8 [1]	206.4±2.3	173.6±2.4 [1]	189.6±2.2	160.9±7.5 [1]	146.9±2.3	-	<8
1406+34		165±24	246.6±2.9 [1]	301.5±3.1 [1]	312.8±3.1	263.1±3.4 [1]	276.3±3.0	237±10 [1]	180.1±2.9	90.2±3.4	<4
1603+30		54.17±0.14*	34.4±9.9 [3]	38.8±2.5 [3]	34.5±2.4	-	26.9±0.6	-	9.7±1.3	-	**17**
	A	-	-	-	-	-	-	-	2.4±0.8	-	
	C	-	-	-	-	-	-	-	7.3±1.0	-	
1624+37		56.44±0.14*	35.0±3.0 [1]	25.8±1.5 [1]	28.1±3.7	22.5±0.7 [1]	18.2±1.7	18.9±5.6 [1]	7.4±3.1	-	<19

Table 3.4: Flux densities for the sample of 34 non-BAL QSOs (see the caption of Table 3.3 for details). For source 2238+00 we give the upper limit of linear size from the FIRST, since the only significant detection from our observations was at 1.4 GHz, with a lower resolution.

Name	comp.	$S_{1.4}$	$S_{2.6}$	$S_{4.85}$	$S_{4.86}$	$S_{8.35}$	$S_{8.46}$	$S_{10.5}$	S_{22}	S_{43}	LS
0014+01		40.9±6.3	19.6±1.8 [3]	13.7±0.9 [3]	14.1±0.5	13.9±0.7 [3]	10.9±0.4	8.5±1.8 [3]	4.0±1.2	-	<8
0029−09		41.9±5.2	33.5±2.5 [3]	43.5±2.7 [3]	38.6±1.1	39.6±1.0 [3]	54.7±0.7	44.4±2.5 [3]	67.9±2.8	40.0±2.2	<4
0033−00		65.1±5.7	29.1±2.3 [3]	19.8±1.3 [3]	17.9±0.7	12.4±0.6 [3]	13.2±0.4	12.9±2.2 [3]	4.1±2.0	-	**51**
	A	-	-	-	-	-	2.5±0.2	-	-	-	
	C	-	-	-	-	-	10.7±0.3	-	-	-	
0103−11		50.17±0.15*	48.1±2.5 [3]	41.4±2.5 [3]	40.4±0.5	28.6±0.9 [3]	32.2±0.5	26.8±2.2 [3]	24.2±2.1	10.4±1.8	<4
0124+00		178.4±6.9	83.9±3.8 [2]	59.2±2.4 [2]	62.8±1.9	41.4±1.5 [2]	40.2±0.8	36.7±4.9 [2]	11.6±1.6	-	<8
0125−00		536.97±0.42*	365.7±3.4 [1]	248.4±2.8 [1]	240.3±4.5	158.6±3.7 [1]	173.7±1.9	151.9±7.7 [1]	81.2±2.6	46.0±2.9	**42**
	A	-	-	-	-	-	27.2±0.8	-	-	-	
	C	-	-	-	-	-	146.5±1.7	-	-	-	
0152+01		33.30±0.15*	-	-	9.2±1.2	-	10.7±0.9	-	3.3±1.3	<1.2	<19
0154−00		273.8±8.2	234.6±2.8 [2]	163.5±5.9 [2]	162.3±1.5	94.6±3.1 [2]	-	68.1±4.3 [2]	27.0±1.7	7.3±2.0	<4
0158−00		190.9±4.4	106.4±3.2 [2]	75.1±2.8 [2]	75.0±0.7	51±19 [2]	52.6±0.7	45.6±3.6 [2]	-	12.4±1.9	<4
0750+36		109.9±5.1	-	66.1±2.6 [2]	65.4±0.8	45.2±1.2 [2]	46.9±0.7	37.5±3.6 [2]	20.5±2.1	<5.1	<8
1005+48		161±22	162.2±2.5 [1]	111.5±4.4 [1]	121.3±1.0	69.9±3.2 [1]	83.6±1.1	68.7±4.0 [1]	45.7±1.6	10.9±2.4	<4
1322+50		116±10	78.9±2.4 [1]	54.3±1.5 [1]	55.6±0.9	42.7±1.1 [1]	40.2±0.7	35.6±3.2 [1]	14.3±2.6	-	<8
1333+47		176.4±6.9	-	26.6±1.7 [3]	25.9±0.5	-	17.8±0.5	-	13.9±3.5	-	<8
1401+52		100±13	47.8±3.3 [3]	36.7±2.4 [3]	33.2±0.6	-	24.9±1.2	-	8.3±1.6	-	<8
1411+34		189.14±0.24*	145.0±2.4 [1]	120.2±1.9 [1]	85.1±5.2	105.1±1.9 [1]	86.3±2.9	102.6±5.3 [1]	120.2±1.7	83.3±2.7	**199**
	A	28.32±0.14*	-	-	5.4±0.7	-	2.6±0.7	-	-	-	
	B	58.17±0.14*	-	-	16.4±0.7	-	5.3±0.7	-	-	-	
	C	102.65±0.14*	-	-	80.4±1.0	-	85.5±1.3	-	-	-	
1411+43		135.4±8.9	112.1±2.0 [1]	98.6±1.4 [1]	99.9±0.9	79.3±1.2 [1]	82.3±1.1	73.5±4.1 [1]	63.7±2.0	29.6±3.0	<4
1502+55		91.94±0.15*	58.9±1.6 [1]	35.2±1.1 [1]	35.6±0.7	34±16 [1]	24.9±0.5	19.7±2.7 [1]	7.2±1.7	-	<8
1512+35		47.48±0.13*	40.8±2.2 [2]	36.0±1.9 [2]	40.9±0.5	34.7±4.7 [2]	48.4±0.8	32.8±3.4 [2]	60.4±2.5	16.8±2.9	<4
1521+43		268.0±4.5	276.0±2.7 [1]	256.8±2.8 [1]	387.3±3.0	346.9±4.4 [1]	523.1±5.7	396±16 [1]	583.7±6.2	-	<8
1528+53		207±12	131.7±8.4 [1]	68.0±1.4 [1]	70.6±3.7	45.0±1.5 [1]	43.0±0.8	36.3±3.5 [1]	15.1±1.5	-	<8
1554+30		41.22±0.15*	31.4±2.7 [3]	44.6±2.8 [3]	37.1±1.9	-	30.3±2.2	-	10.1±2.9	2.6±1.2	<8
1634+32		46.9±1.6	209.9±2.8 [2]	171.6±5.8 [2]	179.3±1.5	136.5±2.9 [2]	148.3±1.9	116.9±5.7 [2]	35.1±3.3	13.9±2.6	<4
1636+35		86.6±7.0	97.7±2.5 [2]	76.1±2.9 [2]	-	58.1±2.9 [2]	-	48.8±3.9 [2]	29.3±2.0	-	<8
1641+33		83.7±6.4	73.1±2.2 [2]	73.4±2.8 [2]	81.4±0.8	70.6±1.7 [2]	66.1±0.9	61.7±3.6 [2]	26.6±3.3	-	<8
1728+56		190±14	108.6±2.7 [1]	56.4±1.3 [1]	67.2±0.9	34.9±1.7 [1]	35.8±1.4	25.3±3.3 [1]	15.4±1.6	-	**87**
	A	-	-	-	26.6±0.4	-	14.9±0.3	-	4.2±1.1	-	
	B	-	-	-	-	-	-	-	4.9±0.8	-	
	C	-	-	-	-	-	-	-	6.3±0.9	-	
	B+C	-	-	-	40.9±0.5	-	22.3±0.4	-	-	-	
2109−07		59.5±3.2	41.7±2.7 [3]	33.7±2.2 [3]	30.9±0.7	19.9±0.8 [3]	22.6±0.6	15.1±2.8 [3]	-	-	<19
2129+00		51.4±7.6	33.2±1.5 [1]	30.4±3.0 [1]	32.8±0.5	24.2±0.8 [1]	27.4±0.5	21.6±2.6 [1]	10.3±1.6	8.6±2.3	<8
2143+00		41.45±0.10*	38.5±2.4 [3]	53.9±3.3 [3]	50.9±0.6	53.6±1.3 [3]	61.9±0.8	56.9±2.2 [3]	39.4±1.9	26.3±1.8	<4
2238+00		32.2±7.9	-	-	-	-	-	-	<5.4	-	<37
2244+00		34.4±7.1	-	-	24.9±0.7	-	22.2±0.5	-	8.9±1.5	4.9±1.5	<8
2248−09		35.33±0.13*	19.4±1.6 [1]	14.9±2.5 [1]	13.2±0.4	7.9±0.7 [1]	8.1±0.5	7.4±2.0 [1]	-	-	<19
2331+01		41.96±0.13*	38.4±2.0 [1]	28.5±2.5 [1]	25.9±0.5	19.3±0.6 [1]	23.0±0.5	17.9±2.3 [1]	10.7±1.4	<7.5	<8
2346+00		48.4±2.9	41.9±2.5 [2]	47.6±2.1 [2]	49.7±0.6	41.8±4.0 [2]	50.1±0.8	42.7±3.8 [2]	37.1±1.9	16.7±2.6	<4
2353−00		87±17	-	<63 [2]	26.8±0.6	-	18.5±0.5	<29 [2]	7.9±1.8	1.9±0.7	<8

Table 3.5: Low-frequency flux densities (in mJy) from the literature (see Section 4 for references) for the samples of BAL (upper list) and non-BAL (bottom list) QSOs. The subscripts indicate the frequencies in MHz. For VLSS and WENSS, 3-σ upper limits are given for non-detections.

Name	S_{74}^{VLSS}	S_{151}^{6C}	S_{325}^{WENSS}	S_{365}^{TEXAS}	S_{408}^{B3}
0044+00	<300	-	-	-	-
0756+37	<228	-	25.0±3.1	-	-
0816+48	<936	-	62.7±4.5	-	-
0842+06	<267	-	-	-	-
0849+27	453±75	-	-	-	-
0905+02	<360	-	-	-	-
0929+37	<909	-	91.0±3.2	-	100±20
1014+05	<489	-	-	-	-
1040+05	<405	-	-	-	-
1054+51	<201	-	42.5±3.6	-	-
1102+11	<297	-	-	-	-
1103+11	4050±420	-	-	1091±61	810±50
1129+44	<246	-	<13.2	-	-
1159+01	<320	-	418±5.1	492±42	-
1159+06	1140±140	-	-	481±26	-
1229+09	<1032	-	-	-	-
1237+47	<243	-	42.5±2.9	-	-
1304+13	<594	-	-	-	-
1327+03	<288	-	-	-	-
1335+02	<261	-	-	-	-
1337−02	<210	-	-	-	-
1404+07	<309	-	-	-	-
1406+34	<318	-	184.0±3.6	-	-
1603+30	<225	-	33±4.4	-	-
1624+37	<355	-	59±4.0	-	-
0014+01	<303	-	-	-	-
0029−09	<402	-	-	-	-
0033−00	562±95	-	-	-	-
0103−11	<288	-	-	-	-
0124+00	1140±140	-	-	905±56	-
0125−00	4890±530	-	-	1710±110	1590±90
0152+01	<267	-	-	-	-
0154−00	<420	-	-	-	-
0158−00	1730±210	-	-	754±23	-
0750+36	<231	-	24.9±3.4	-	-
1005+48	760±120	630±50	-	492±42	-
1322+50	960±120	520±40	-	421±50	-
1333+47	<246	-	34.3±3.0	-	-
1401+52	<321	-	<10.2	-	-
1411+34	1820±210	830±90	453.6±3.3	360±25	-
1411+43	<237	-	154.7±2.8	-	170±20
1502+55	1480±170	710±40	349.6±3.1	340±19	504±70
1512+35	<333	-	42.3±3.5	-	-
1521+43	<249	-	117.8±3.6	-	120±20
1528+53	1250±150	1020±40	504.8±4.0	534±30	-
1554+30	<219	-	30.1±4.2	-	-
1634+32	<225	-	81.8±4.0	-	-
1636+35	<219	-	<12.6	-	-
1641+33	<195	-	106.1±4.6	-	-
1728+56	1720±220	1250±40	726.9±3.9	734±31	-
2109−07	<354	-	-	-	-
2129+00	<273	-	-	-	-
2143+00	<390	-	-	-	-
2238+00	<351	-	-	-	-
2244+00	<333	-	-	-	-
2248−09	<252	-	-	-	-
2331+01	<288	-	-	-	-
2346+00	<384	-	-	-	-
2353−00	900±130	-	-	-	-

sources are shown in Fig. 3.1 and their linear sizes are listed in Table 3.3 and 3.4.

BAL QSO sample

Amongst the BAL QSO sample, 16 were detected at high angular resolution (3 with resolution 0.47 arcsec, from 43-GHz observations, and 15 with resolution 0.9 arcsec, from 22-GHz observations). Only one of them (1603+30) was resolved at either of these frequencies. Another five sources were observed with a poorer resolution, of 2.3 arcsec (8.46 GHz). For 0849+27, lacking VLA observations from our work, the FIRST data provide the best resolution. A detailed discussion of the four resolved BAL QSOs is presented below.

0816+48

This source is elongated to the south-west in the 1.4-GHz map. A gaussian fit yields an angular size of 29 arcsec along the major axis and an upper limit of 14 arcsec along the minor axis, corresponding to a projected linear size of 217 kpc and <105 kpc respectively. The total spectral index in the range from 4.86 to 8.46 GHz is $\alpha_{4.86}^{8.46} = -0.86 \pm 0.05$ (see Section 4.4 and Table 3.7).

0849+27

0849+27, for which we have no usable VLA observations, is resolved in the FIRST map (resolution of 5 arcsec, see Fig. 2). The map shows three components, located at 25 arcsec NE (D), 34 arcsec NE (B) and 20 arcsec SW (A) from the core (C), which is coincident with the QSO optical position. The four components are included in the FIRST catalogue of radio sources. Throughout the paper, we will label core components as 'C'. The largest separation between components is approximately 44 arcsec, corresponding to a projected linear size of 382 kpc. The total spectral index of the source is $\alpha_{4.86}^{8.46} = -0.73 \pm 0.12$. If the two fainter and farther located NE components are interpreted as a background source, 0849+27 would have a size of 20 arcsec, corresponding to a projected linear size of 173 kpc.

1103+11

1103+11 is resolved at 1.4 (FIRST), 4.86 and 8.46 GHz, and shows a core-lobe morphology. This interpretation is supported by the coincidence of component C with the optical position of the QSO. The angular size from the highest-resolution map (8.46 GHz) is 8 arcsec, corresponding to a projected linear size of 69 kpc. The lobe is not detected at higher frequencies, probably due to the steeper spectral index with respect to the core, which decreases the lobe flux density below the 3-σ detection limit at the highest frequencies. The spectral indices are: $\alpha_{4.86}^{8.46} = -0.37 \pm 0.02$ for the core (C) and $\alpha_{4.86}^{8.46} = -1.32 \pm 0.06$ for the lobe (A), and $\alpha_{4.86}^{8.46} = -0.53 \pm 0.02$ for the total emission.

1603+30

At 22 GHz this source is resolved, showing a core component (C) coincident with the optical position of the QSO and another component towards the south (A), which could be interpreted as a lobe. The angular size is 2 arcsec, corresponding to 17 kpc. The total spectral index of the source is $\alpha_{4.86}^{8.46} = -0.45 \pm 0.13$.

non-BAL QSO sample

For 31 of the 34 sources in the comparison sample, we obtained observations with resolution 0.5 or 0.9 arcsec (frequencies 43 and/or 22 GHz) and for two other two sources we have 8.46-GHz observations with resolution 2.3 arcsec. The highest-resolution observations available for 2238+00 are from FIRST, and the source is unresolved. In total four of the non-BAL QSOs are resolved:

0033-00

This source has core-lobe structure in the 8.46-GHz map. The total angular size is 6 arcsec (51 kpc) and the total spectral index is $\alpha_{4.86}^{8.46} = -0.55 \pm 0.09$.

0125-00

A core-lobe structure is visible in 0125−00 at 4.86 and 8.46 GHz. Since at 4.86 GHz the lobe is not well resolved from the core, we only provide the total flux density (core and lobe) at this frequency in Table 3.4. The angular size, as measured from the 8.46 GHz map, is 5 arcsec, corresponding to 42 kpc. The total spectral index of the source is $\alpha_{4.86}^{8.46} = -0.59 \pm 0.04$.

1411+34

This is a resolved source in the FIRST survey, and our VLA maps at 4.86 and 8.46 GHz show a core and double-lobe, with angular size at 8.46 GHz of 23 arcsec (199 kpc). At 22 and 43 GHz only the core is detected. The spectral indices are $\alpha_{4.86}^{8.46} = 0.11 \pm 0.03$ for the core, $\alpha_{4.86}^{8.46} = -1.32 \pm 0.54$ for lobe A and $\alpha_{4.86}^{8.46} = -2.04 \pm 0.25$ for lobe B. The total spectral index is $\alpha_{4.86}^{8.46} = 0.02 \pm 0.13$.

1728+56

1728+56 is a double source at 4.86 and 8.46 GHz. At 22 GHz, a core component is also detected, and is coincident with the optical position of the QSO. The B and C components, which are resolved at 22 GHz, are blended at the lower frequencies. The angular size (separation of A and B) at 22 GHz is 10 arcsec, corresponding to 87 kpc. The spectral index calculation for the A component yields $\alpha_{4.86}^{8.46} = -1.04 \pm 0.04$ and for B+C $\alpha_{4.86}^{8.46} = -1.09 \pm 0.04$, indicating that the lobe emission dominates. For the total emission we found

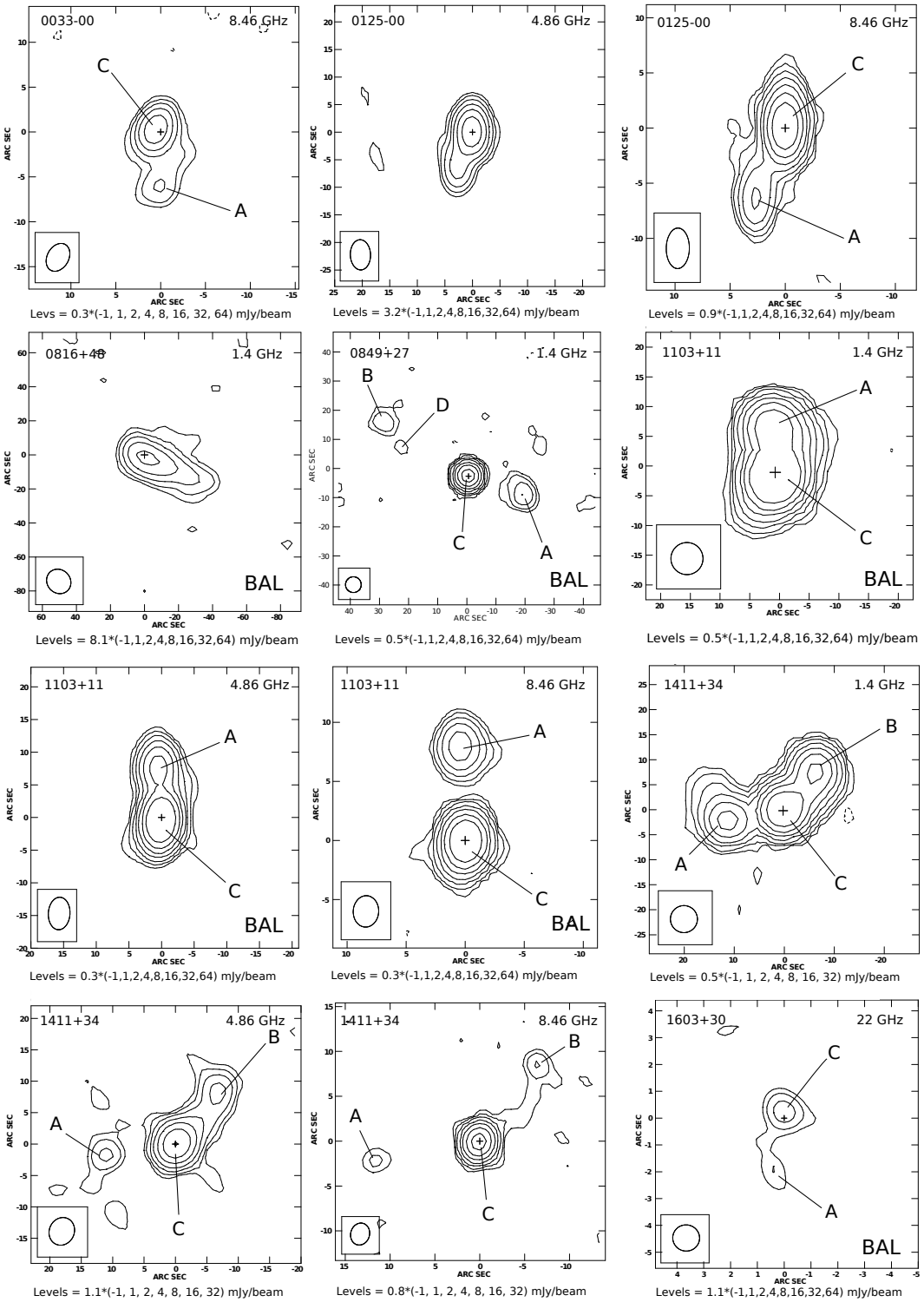

Figure 3.1: Maps of the resolved QSOs. The synthesised beam size is shown in the lower left corner of the map. Levels are multiples of the 3-σ flux density value in mJy/beam, according to the legend. A cross indicates the SDSS optical position.

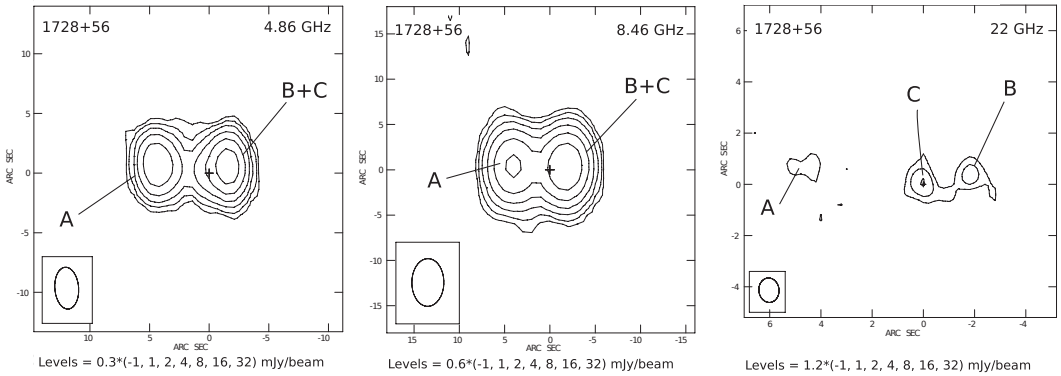

Figure 3.1: Continued.

a spectral index $\alpha_{4.86}^{8.46} = -1.14 \pm 0.07$.

In summary, we found from our multi-wavelength observations only eight resolved sources out of 59. The fractions of resolved sources in the two samples are similar, as are the ranges of angular sizes, from 20 to 200-400 kpc. The morphologies of the BAL QSOs include one extended source, two core-lobe and an ambiguous case between core-lobe and core double-lobe. The morphologies of the non-BAL QSOs include two core-lobe and two core double-lobe sources. The fraction of unresolved sources is 21/25=84% for the BAL QSOs and 30/34=88% for the non-BAL QSOs. 20 of the unresolved BAL QSOs and 27 of the unresolved non-BAL QSOs have been observed at the VLA at 8.46 GHz, with 2.3 arcsec resolution. These data indicate that most of the QSOs in the two samples have sizes below 20 kpc at 8 GHz, using the average redshift $z = 2.4$ of the two samples. Individual upper limits for the sources linear sizes are given in Table 3.3 and 3.4. Two of the unresolved BAL QSOs, 1159+01 and 1624+37, were resolved by VLBA (Montenegro-Montes et al. 2008b, 2012), both showing a core-jet morphology with sizes of 0.85 kpc and 60 pc respectively.

It has been suggested that up to 25% of compact radio sources can intrinsically be extended sources, viewed as being compact due to their orientation (Fanti et al. 1990). Our sample includes only QSOs, which are usually considered to be active galactic nuclei seen from a particular range of viewing angles, from a few degrees up to ∼45° from the jet axis (limit imposed by the presence of the dusty torus). This, in principle, could increase the contamination, if we consider, as do Fanti et al., that a viewing angle <20°-30° can significantly reduce the projected linear size of a source.

3.2.2 Variability

We have observations at 4.8 GHz and at 8.4 GHz at both the VLA and Effelsberg-100m. This allow us to evaluate the variability of the sources in

the sample for each couple of measurements, through the calculation of the fractional variability and significance. For the sources resolved in the VLA maps (see Sect. 4.1) we used the total flux densities. We adopted the fractional variability index defined by Tornianien et al. (2005) as:

$$Var_{\Delta S} = \frac{S_{max} - S_{min}}{S_{min}} \tag{3.3}$$

The significance of the source variability was estimated using the σ_{Var} parameter as defined e.g. by Zhou et al. (2006),

$$\sigma_{Var} = \frac{|S_2 - S_1|}{\sqrt{\sigma_1^2 + \sigma_2^2}} \tag{3.4}$$

where S_i and σ_i are the flux density and its corresponding uncertainty. We consider as candidate variable sources those with $\sigma_{Var} \geq 4$ and a fractional variability $\geq 20\%$. In the following we briefly discuss these cases.

Regarding the BAL QSO sample, 20 sources have the two measurements at 4.8 GHz and 17 have the two measurements at 8.4 GHz (16 of them in common with the first group). In four cases we found $\sigma_{Var} > 4$ and these sources are listed in Table 3.6, where the flux densities, variability significance, fractional variability and time interval are presented. None of these sources exceeds the limit of 20% fractional variability.

30 of the sources in the comparison sample were observed at Effelsberg and the VLA at 4.8 GHz, and for 25 of them also both measurements are available at 8.4 GHz. Seven of the sources have variability significance above 4 at one or both frequencies and they are listed in Table 3.6. 1005+48 shows modest variability, just at the considered threshold. 0029−09 and 1521+43 show both a high variability significance, $\sigma_{Var} > 10$, and a high fractional variability, $\sim$ 40-50 per cent, with 1521+43 being the most extreme case, showing in fact large variations at the two frequencies. The remaining variable source, 1411+34, is resolved at the VLA (see Sect. 4.1). It shows variations at the two frequencies at a level 20-40 % with significance 5-7σ. Since for this case we found the lower flux densities at the higher resolutions, the measured variability for this source could be due to resolution effects and therefore it cannot be considered as a bona fide intrinsic variable candidate.

Summarizing the results from the comparison between VLA and Effelsberg data, we found three sources with likely intrinsic variability, 0029−09, 1005+48 and 1521+43, all of them in the comparison sample. 1411+34 (non-BAL QSO sample) shows flux density variations that could be due to resolution effects. Given the low number of variable sources, it is not possible to firmly state whether BAL and non-BALs have different variability behaviour, although our data suggest a lower fraction of variables for the BAL QSO sample.

The BAL QSOs 1159+01, 1603+30 and 1624+37 were also included in the Montenegro-Montes et al. (2008a) sample. We studied the possible variability of these sources comparing the flux densities at various frequencies in this work with those reported at Montenegro-Montes et al. (2008a), considering the same

Table 3.6: Sources with significant variability, $\sigma_{Var} > 4$, from the observations in this paper. 'BAL' in the last column indicates that the QSO is from the BAL QSO sample.

Name	4.8 GHz				8.4 GHz				Elapsed time	
	S_{Eff}	S_{VLA}	σ_{Var}	$Var_{\Delta S}$	S_{Eff}	S_{VLA}	σ_{Var}	$Var_{\Delta S}$		
0029−09	-	-	-	-	39.6±1.0	54.7±0.7	12.4	0.38	21 d	
0756+37	209.6±2.6	226.2±2.0	5.1	0.08	-	-	-	-	1.6 yr	BAL
1005+48	-	-	-	-	69.9±3.2	83.6±1.1	4.1	0.20	1.6 yr	
1103+11	-	-	-	-	65.9±1.1	75.0±0.8	6.7	0.14	1.6 yr	BAL
1327+03	67.7±1.9	79.5±1.7	4.6	0.17	-	-	-	-	1.6 yr	BAL
1404+07	-	-	-	-	173.6±2.4	189.6±2.2	4.9	0.09	1.6 yr	BAL
1411+34	120.2±1.9	85.1±5.2	6.3	0.41	105.1±1.9	86.3±2.9	5.4	0.22	1.6 yr, 1.6 yr	
1521+43	256.8±2.8	387.3±3.0	31.8	0.51	346.9±4.4	523.1±5.7	24.5	0.51	1.6 yr, 1.6 yr	
1728+56	56.4±1.3	67.2±0.9	6.8	0.19	-	-	-	-	1.6 yr	
2143+00	-	-	-	-	53.6±1.3	61.9±0.8	5.4	0.15	21 d	
2331+01	-	-	-	-	19.3±0.6	23.0±0.5	4.7	0.19	1.6 yr	

radiotelescope (Effelsberg or VLA). Most of the flux densities for 1624+37 presented at Montenegro-Montes et al. (2008a) were taken from Benn et al. (2005).

For 1159+01 we found $\sigma_{var} > 4$ in the comparison of VLA data at the frequencies of 8.4 GHz and 22 GHz, although in the first case yielding a low fractional variability, of 9%. At 22 GHz the flux density variation is important, with σ_{var}=21 and fractional variability 60%. The variations could be due to resolution effects, since both correspond to an increase in flux density from the VLA A configuration data (HPBW=0.08 arcsec) from Montenegro-Montes et al. (2008a) to the lower resolution VLA C configuration data (HPBW=0.9 arcsec) for this work. The flux densities varied from 160.8±1.25 mJy to 176.6±2.2 at 8.4 GHz, and from 105.5±1.15 mJy to 169.2±2.8 mJy at 22 GHz, in a time interval of 4.5 years.

For 1603+30 we could compare 2.6 and 4.8 GHz Effelsberg data as well as 8.4 and 22 GHz VLA data. We found σ_{var}=4.9 and fractional variability 49% for the 4.8 GHz Effelsberg data, over a 4.5 years interval, indicating significant intrinsic variability. For the 8.4 GHz VLA data there is a flux density variation from 22.1 ± 0.35 mJy at VLA(A) to 26.9 ± 0.6 mJy for VLA(C), in 3.4 years. The variation is significant, $\sigma_{var} = 6.9$ and fractional variability 22%, although we cannot reject that resolution effects play a role. However, the variability at this frequency is confirmed by Montenegro-Montes et al. (2008a), where the source is listed as a variable candidate (significance 4.2 and fractional variability 22%) from the comparison between the flux densities from their data and those from Becker et al. (2000), both from VLA in A configuration.

Regarding 1624+30, although the comparison of flux densities was possible at four frequencies (4.8 GHz Effelsberg and 8.4, 10.5 and 22 GHz VLA), none of them yielded $\sigma_{var} > 4$. Therefore, from the comparison with the flux densities in Montenegro-Montes et al. (2008a), only 1603+30 is a candidate variable.

In total four sources, one BAL QSO and three non-BAL QSOs, are classified as intrinsic variables (not due to resolution effects) at levels above 20% (0029−09, 1005+48, 1521+43 and 1603+30). The additional data from Montenegro-Montes et al. (2008a) weaken the trend of BAL QSOs being less variable than

non-BAL QSOs.

Barvainis et al. (2005) studied the flux density variability at 8.4 GHz over 10 epochs (with time spacings for each source ranging from two weeks to 1.6 years) of a core dominated sample of 50 QSOs with $S_{8.4\ \mathrm{GHz}} \geq 0.3$ mJy, including radio-quiet, radio-loud and radio-intermediate QSOs. 38 of the QSOs in their sample (76%) have a flat radio spectrum, with $\alpha_{4.8}^{8.4} \geq -0.5$. The authors found five QSOs with fractional variability above 20%, specifically four of them in the range 20–40% and the other one with fractional variability of 140%. The four QSOs with higher variability have flat spectra, whereas the remaining one is steep.

The fraction of variable sources at a level around 20% obtained by Barvainis et al. (2005) (5/50) is consistent with our results for the SDSS-FIRST QSOs, (4/59), within the errors. In addition, we will show in Sect. 4.4 that the variable sources in our work also have a flat spectrum in the frequency range from 5 to 8 GHz, although our sample has a lower fraction of flat sources (25/59 = 42%, see Sect. 4.4 and Table 3.7), compared to 76% in the Barvainis et al. (2005) sample. This inferior fraction of flat sources could also explain the slightly lower fraction of variables in our work with respect to their results.

Sadler (2006) investigated the variability at 20 GHz over a 1-2 years period of a sample of radio sources selected at this frequency, with $S_{20\ \mathrm{GHz}} \geq 100$ mJy and including 32 QSOs. The QSO sub-sample is dominated by flat spectrum sources (69% with $\alpha_5^8 \geq -0.5$) and has two sources just above the 20% fractional variability threshold (2/32). Although the number of sources in this sample seems poor for statistics, the proportion of variable sources is consistent with the results from Barvainis et al. (2005) and from our work. We note however that the two QSOs in Sadler (2006) with variability above 20% do not have flat spectra (their spectral indices being $\alpha_5^8 = -0.59$ and $\alpha_5^8 = -0.53$).

3.2.3 Shape of the radio spectra

Taking advantage of the collected multi-frequency SEDs, it is possible to study the shape of the synchrotron emission of the quasars in the two samples, allowing us to obtain the fraction of CSS-GPS sources. GPS sources are compact ($\leq$1 kpc) and have a convex radio spectrum that peaks between 500 MHz and 10 GHz in the observer's frame, CSS are larger (between 1 and 20 kpc in size) and have convex spectra peaking at lower frequencies, typically <500 GHz (O'Dea 1998). The SEDs of the sources are shown in Figure 3 as $\log S_\nu$ versus $\log\nu$ plots, using the flux densities listed in Tables 3.3, 3.4 and 3.5. For resolved sources we used the total flux densities.

The SEDs of the sources with observations at various frequencies were fitted through χ^2 minimization on the $\log S_\nu$ versus $\log\nu$ plane, using a power-law model (L) and a parabola (P). A fit was accepted as statistically significant if the parameter Q, indicating the probability that a value of χ^2 as poor as the value found should occur by chance, was above 0.01. The parabolic model was chosen as a simple representation for the SEDs curved on the $\log S_\nu$ vs.

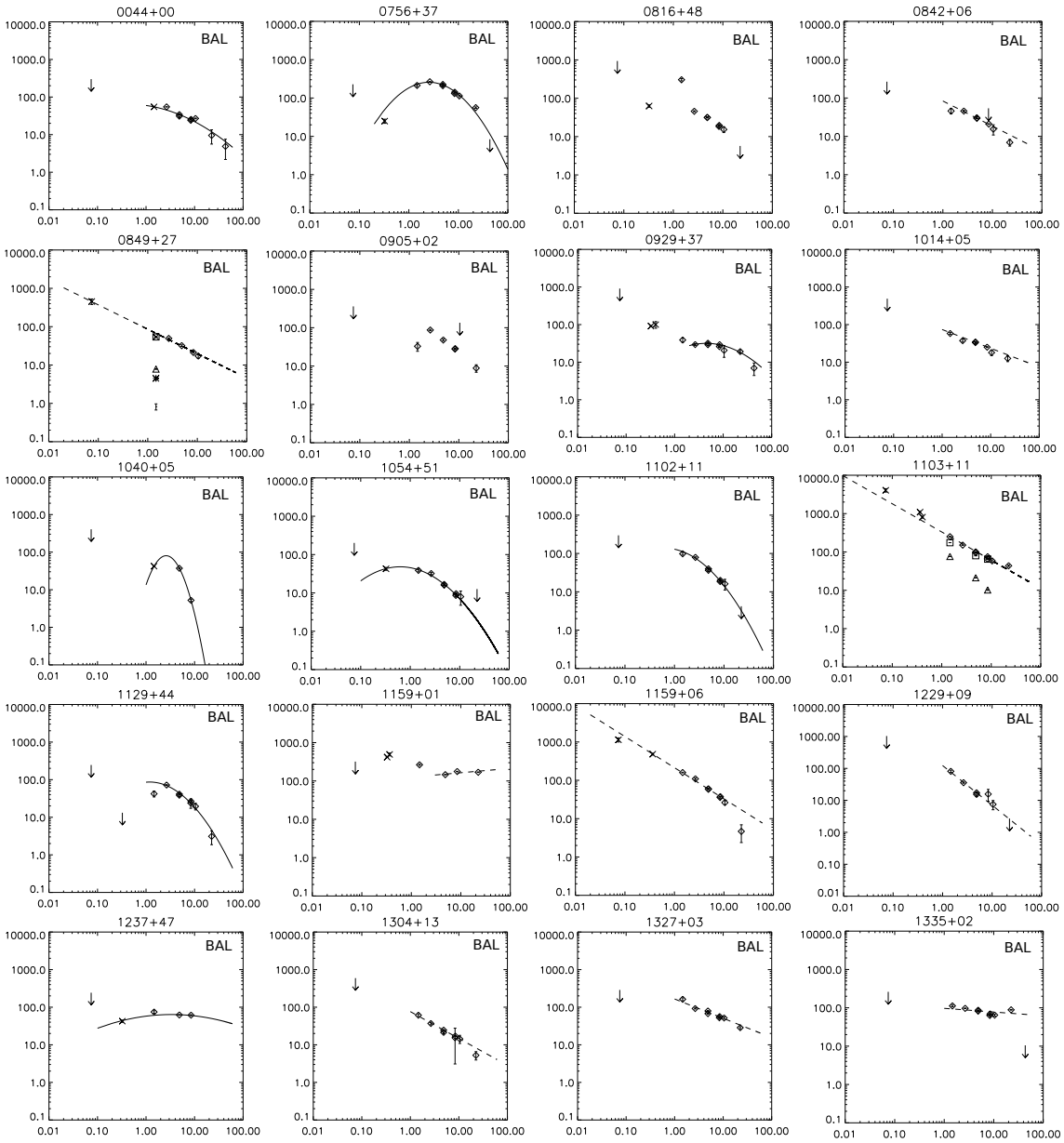

Figure 3.2: Radio spectra of the 25 BAL and 34 non-BAL QSOs (GHz on x-axis, mJy on y-axis). Error bars are shown if larger than the symbol size. Crosses represent flux densities from the literature, rhombi are flux densities from our observational campaign and arrows are upper limits from the literature. Solid lines are fits to a parabola and dashed lines are fits to a power-law. For resolved sources flux densities are presented as follows: a square for C component (core) and triangle, asterisk and dot for components A, B and D respectively (see Tables 3.3 and 3.4). For 1728+56 the flux densities at 4.8 and 8.4 GHz shown as asterisks correspond to the B+C components.

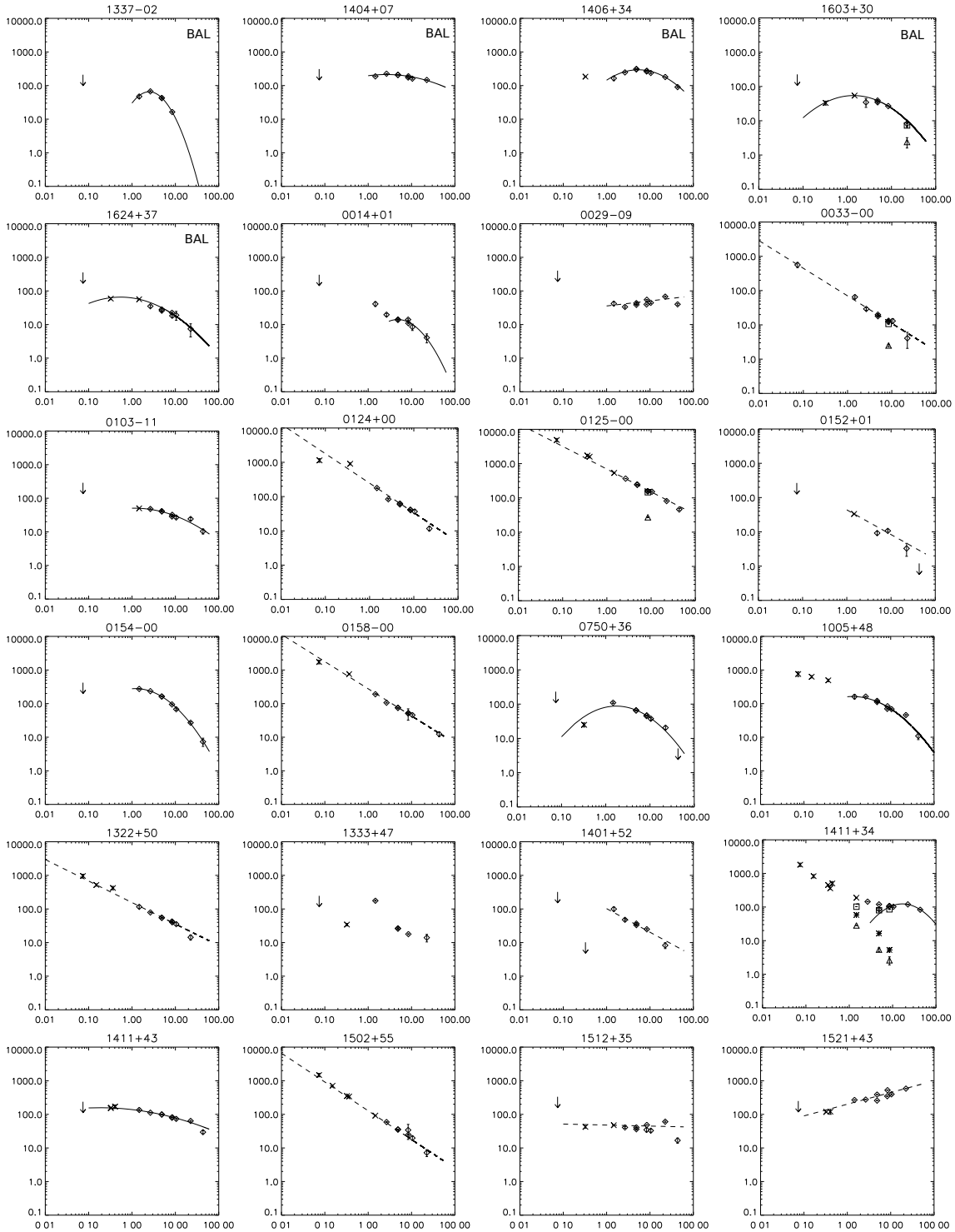

Figure 3.2: Continued.

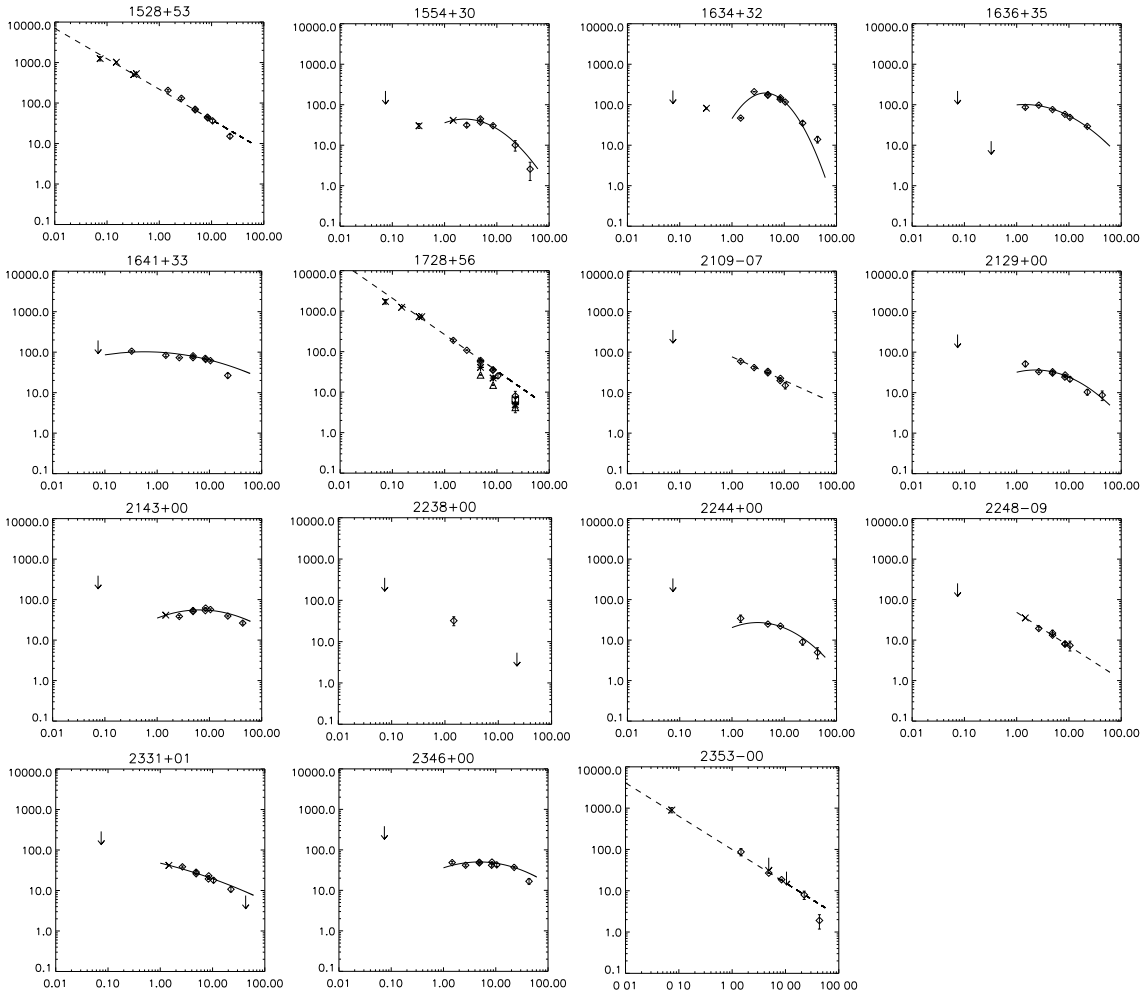

Figure 3.2: Continued.

logν plane, following Kovalev (1996). For the cases where the two models were statistically accepted, the power-law was selected as the best fit. The fits are shown in Fig. 3 using a dotted line for the power-law model and a continuous line for the quadratic model.

For a total of ten sources (BAL QSOs 0842+06, 0849+27, 1014+05, 1229+09 and 1304+13, and non-BAL QSOs 0033−00, 1401+52, 2109−07, 2248−09 and 2353−00) we found statistically significant fits as power laws, and these sources are labelled as L_Q in Table 3.7, where the fitting results are presented. For six further sources we found a statistically significant fit for the parabolic model (BAL QSOs 1054+51, 1102+11, 1337−02 and 1603+30, non-BAL QSOs 0154−00 and 1636+35). All these fits are convex, i.e. showing a flattening from high (10-20 GHz) to mid (1-5 GHz) frequencies. These sources are labelled as P_Q in Table 3.7. Although BAL QSO 1159+06 also fall in this category, we adopted for the source the linear model, since the peak of the parabola is far away from the observed frequencies, the linear and parabolic model being practically coincident over the observed range. We adopt the label *L* in Table 3.7 for this source.

For the other 29 sources at least one of the models shows a good match from visual inspection, and we selected as the best model the one yielding the lowest mean squared error, labelling the sources as L or P in Table 3.7. The linear model includes six sources (BAL QSO 1327+03 and non-BAL QSOs 0029−09, 0152+01, 0158−00, 1322+50 and 1512+35), and the parabolic model 15 sources (BAL QSOs 0044+00, 0756+37, 1129+44, 1237+47, 1404+07 and 1624+37 and non-BAL QSOs 0103−111, 0750+36, 1411+43, 1641+33, 2129+00, 2143+00, 2244+00, 2331+01 and 2346+00), all of them with convex shape. Although the remaining eight sources have the lowest mean squared error for the quadratic model, we adopted the linear fit, also with a low mean squared error, because either the peak was far away from the SED, making the linear and quadratic model very similar, or the parabolic shape was concave, which is inconsistent with the expected shapes from synchrotron models. As for 1159+06, described in the previous paragraph, we used the italic label *L* for these sources (BAL QSOs 1103+11 and 1335+02, and non-BAL QSOs 0124+00, 0125−00, 1502+55, 1521+43, 1528+53 and 1728+56). For the sources modelled with a parabola with its peak within the fitted range, the frequency peaks are listed in Table 3.7.

Other three sources were not fitted, since they showed abrupt changes in their SEDs (BAL QSOs 0816+48 and 0905+02, and non-BAL QSO 1333+47).

Other eight sources (BAL QSOs 0929+37, 1159+01, 1406+34, and non-BAL QSOs 0014+01, 1005+48, 1411+34, 1554+30, 1634+32) have SEDs that suggest the presence of a separate component at low frequency. In fact 1411+34 was also morphologically resolved as a core double-lobe with the two lobes steeper, i.e. stronger at low frequencies, than the core (see Sect. 4.1). For these sources we considered then fits removing one or various of the lowest frequency data points, with hints of excess emission. The low frequency points rejected for the fits are indicated in Table 3.7. Regarding the high frequency

components, six of the sources belong to class P and another one to class P_Q, all with convex shape. The SED of 1159+01 shows hints of excess emission from 325 MHz to 1.4 GHz, leaving only three high frequency data points. Since the power law fit gives a low mean squared error we adopted this model for the source. For the cases where the high frequency component was modelled as a parabola with its peak within the fitted range, the frequency peaks are listed in Table 3.7, using italic digits. However, these sources cannot be considered as CSS-GPS candidates, because of the presence of the secondary low-frequency emission. The fraction of QSOs with hints of an additional low frequency component (up-turns at low frequency) is $12 \pm 7\%$ for BAL QSOs (3/25) and $15 \pm 7\%$ for non-BAL QSOs (5/34), the two values being similar within the errors. Since this low-frequency excess emission likely corresponds to old components, this result favours similar ages for BAL and non-BAL QSOs.

The remaining sources in the sample are 1040+05 (BAL QSO) and 2238+00. For 1040+05 only three data points are available, with an obvious flattening at low frequencies, and we selected as best model the parabola passing through these points. 2238+00 has a good quality measurement only at one frequency.

In total we found nine BAL QSOs and 16 non-BAL QSOs whose complete SEDs have reasonable fits with power laws. For 11 BAL QSOs and 11 non-BAL QSOs best fits are with a curved shape along the whole SED due to a flattening of the spectra at low frequencies. For 15 of these (eight BAL QSOs and seven non-BAL QSOs) the frequency peak of the model parabola falls within the fitted range, with values ranging from 500 MHz to 7 GHz in the observer frame, indicating that they represent candidate GPS sources. Three sources that were not fitted due to abrupt changes in their SEDs have a maximum within the observed frequency range with frequency peaks above 1 GHz. In addition, although BAL QSO 1129+44 is fitted with a parabola with its peak below the observed frequency range, the flux density distribution shows a peak at 2.6 GHz. Among these 19 sources whose SED is Giga-Hertz peaked, two of them are resolved, BAL QSOs 0816+48 and 1603+30, with sizes of 217 kpc and 17 kpc respectively (see Sec. 4.1), exceeding the typical size of 1 kpc for GPS sources (O'Dea 1998). Excluding these two sources the total number of candidate GPS sources would be of 9 BAL QSOs and 8 non-BAL QSOs, with corresponding fractions with respect to the total samples of $36 \pm 12\%$ (9/25) and $23 \pm 8\%$ (8/34), adopting Poisson errors. In Sec. 4.1 we obtained for the unresolved sources a conservative upper limit of 20 kpc for their sizes at 8.4 GHz, therefore higher resolution observations are needed to confirm the GPS classification. In particular, this classification is confirmed for 1624+37, with a size of 60 pc at 5 GHz and 75 pc at 8 GHz (Montenegro-Montes et al. 2008b, 2012 in preparation). The fraction of GPS candidates in the BAL QSO and non-BAL QSO samples is similar, within the errors. Considering the interpretation that GPS sources are young, our results are consistent with the hypothesis that BAL QSOs are not a younger population than non-BAL

QSOs.

We adopted a conservative approach in the quantification of young objects, since only candidate GPS sources were considered for that purpose, but also CSS objects, showing a steep spectrum in the GHz frequency range, with peak frequencies below 500 MHz, can be interpreted as young sources. Additional observations at low-frequency could confirm the presence of peaks in the MHz frequency range for some of the sources in this work. In fact the maximum size for CSS is 20 kpc (O'Dea 1998) and most of the sources in this work are unresolved with sizes below this limit.

3.2.4 Spectral indices

The spectral index can be a statistical indicator of the orientation of radio sources (Orr & Browne 1982), so we can use this quantity to determine whether BAL QSOs have a particular orientation or not. Spectral indices of the QSOs were computed in the observed frequency intervals 4.8-8.4 GHz and 8.4-22 GHz, since these frequencies exceed the typical peak frequencies of the candidate GPS sources in the sample. We used the total flux densities for the resolved sources and VLA data, which were obtained during a one week run (see Table 3.1). Effelsberg flux densities were adopted for the few sources/frequencies lacking VLA data (BAL QSOs 0849+27 and 1229+09 and non-BAL QSOs 0154−00 and 1636+35). The spectral indices and their errors are listed in Table 3.7.

Figure 3.3 (top and middle panels) show $\alpha_{8.4}^{22}$ versus $\alpha_{4.8}^{8.4}$ for the two samples. The square symbols correspond to sources without available spectral index $\alpha_{8.4}^{22}$. They were plotted using the mean $\alpha_{8.4}^{22}$ of each sample. Upper limits are plotted as triangles. The dashed line traces pure power-laws: the location of most of the sources below this line is due to the steepening at high frequencies. The spectral indices of the BAL QSOs show a large scatter in the plot. From a statistical analysis of the spectral indices we obtained the following results:

- Although in Fig. 3.3 most BAL QSOs are found in the same region as non-BAL QSOs, there is an apparent excess of steep sources in the BAL QSO sample, with six sources showing spectral indices below -1.5 at either of the two frequency ranges. In addition, there appears to be an excess of non-BAL QSO sources with $\alpha_{4.8}^{8.4} > 0$. However, the distribution of each of the spectral indices is the same for the BAL and non-BAL QSO samples according to the Kolmogorov-Smirnov (K-S) test, for which the distributions are different only at a significance level of 74% for $\alpha_{4.8}^{8.4}$ and 0.3% for $\alpha_{8.4}^{22}$. Considering the test that the distribution of spectral indices is steeper for BAL QSOs than for non-BAL QSOs, the significance levels increase to 87% for $\alpha_{4.8}^{8.4}$ and to 28% for $\alpha_{8.4}^{22}$.

- It is useful to test the hypothesis that BAL QSOs are flatter than non-BAL QSOs. This hypothesis can be rejected at a 100% confidence level for $\alpha_{4.8}^{8.4}$ and at 77% confidence level for $\alpha_{8.4}^{22}$. Although we do not find

Table 3.7: Radio spectral shape and spectral indices of the QSO sample

Name	Fit type	ν_{peak} (GHz)	ν^{rest}_{peak} (GHz)	ν_{rej} (GHz)	$\alpha^{8.4}_{4.8}$	$\alpha^{22}_{8.4}$	log10($L_{4.8\ \mathrm{GHz}}$) (W Hz^{-1})	
(1)	(2)	(3)	(4)	(5)	(6)	(7)	(8)	(9)
0044+00	P	-	-	-	−0.53±0.10	−1.01±0.29	26.89	BAL
0756+37	P	2.5	8.7	-	−0.84±0.03	−0.95±0.05	27.97	BAL
0816+48	-	-	-	-	−0.86±0.05	≤ −1.26	27.47	BAL
0842+06	L_Q	-	-	-	−0.62±0.05	−1.13±0.21	26.94	BAL
0849+27	L_Q	-	-	-	−0.73±0.12	-	26.69	BAL
0905+02	-	-	-	-	−0.93±0.13	−1.20±0.23	27.01	BAL
0929+37	P_Q	*4.5*	*13.1*	0.325, 0.408, 1.4	−0.16±0.04	−0.44±0.08	26.53	BAL
1014+05	L_Q	-	-	-	−0.57±0.05	−0.70±0.18	26.80	BAL
1040+05	P_Q	2.6	8.8	-	−3.55±0.15	-	28.61	BAL
1054+51	P_Q	0.6	2.0	-	−0.93±0.13	≤ 0.29	26.79	BAL
1102+11	P_Q	-	-	-	−1.25±0.07	≤ −1.59	27.36	BAL
1103+11	*L*	-	-	-	−0.53±0.02	−0.55±0.04	27.11	BAL
1129+44	P	-	-	-	−0.67±0.16	−2.20±0.40	26.98	BAL
1159+01	L	-	-	0.325, 0.365, 1.4	0.34±0.03	−0.04±0.02	26.98	BAL
1159+06	*L*	-	-	-	−0.80±0.05	−2.15±0.51	27.22	BAL
1229+09	L_Q	-	-	-	−0.17±0.73	≤ −1.80	26.53	BAL
1237+47	P	3.4	11.1	-	−0.02±0.05	-	26.88	BAL
1304+13	L_Q	-	-	-	−0.66±0.06	−1.20±0.25	26.93	BAL
1327+03	L	-	-	-	−0.62±0.04	−0.70±0.07	27.50	BAL
1335+02	*L*	-	-	-	−0.40±0.04	0.25±0.02	27.04	BAL
1337−02	P_Q	2.5	10.2	-	−1.73±0.06	-	27.99	BAL
1404+07	P	2.6	10.1	-	−0.15±0.03	−0.26±0.02	27.66	BAL
1406+34	P	*5.4*	*19.2*	0.325	−0.22±0.03	−0.44±0.02	27.79	BAL
1603+30	P_Q	1.4	4.2	-	−0.45±0.13	−1.04±0.14	26.75	BAL
1624+37	P	0.5	2.2	-	−0.78±0.29	−0.92±0.44	27.32	BAL
0014+01	P	*4.8*	*15.3*	1.4, 2.6	−0.46±0.09	−1.02±0.31	26.43	
0029−09	L	-	-	-	0.63±0.06	0.22±0.04	26.44	
0033−00	L_Q	-	-	-	−0.55±0.09	−1.19±0.50	26.39	
0103−11	P	-	-	-	−0.41±0.04	−0.29±0.09	26.87	
0124+00	*L*	-	-	-	−0.80±0.06	−1.27±0.14	27.09	
0125−00	*L*	-	-	-	−0.59±0.04	−0.78±0.03	27.77	
0152+01	L	-	-	-	0.27±0.28	−1.20±0.41	26.12	
0154−00	P_Q	-	-	-	−0.97±0.06	−1.28±0.07	27.56	
0158−00	L	-	-	-	−0.64±0.03	-	27.42	
0750+36	P	1.7	5.1	-	−0.60±0.03	−0.85±0.11	27.10	
1005+48	P	-	-	0.074, 0.151, 0.365	−0.67±0.03	−0.62±0.04	27.55	
1322+50	L	-	-	-	−0.58±0.04	−1.06±0.19	26.87	
1333+47	-	-	-	-	−0.68±0.06	−0.25±0.26	26.98	
1401+52	L_Q	-	-	-	−0.52±0.09	−1.12±0.20	27.11	
1411+34	P	*16.8*	*47.4*	0.074 - 4.86	0.02±0.13	0.34±0.04	26.83	
1411+43	P	-	-	-	−0.35±0.03	−0.26±0.03	27.55	
1502+55	*L*	-	-	-	−0.64±0.05	−1.27±0.24	27.31	
1512+35	L	-	-	-	0.30±0.04	0.23±0.05	26.52	
1521+43	*L*	-	-	-	0.54±0.02	0.11±0.02	27.36	
1528+53	*L*	-	-	-	−0.89±0.10	−1.07±0.10	27.61	
1554+30	P	*2.4*	*8.8*	0.325	−0.36±0.16	−1.12±0.30	26.98	
1634+32	P	*4.3*	*14.4*	0.325	−0.34±0.03	−1.47±0.10	27.53	
1636+35	P_Q	1.4	4.1	-	−0.49±0.11	−0.70±0.09	27.05	
1641+33	P	0.6	2.2	-	−0.38±0.03	−0.93±0.13	27.35	
1728+56	*L*	-	-	-	−1.14±0.07	−0.86±0.11	27.22	
2109−07	L_Q	-	-	-	−0.56±0.06	-	26.68	
2129+00	P	2.3	9.1	-	−0.32±0.04	−1.00±0.16	26.99	
2143+00	P	6.6	20.1	-	0.35±0.03	−0.46±0.05	26.53	
2244+00	P	3.1	12.2	-	−0.21±0.06	−0.93±0.17	26.79	
2248−09	L_Q	-	-	-	−0.88±0.12	-	26.58	
2331+01	P	-	-	-	−0.21±0.05	−0.78±0.14	26.73	
2346+00	P	4.9	13.7	-	0.01±0.04	−0.31±0.05	26.58	
2353−00	L_Q	-	-	-	−0.67±0.06	−0.87±0.23	26.68	

Notes: Column 2: Best-fitting function is specified (L for linear, P for parabolic, see Sect. 4.3); cols. 3 and 4: Peak frequencies (observer and rest-frame); col. 5: Frequencies of the rejected flux densities for the fits (if any); cols 6-7: Observer-frame spectral indices; col. 8: Radio luminosity; col. 9: Indication whether the source is a BAL QSO.

statistical evidence of steeper spectra for BAL QSOs, we can firmly reject that BAL QSOs have on average flatter radio spectra than non-BAL QSOs, in the frequency range 4.8-8.4 GHz.

- Figure 3.3 (bottom panel) shows the same spectral index diagram for the BAL QSOs in Montenegro-Montes et al. (2008a). BAL QSOs 1159+01, 1603+30 and 1624+37, which are common to both samples, were plotted with a different symbol (circles with their size increasing with the right ascension of the sources). From the combined sample of BAL QSOs from this work and Montenegro-Montes et al. (2008a) (using our data for the sources in common), we find that the hypothesis that BAL QSOs have steeper $\alpha_{4.8}^{8.4}$ than non-BAL QSOs has a higher confidence level, of 91%, although still below the threshold of 95% generally adopted for the rejection of the null hypothesis. It is important to note that in this test we are using the comparison sample selected for this work, with $S_{1.4} > 30$ mJy, which is a higher value than the limit of Montenegro-Montes et al. (2008a) sample, of 15 mJy. Regarding $\alpha_{8.4}^{22}$, the combined sample of BAL QSOs is steeper than the non-BAL QSO sample only at a 55% confidence level.

- The hypothesis that the BAL QSOs in the combined sample are flatter than non-BAL QSOs can be rejected at a 97% confidence level for $\alpha_{4.8}^{8.4}$ and at 98% confidence level for $\alpha_{8.4}^{22}$. Although the evidence of steeper spectra for BAL QSOs is at most marginal, with 91% significance for the test between the combined BAL sample and the comparison sample at the frequency range 4.8-8.4 GHz, we can reject with a high confidence, above 97%, that BAL QSOs have on average flatter radio spectra than non-BAL QSOs, both in the frequency ranges 4.8-8.4 GHz and 8.4-22 GHz. We interpret this result as statistical evidence that the BAL QSOs in our sample, or in combination with Montenegro-Montes et al. (2008a) sample, do not tend to have position angles closer to the radio axis than non-BAL QSOs, i.e. the orientation models for BAL QSOs in which they predominantly arise from polar winds (for instance Punsly 1999a,b), are in contradiction with our results. At a lower significance level, the slightly steeper spectra of BAL QSOs compared to non-BAL QSOs in the range 4.8-8.4 GHz are consistent with the equatorial wind model of Elvis (2000).

Figure 3.4 shows histograms of the distributions of $\alpha_{4.8}^{8.4}$ and $\alpha_{8.4}^{22}$ for the BAL and non-BAL QSO samples. The basic statistics for the spectral indices $\alpha_{4.8}^{8.4}$ and $\alpha_{8.4}^{22}$ of the BAL and non-BAL samples is presented in Table 3.8. The spectral indices in the two frequency ranges show a mixture of flat ($\alpha \geq -0.5$) and steep ($\alpha < -0.5$) spectra for the BAL and non-BAL QSO samples (see also Table 3.7). The values found for BAL QSOs suggest that these QSOs are seen from a wide range of orientations with respect to the jet axis (both flat and steep sources are present). The same conclusion that BAL QSOs are not

Table 3.8: Spectral-index statistics for various QSO samples: the BAL and non-BAL QSO samples presented in this paper ('BAL', 'non-BAL'), the BAL QSO sample presented in Montenegro-Montes et al. (2008a), and the comparison QSO sample from Vigotti et al. (1997, 1999)

	$\alpha_{4.8}^{8.4}$						$\alpha_{8.4}^{22}$					
	N	min	max	median	mean	std	N	min	max	median	mean	std
BAL	25	−3.55	0.34	−0.62	−0.71	0.72	20	−2.20	0.25	−0.92	−0.86	0.64
BAL+MM08	37	−3.55	0.76	−0.62	−0.66	0.70	32	−2.20	0.25	−0.93	−0.93	0.54
non-BAL	33	−1.14	0.63	−0.49	−0.39	0.43	30	−1.47	0.34	−0.87	−0.74	0.50
B3-VLA QSOs[1] (<2.3")	40	−1.38	0.54	−0.65	−0.57	0.47	-	-	-	-	-	-
B3-VLA QSOs[1] (all)	123	−2.23	0.54	−0.89	−0.79	0.45	-	-	-	-	-	-

[1] The spectral index for this sample is $S_{4.8}^{10.6}$.

oriented along a particular line of sight was obtained from Becker et al. (2000) and Montenegro-Montes et al. (2008a), also on the basis of the radio spectral index of BAL QSOs. The comparison in our work with a control sample similar in redshift, and radio and optical properties, except for the absence of broad absorption features, reveals a weak tendency for BAL QSOs to be on average steeper than non-BAL QSOs, and allow us to firmly conclude (above 97% confidence) that BAL QSOs do not have flatter spectra than non-BAL QSOs. The QSO sample from our work includes three sources classified as variable: the unresolved non-BALs 0029−09, 1005+48 and 1521+43 and the resolved BAL QSO 1603+30. 0029−09 and 1521+43 are the flatter sources in the total QSO sample, both with $\alpha_{4.8}^{8.4} > 0.5$. The resolved BAL QSO 1603+30 has a spectral index near the limit between flat and steep spectra, with $\alpha_{4.8}^{8.4} = -0.45$. 1005+48 shows modest variability (just at the adopted thresholds of significance and fractional variability) and its spectral index is $\alpha_{4.8}^{8.4} = -0.67$. This trend between variability and a flat radio spectra is consistent with the expectation that a flat spectrum source is more likely to present Doppler beaming, and therefore have any existant variability magnified due to this same effect.

The radio luminosities of the sources, $L_{\ 4.8\mathrm{GHz}}$ in the QSO rest frame, are listed in the penultimate column of Table 3.7. They were calculated using the total flux density at 4.86 GHz from the VLA or from Effelsberg if VLA data were not available from this work. The k-correction was obtained using the spectral index $\alpha_{4.8}^{8.4}$ listed in the same Table. The radio luminosities range from $10^{26.1}$ to $10^{28.6}$, above the limit $L_{\mathrm{rad}} = 10^{26}$ W Hz^{-1} generally adopted for radio-loud QSOs (Miller 1990).

Comparison with literature samples

It is interesting to test how the two spectral-index distributions obtained for the FIRST-SDSS QSOs in our work, and in the BAL QSO sample by Montenegro-Montes et al. (2008a), compare to other samples of radio QSOs from the literature. A useful survey to compare with is the B3-VLA QSO sample (Vigotti

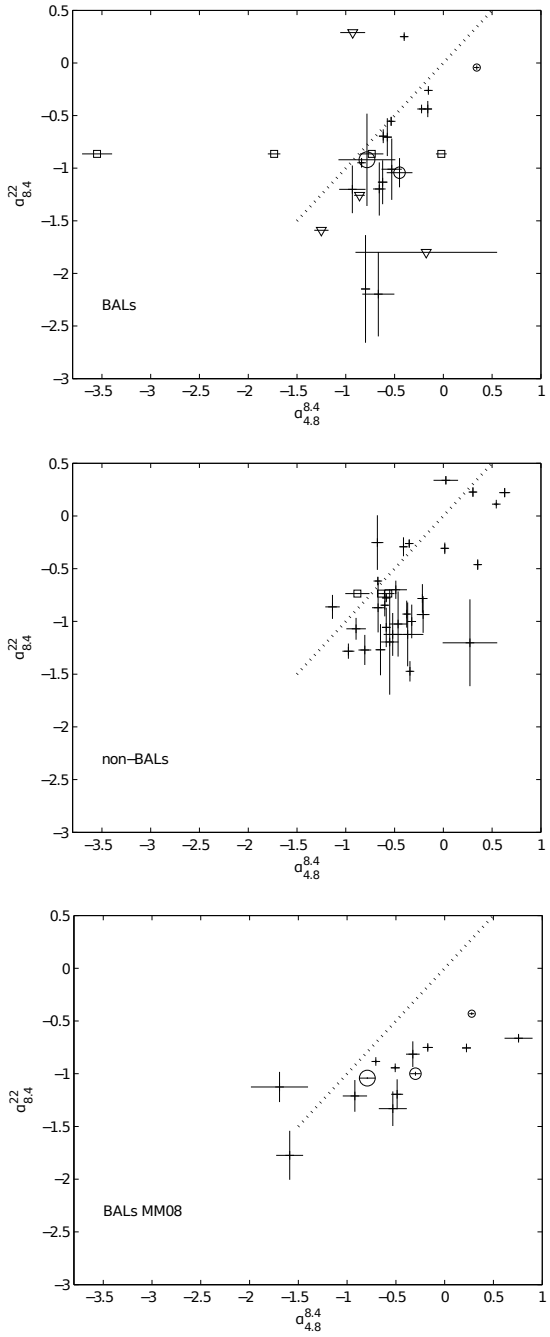

Figure 3.3: $\alpha^{22}_{8.4}$ versus $\alpha^{8.4}_{4.8}$ for the BAL QSOs, the non-BAL QSOs and Montenegro-Montes et al. (2008a) sample. The dashed line traces the locus of power-law spectra. Square symbols indicate sources lacking a 22-GHz flux density. For these, we adopted the $\alpha^{22}_{8.4}$ mean value of the sample. Upper limits for $\alpha^{22}_{8.4}$ are plot as triangles. Circles indicate objects in common with Montenegro-Montes et al. (2008a) (symbol size increases with the RA of the source).

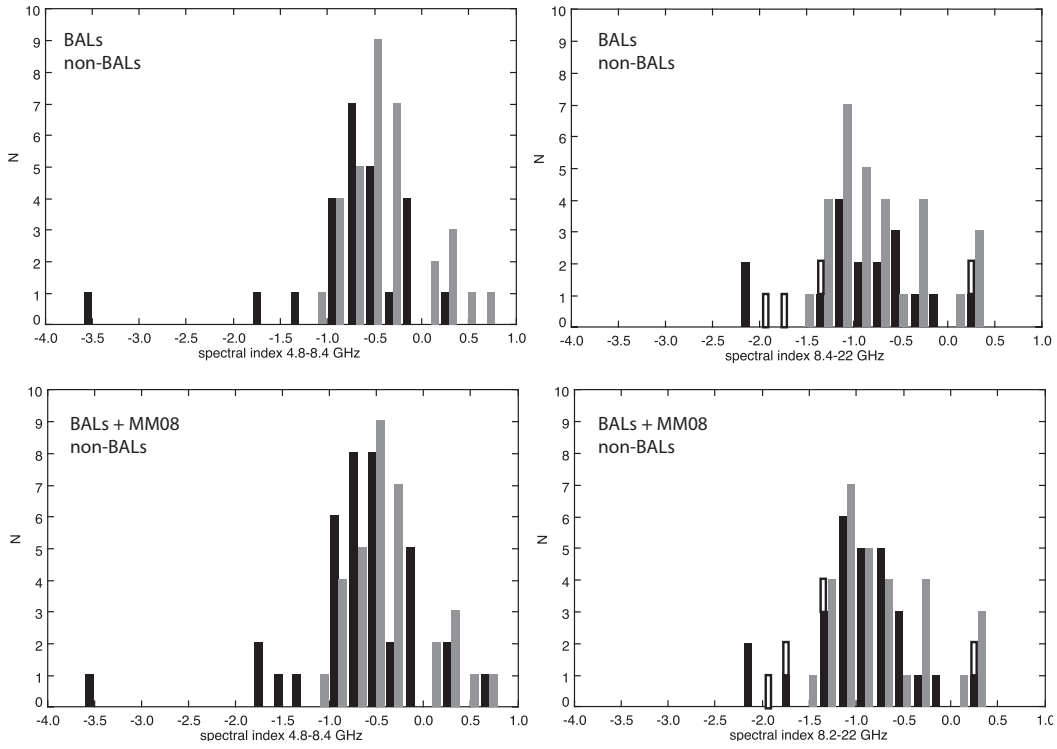

Figure 3.4: Distribution of the radio spectral indices ($\alpha_{4.8}^{8.4}$ and $\alpha_{8.4}^{22}$) for the BAL (black) and non-BAL (grey) QSO samples in this work. Upper limits are in white.

et al. 1997, 1999), selected at 408 MHz, and complete down to $S = 100$ mJy, with available multifrequency data from which we can compute the spectral index in the range 4.8-10.6 GHz, close to the range 4.8-8.4 GHz analysed in the present work. The angular sizes at 1.4 GHz of the B3-VLA QSOs were measured from maps taken with the VLA in C and D configurations (Vigotti et al. 1989) and for the most compact sources from observations in A configuration (private communication). Since most of the QSOs in our sample are unresolved, apart from analysing the spectral index distribution for the B3-VLA QSO sample as a whole (the largest size for these sources is 131 arcsec), we also considered the subsample with angular sizes below 2.3 arcsec, which is a representative upper limit of the sizes of the unresolved sources in our work (from 8.46 GHz VLA data). The basic statistics for the spectral indices $\alpha_{4.8}^{10.6}$ of the B3-VLA QSOs are included in Table 3.8, considering the whole sample and the subsample of the more compact sources, with sizes below 2.3 arcsec. A K-S test shows that compact B3-VLA QSOs have a similar distribution of spectral indices as BAL QSOs, at 97% confidence level, both for the sample of this work and for the combined sample including Montenegro-Montes et al. (2008a) BALs. The comparison with non-BALs shows that B3-VLA QSOs are steeper, at a 99.1% confidence level. There is no obvious physical reason for B3-VLA QSOs to be more similar to BAL QSOs than to non-BAL QSOs, the most plausible explanation being that the selection of B3-VLA QSOs at a low frequency, 408 MHz, favours the inclusion of steeper sources. The fact that the spectral indices of B3-VLA QSOs are more similar to those of BAL QSOs than to those of non-BAL QSOs is a consequence of the former being slightly more steep than the latter. Furthermore, this result emphasizes the importance of using an appropriate control sample.

3.2.5 Polarisation

For all sources we have obtained Stokes Q and U (S_Q and S_U) in order to calculate the fractional polarisation m and the polarisation angle χ. Most of the measurements were obtained from the VLA observations. In only a few cases did the Effelsberg observations have high-enough signal-to-noise to detect polarisation fractions below 10%. Only 3-σ results were considered, except for the cases for which a detection above 2-σ resulted in a consistent m with respect to the other frequencies, increasing the measurement reliability. Values of the fractional polarisation are presented in Tables 3.9 and 3.10 for BAL and non-BAL QSOs respectively. We have included the NVSS values (NRAO VLA Sky Survey, Condon et al. 1998) for the polarisation fraction at 1.4 GHz when no measurements could be obtained from our data. The polarisation measurements as well as the more significant upper limits were mostly obtained for frequencies in the range from 1.4 to 8.5 GHz.

We have obtained the cumulative distribution function $F(m) = \mathrm{Prob}(M \leq m)$ for the fractional polarisation at 1.4, 4.8 and 8.4 GHz for the two samples, using the Kaplan-Meier estimator, that allows to include the information from

Table 3.9: Fractional polarisation m (in percentage), at several frequencies (ν in GHz), for the BAL QSO sample. When no polarisation measurement was possible at 1.4 GHz, the NVSS value was used (indicated with an asterisk). Last two columns show the Rotation Measure (observed and corrected values).

Name	$m_{1.4}$	$m_{2.6}$	$m_{4.85}$	$m_{4.86}$	$m_{8.3}$	$m_{8.46}$	$m_{10.5}$	m_{22}	m_{43}	Observed RM (rad m^{-2})	Rest-frame RM (rad m^{-2})
0044+00	1.2±0.9*	-	-	<3.8	-	<4.7	-	<74.3	-	-	-
0756+37	2.4±0.7	1.8±0.5	-	1.1±0.2	1.5±0.4	1.4±0.3	-	<10.1	-	60.4±2.1	643±26
0816+48	5.7±1.2	-	-	<4.3	-	<7.0	-	-	-	-	-
0842+06	<20.5	-	-	<3.8	-	<6.2	-	-	-	-	-
0849+27	<2.1*	-	-	-	-	-	-	-	-	-	-
0905+02	7.7±3.8	-	-	<4.7	-	4.2±1.8	-	<61.7	-	-	-
0929+37	6.1±0.9	-	-	<3.9	-	<4.1	-	<25.5	-	-	-
1014+05	<4.7	-	-	2.9±1.1	-	<4.9	-	<49.5	-	-	-
1040+05	<3.2*	-	-	4.4±0.9	-	<24.6	-	-	-	-	-
1054+51	4.2±1.1	-	-	-	-	<11.8	-	-	-	-	-
1102+11	1.9±0.9	-	-	<3.7	-	<6.2	-	<377.8	-	-	-
1103+11	<1.2	-	-	<1.5	-	<1.8	-	<13.1	-	-	-
1129+44	<7.5	-	-	<4.1	-	<4.7	-	-	-	-	-
1159+01	6.5±0.7	-	-	1.9±0.3	-	0.7±0.2	-	<4.9	-	−79.2±1.8	−822±16
1159+06	1.3±0.5	-	-	2.1±0.7	-	3.6±1.3	-	-	-	151.1±2.1	1436±21
1229+09	3.1±1.4	-	-	-	-	-	-	-	-	-	-
1237+47	<3.7	-	-	<3.8	-	5.9±2.6	-	-	-	-	-
1304+13	<5.5	-	-	<5.9	-	-	-	<77.7	-	-	-
1327+03	<2.1	<83.2	-	-	-	<2.3	-	-	-	-	-
1335+02	<2.5	-	-	<3.7	-	<1.9	-	<4.2	-	-	-
1337−02	7.8±2.4	-	-	-	-	<8.0	-	-	-	-	-
1404+07	<1.6	-	-	<5.3	-	0.6±0.2	-	<3.9	-	-	-
1406+34	2.9±0.9	-	<4.3	1.0±0.2	1.7±0.2	3.5±0.2	-	2.3±1.1	-	284.0±4.5	3520±57
1603+30	<2.4*	-	-	<14.6	-	<4.1	-	<52.4	-	-	-
1624+37	-	-	-	-	-	<17.9	-	-	-	-	−18350±570[1]

[1] RM value taken from Benn et al. (2005).

Table 3.10: Polarisation measurements for the sample of non-BAL QSOs (see caption of Table 3.9 for details).

Name	$m_{1.4}$	$m_{2.6}$	$m_{4.85}$	$m_{4.86}$	$m_{8.3}$	$m_{8.46}$	$m_{10.5}$	m_{22}	m_{43}	Observed RM [rad m^{-2}]	Rest-frame RM [rad m^{-2}]
0014+01	7.8±2.4	-	-	9.5±3.1	-	11.8±3.7	-	-	-	−7.8±0.6	8.7±6.1
0029−09	<6.9	-	-	<3.5	-	1.6±0.7	-	<8.4	<14.4	-	-
0033−00	3.8±0.9	-	-	<6.8	-	<9.1	-	-	-	-	-
0103−11	<2.3	-	-	<2.9	-	<2.7	-	-	<47.6	-	-
0124+00	<1.2	11.1±2.1	5.7 ±1.1	5.5±0.6	-	4.5±1.1	-	<38.1	-	43.7±7.9	257±64
0125−00	1.2±0.1*	-	4.5 ±0.9	6.4±0.3	-	6.9±0.3	5.6±1.0	4.8±1.8	<14.2	108.2±4.2	1041±45
0125−00A[1]	-	-	-	-	-	11.0±0.8	-	-	-	-	-
0125−00C[1]	-	-	-	-	-	6.3±0.2	-	-	-	-	-
0152+01	<3.8*	-	-	24.6±5.8	-	<14.9	-	-	-	-	-
0154−00	<1.1	-	-	1.2±0.3	-	-	-	<16.6	-	-	-
0158−00	3.5±0.4	-	-	1.9±0.5	-	<2.4	-	<18.4	-	-	-
0750+36	<11.9	-	-	1.4±0.7	-	<2.6	-	<26.5	-	-	-
1005+48	9.1±1.9	11.9±0.8	<95.1	11.3±0.4	11.4±0.9	12.4±0.8	12.1±3.0	15.4±3.4	<56.8	5.1±0.7	−26.9±8.0
1322+50	2.1±0.3	-	-	<2.6	-	<3.5	-	<33.1	-	-	-
1333+47	2.3±0.6	-	-	<5.2	-	-	-	<59.6	-	-	-
1401+52	7.0±1.5	-	-	<3.5	-	4.8±1.6	-	<59.3	-	-	-
1411+34	5.0±0.3*	5.6±1.1	-	5.9±0.7	-	4.8±0.6	-	<3.0	<1.0	−238±16	−1937±130
1411+43	2.2±0.6	-	-	1.2±0.3	-	2.2±0.5	-	<8.0	<29.8	−174.4±7.4	−3077±130
1502+55	4.0±0.9	-	-	5.6±1.2	-	6.3±1.9	-	<69.6	-	96.6±0.6	1668±11
1512+35	<2.2*	-	-	1.8±0.9	-	2.4±0.9	-	<10.9	-	-	-
1521+43	1.6±0.3	-	-	0.7±0.2	-	2.6±0.1	-	1.2±0.5	-	−72.1±5.3	−725±53
1528+53	<2.4	-	-	-	-	4.5±1.1	-	<27.4	-	-	-
1554+30	1.9±1.1*	-	-	-	-	<17.8	-	<87.6	-	-	-
1634+32	<7.3	-	1.5±0.4	1.7±0.2	-	2.8±0.3	-	<18.4	<38.7	281±40	2950±450
1636+35	-	-	-	2.8±0.5	5.9±1.0	-	-	<18.6	-	-	-
1641+33	2.1±1.0	-	-	2.1±0.5	-	3.1±0.7	-	<28.0	-	23.2±0.1	107.1±1.4
1728+56	2.3±0.6	-	-	3.2±0.6	-	<3.7	-	<50.8	-	-	-
2109−07	3.6±1.4	-	-	4.2±1.3	-	<7.2	-	-	-	-	-
2129+00	<4.3	-	-	<3.0	-	<5.4	-	-	-	-	-
2143+00	-	-	-	<2.3	-	<2.2	-	<15.7	<20.2	-	-
2238+00	<7.6	-	-	-	-	-	-	-	-	-	-
2244+00	<8.0	-	-	<4.2	-	<6.2	-	<52.6	-	-	-
2248−09	3.3±1.4*	-	-	<7.7	-	<14.4	-	-	-	-	-
2331+01	<3.7*	-	-	<4.5	-	<5.5	-	<37.6	-	-	-
2346+00	6.8±1.8	-	-	<5.1	-	1.8±0.8	-	<12.4	<39.7	-	-
2353−00	<3.3	-	-	<4.3	-	<6.6	-	-	-	-	-

[1] Measurements for a specific component (see Fig. 2).

the upper-limits. The method is described in detail in Feigelson & Nelson (1985). The results are shown in Fig. 3.5. The pair of numbers in parenthesis indicates the number of detections and the number of upper limits for each frequency.

The distributions for the non-BAL QSOs are very similar for the three frequencies, yielding a median value m in the range 1.8-2.5%. The 85% percentile corresponds to $m \leq 5.8-6.3\%$. Table 3.10 shows five sources exceeding $m = 10\%$ at some frequency. These sources are 0014+01, 0124+00, 0152+01, 1005+48 and the lobe component of 0125−00. In particular 1005+48 shows fractional polarisation above 10% at a wide range of frequencies, from 2.6 to 22 GHz. The distributions for the BAL QSOs have a higher uncertainty, due to the fewer data and the larger fraction of upper limits, especially at 4.8 and 8.4 GHz. From the 1.4 GHz data we find a median $m = 1.8\%$ and a limit $m \leq 6.2\%$ for the 85% percentile. None of the measurements in Table 3.9 is above $m = 10\%$.

Regarding the three BAL QSOs in common with Montenegro-Montes et al. (2008a), we note that for 1603+30 these authors obtained $m = 1\%$ at 8.4 GHz and upper limits for the remaining frequencies in their study. For this source we only obtained upper limits, and the one at 8.4 GHz is consistent with the measurement at Montenegro-Montes et al. (2008a). For 1159+01 our measurements at 4.8 and 8.4 GHz agree with the results by Montenegro-Montes et al. (2008a), although at 1.4 GHz we obtained $m = 6\%$, less than half the value reported by Montenegro-Montes et al. (2008a), of $m = 15\%$ (taken from NVSS). For the remaining source, 1624+37, our data only provide a high upper limit for m, but the source shows a high fractional polarisation from the data reported in Benn et al. (2005) (their Table 2), with $m = 6\%$ at 4.8 GHz and $m = 11\%$ at 10 and 22 GHz.

The fractional polarisations of BAL and non-BAL QSOs appear to be quite similar, with median values around 1-3%, an 85% of the sources having $m <$ 6%, and around ten per cent of the sources showing fractional polarisation above 10% at some frequency (4/34 for the non-BAL QSOs and 2/25 for the BAL QSOs, considering the information from the literature).

Comparison with literature

An extensive survey of the fractional polarisation of QSOs is presented in Pollack (2003), based on a sample with $S_{4.85\ \mathrm{GHz}} \geq 350$ mJy and radio spectral index $\alpha_{1.4}^{4.8} \geq -0.5$. The authors compute m at 4.85 GHz separately for the core and jet components, and find a higher polarisation for the jet components. In particular, the 85% percentile corresponds to $m \leq 3\%$ for the core components and to $m \leq 14\%$ for the jet components, and the proportion of sources exceeding a fractional polarisation of 10% is 1/91 for the cores and 17/43 for the jet components. The fractional polarisations we found for the BAL and non-BAL QSOs in our sample occupy an intermediate range between the results found by Pollack et al. (2003) for core and jet components.

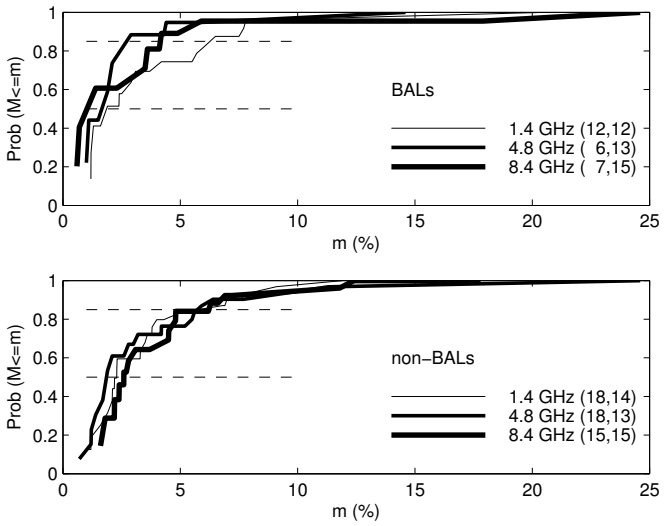

Figure 3.5: Cumulative distribution of the fractional polarisation for the two samples, at each of three frequencies. Each pair of numbers in parenthesis indicates the number of detections and the number of upper limits at that frequency. The dashed lines show the 50% percentile (i.e. the median) and the 85% percentile.

Sadler (2006) obtained the polarisation fraction or upper limits for 41 QSOs in their sample of radio sources selected at 20 GHz, with $S_{20\ \mathrm{GHz}} \geq 100$ mJy. As mentioned in Sect. 4.2, this QSO subsample is dominated by flat spectrum sources (69% with $\alpha_5^8 \geq -0.5$, compared to 42% for the SDSS-FIRST QSOs in our sample). We obtained the cumulative distribution function of m for this sample, using the Kaplan-Meier estimator, and found $m = 2.4\%$ and $m \leq 4.2\%$ for the median and the 85% percentile respectively. None of the QSOs in Sadler (2006) sample exceed polarisation levels of 10%. The results of Sadler et al. (2006) show a good agreement with those of Pollack et al. (2003) for the core components.

3.2.6 Rotation measures

With at least three measurements of the polarisation angle χ at different frequencies it is possible to estimate the Rotation Measure (RM) of a source performing the linear fit of the polarisation angle versus the square of the observed wavelength λ ($\chi = \chi_0 + \mathrm{RM}\lambda^2$, χ_0 being the intrinsic polarisation angle). The Rotation Measure, which is the slope of the fit, is proportional to the magnetic field component along the line of sight, to the electron density, and to the path length,

$$\mathrm{RM} \propto \int_0^L n_e \; B_{\parallel} \; dl \tag{3.5}$$

Plots of the linear fits for the four BAL QSOs and ten non-BAL QSOs with at least three measurements are shown in Figure 7. The observed RM values are listed in Tables 3.9 and 3.10, along with the RM values corrected from the Galaxy contribution and converted to the rest-frame, multiplying by the factor $(1+z)^2$. Since the sources are located well above the Galactic Plane ($b > 28°$) the applied Galactic correction was small, in the range from -9 to 17 rad m^{-2} (Taylor et al. 2009).

Results can be summarized as follows:

- There is a good agreement between the observed Rotation Measure for 1159+01 in this work, of 79.2±1.8 rad m^{-2} and the result from Montenegro-Montes et al. (2008a), of 72.1±1.4 rad m^{-2}. The RM listed in Table 3.9 for 1624+37 was taken from Benn et al. (2005). With a rest-frame RM of -18350 ± 570 rad m^{-2}, this was and still is the second-highest RM known, after that of quasar OQ172 (Kato et al. 1987; O'Dea 1998), with RM = 22400 rad m^{-2}.

- For the non-BAL QSO sample we have available data for ten sources, allowing to obtain some statistical results. We found rest-frame |RM| values in the range from 8.7 to 3077 rad m^{-2}, with a median value of 883 rad m^{-2}, and average and standard deviation of 1180 rad m^{-2} and 1117 rad m^{-2}. Three of the BAL QSOs have rest-frame |RM| values within the range found for the non-BAL QSOs. One of the remaining BAL QSOs with available Rotation Measure is 1406+34, with RM = 3520 ± 57 rad m^{-2}, which is only 2σ from the average value for the non-BAL QSOs. The other source is 1624+37, with the extremely high value RM = -18350 ± 570. The small number of data for BAL QSOs does not allow to compare the Rotation Measures of the two samples.

- Zavala & Taylor (2004) reported rest-frame Rotation Measures, |RM|, for the flat core components of 26 QSOs in the range from 200 to 10000 rad m^{-2}, with a median value of 1862 rad m^{-2} and average 2515 rad m^{-2}. The same authors found lower values for the Rotation Measures of the steep jet components of these QSOs, for which they obtained a median value of 458 rad m^{-2} and average 600 rad m^{-2}. The statistics for the non-BAL QSOs in our sample places them in the intermediate range of Rotation Measures between those of the flat and steep components in the Zavala & Taylor sample.

3.3 Conclusions

We constructed a sample of 59 radio-loud QSOs with $S_{1.4} > 30$ mJy, selected by cross-correlating the FIRST radio survey and the 4th edition of the SDSS Quasar Catalogue, at redshifts such that the wavelength range from Si IV1400 Å to C IV1550 Å is covered by the SDSS spectra. The sample comprises 25

sources having definite broad absorption in C IVwith velocity width of at least 1000 km s^{-1}, referred to as the "BAL QSO sample", and 34 sources lacking such absorption, which form the "non-BAL QSO comparison sample". The sources were observed at frequencies ranging from 1.4 to 43 GHz, using the 100-m Effelsberg telescope and at the VLA, and these have allowed us to compare several radio properties of the two samples, including morphology, flux-density variability, spectral shapes, spectral-index distributions, and polarisation properties:

Linear sizes

Only eight of the 59 sources are extended at the arcsec level, four of them being BAL QSOs and four of them non-BAL QSOs. The fractions of resolved sources are similar for BALs (16%) and non-BALs (12%), and the distributions of linear sizes are also similar, ranging 20 to 200-400 kpc. The morphologies are also similar, including elongated sources (1), core-lobe (4, possibly 5) and core double-lobe (2, possibly 3). 90-95% of the unresolved sources have an estimated size at 8.46 GHz below 20 kpc, obtained from VLA observations at this frequency (2.3 arcsec resolution), and adopting the average redshift $z = 2.4$ for the two samples. Two of the unresolved BAL QSOs, 1159+01 and 1624+37, were resolved from VLBA observations in Montenegro-Montes et al. (2008b, 2012 in preparation), both showing a core-jet morphology with sizes of 0.85 kpc and 60 pc respectively.

Flux-density variability

The flux-density variability of the sources at 4.8 and 8.4 GHz was computed from observations at VLA and Effelsberg, at the same frequency, in two epochs separated typically by 1.6 years. In addition, for the 3 BAL QSOs in common with Montenegro-Montes et al. (2008a), the flux densities from our work at various frequencies in the interval 2.6-22 GHz (VLA or Effelsberg) were compared to similar data (frequency and telescope) from Montenegro-Montes et al. (2008a), with a time difference of 3-4 years. Excluding variations that could be attributed to resolution effects (higher flux at the lower angular resolution for any source, whether resolved or not), we found three likely variables from our data, all non BALs (0029-09, 1005+48, 1521+43). Using flux densities from the literature, we concluded that the BAL QSO in our sample 1603+30 was also a candidate variable. Our data suggest a lower rate of variable sources among BALs, compared to non-BALs. However, this needs to be confirmed by a monitoring of the sample at various epochs using the same configuration for the radio observations.

The proportion of variable sources exceeding a fractional variability of 20% in our total sample, 4/59, is consistent with the fraction for the core-dominated QSO sample of Barvainis et al. (2005), selected at 8 GHz and yielding a fraction of 5/50 variables at this frequency. The proportion is also consistent with

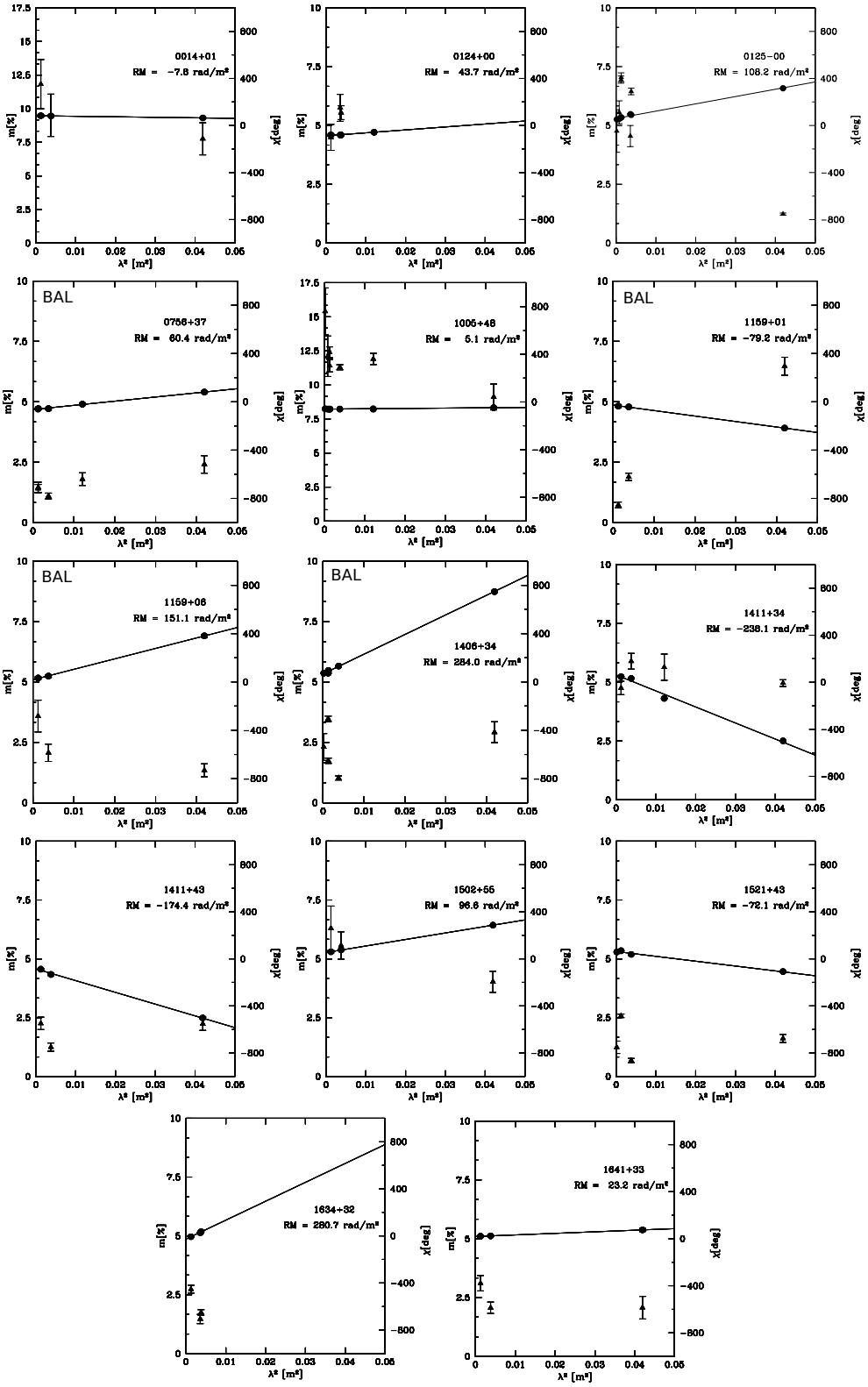

Figure 3.6: Linear fits of the polarisation angles χ versus the square of the observed wavelengths for 4 BAL QSOs and 10 non-BAL QSOs, yielding the Rotation Measures. The errors in the position angles are lower than the dot size. Triangles correspond to the polarisation percentages (m).

the fraction 2/32 from the QSO sample studied at 20 GHz by Sadler et al. (2006).

Radio spectral shape

We found 9 BAL QSOs and 8 non-BAL QSOs with GPS-like radio spectra, having peak frequencies in the range from 0.5 to 7 GHz in the observer frame. Their linear sizes (or limits thereon, typically 20 kpc at 8 GHz) are consistent with a maximum allowed size of 1 kpc, for classification as a GPS source. Higher-resolution observations are needed to confirm or reject the GPS classification of these sources. In particular, this classification is confirmed for 1624+37, with a size of 60 pc at 5 GHz and 75 pc at 8 GHz (Montenegro-Montes et al. 2008b, 2012 in preparation).

The fractions of candidate GPS sources are $36 \pm 12\%$ (9/25) for BAL QSOs and $23 \pm 8\%$ (8/34) for non-BAL QSOs, i.e. no significant difference. Given the widespread interpretation that GPS are young sources, our result suggests that BAL QSOs are not a younger population than non-BAL QSOs.

Low-frequency upturns in some of the radio spectra indicate additional low frequency components, in about $12 \pm 7\%$ of the BAL QSOs (3/25) and $15 \pm 7\%$ of the non-BAL QSOs (5/34). The two values are similar within the errors, and since the low frequency excess emission likely corresponds to old components, this result again favours similar distributions of ages for BAL and non-BAL QSOs.

Radio spectral indices

We found a mix of flat ($\alpha \geq -0.5$) and steep ($\alpha < -0.5$) spectra for both the BAL and the non-BAL QSO samples, suggesting that both classes are seen from a wide range of orientations with respect to the jet axis. A similar conclusion was reached by Becker et al. (2000) and Montenegro-Montes et al. (2008a), on the basis of the radio spectral-index distribution of BAL QSOs. Kolmogorov-Smirnov tests comparing the spectral index distribution $\alpha_{4.8}^{8.4}$ of the two samples provide weak evidence (at the 91% confidence level) that the spectra in the combined BAL QSO sample from our work and Montenegro-Montes et al. (2008a) are steeper than those in the non-BAL QSO sample, and significant evidence ($\geq 97\%$ confidence) that both our BAL sample and the combined BAL QSO sample are not flatter than the non-BAL QSO sample. The latter result indicates that radio-loud BAL QSOs do not tend to have position angles closer to the radio axis than non-BAL radio-loud QSOs, i.e. a model in which the BAL absorption arises predominantly from polar winds (for instance Punsly 1999a, 1999b), is not consistent with our results.

Radio polarisation properties

The fractional polarisations m of the BAL and non-BAL QSOs are similar, median 1-3%, with $\sim 85\%$ of the sources having $m < 6\%$, and $\sim 10\%$ having $m > 10\%$ at some frequency. These values are intermediate between the values found by Pollack et al. (2003) for the core and jet components of the QSOs in their sample, with higher values for the latter.

The Rotation Measure has been determined for 5 BAL QSOs and 10 non-BAL QSOs. The Rotation Measures for the non-BALs range 9 to 3100 rad m^{-2}, with mean and standard deviation 1180 ± 1120 rad m^{-2}, intermediate between flat- and steep-spectrum (higher RM) components in the sample of QSOs of Zavala & Taylor (2004). The limited statistics provide no evidence for a significant difference between the RM of BAL and non-BAL QSOs. The only BAL QSO exceeding by more than 2σ the mean value found for non-BAL QSOs is 1624+37, with an unusually high RM $= 18350 \pm 570$ rad m^{-2}.

Chapter 4

Multi-frequency study of radio variability

4.1 Introduction

Radio-variability in BAL QSOs may provide further constrains to the orientation of these objects. Marscher & Gear (1985) suggest that shocks propagating along radio jets can induce radio flux density variability. The amplitude of the variability can be greatly amplified by the relativistic beaming effect if the radio jets are closely aligned with the line of sight. Similarly, Snellen et al. (1998) present a qualitative model of the long time-scale flux density variability due to the deceleration of a relativistic radio component ejected from the nucleus of active galactic nuclei, and show the comparison with the shock model. These authors also discuss how the amplitude of the variability can be greatly amplified by relativistic beaming if the component is ejected at a small angle to the line of sight, an effect that would also apply in the shock model when the radio jet is oriented towards the observer.

Zhou et al. (2006) compared the 1.4-GHz flux densities of all QSOs in the SDSS QSO catalogues Schneider et al. (2005, 2007) with detections in both the FIRST and NVSS surveys. Among the selected 151 radio-variable QSOs, they identify six to eight QSOs that present the BAL phenomenon. This subsample shows radio flux density variations from 16% to 55% within 1.5-5 yr. Such large amplitudes of variations imply brightness temperatures much higher than the inverse Compton limits, suggesting the presence of relativistic jets beaming toward the observer. Ghosh & Punsly (2007) expand the Zhou et al. (2006) sample of radio variable potentially polar BAL QSOs to the entire SDSS DR5 (Sloan Digital Sky Survey data release 5). The expanded sample of BAL QSOs with high brightness temperatures results in a set composed of 12 sources and shows a large fraction (17%) of LoBAL QSOs whereas the HiBAL QSOs are only 6%, apparently confirming the model of Punsly (1999b).

Although the study of the flux density variability may be used to constrain the orientation of a radio source, this method has been underutilized in the case of BAL QSOs. For a long time, BAL QSOs were in fact believed to be

extremely rare among the population of radio QSOs Stocke et al. (1992) and few measurements of radio flux densities have been performed for these objects until the advent of large comprehensive radio surveys, like the FIRST, which showed that approximately 15% of the BAL QSOs are radio-loud.

In this chapter we continue the multi-frequency study of long-term radio variability of a complete sample of 15 BAL QSOs with redshifts 0.6 <z< 3.4 and flux densities > 15 mJy at 1.4 GHz (as reported in the FIRST catalog) started by Montenegro-Montes et al. (2008a). Thus the sample studied in this chapter is distinct from the one presented in chapter 2, and will be named RBQ sample hereafter.

According to the Structure Function analysis made by Hovatta et al. (2007), from a sample of 70 QSOs the (redshift-corrected) median time-scale for QSO variability is about 1 yr, and only 0.7 yr for High Polarization Quasars (HPQs). At a redshift ∼2 this translates into observed time scales of 2-3 yr. We looked for evidence of long-term flux density variability at different frequencies comparing various observations of the RBQ sample repeatedly performed during 4 years with the Effelsberg 100-m radio telescope and the VLA interferometer. When available, data from literature were also compared with collected values. A second sample of non-BAL QSOs with similar flux densities and redshift contribution as the RBQ sample was also studied in order to compare variabilities eventually observed in BAL QSOs with those characterizing non-BAL objects.

4.2 The sample and observations

The sample consists of the 15 radio-loud BAL QSOs (RBQ sample) selected by Montenegro-Montes et al. (2008a). It is a complete sample in a sense that it is composed of all the BAL QSOs that were known to be radio loud at that time (Becker et al. 2000, 2001; Menou et al. 2001; Reichard et al. 2003) and which were characterized by flux densities > 15 mJy at 1.4 GHz according to the FIRST catalogue (White et al. 1997). These selection criteria were adopted in order to facilitate total power detections at high frequencies. The RBQ sample is shown in Table 4.1. A second sample (Table 4.2) of non-BAL QSOs was studied in order to compare variabilities eventually observed in BAL QSOs with those characterizing non-BAL objects. The comparison sample was extracted from the complete B3-VLA QSO catalogue Vigotti et al. (1997), by selecting a set of sources with redshift and flux densities at 1.4 GHz comparable to those characterizing the RBQ sample.

Radio-continuum flux density measurements of the RBQ sample were performed at different frequencies with the Effelsberg 100-m radio telescope and with the VLA over a time window of 4 years. A summary of the observational sessions carried out during this time is given in Table 4.3. Flux densities of the RBQ sample collected from the literature were also included, enabling, in a few cases, a flux density monitoring with the largest temporal baselines of

Table 4.1: RBQ sample characteristics. Col. 1: source ID; Col. 2,3: optical coordinates in J2000.0; Col. 4: angular distance between optical and FIRST radio positions; Col. 5: optical spectroscopic redshift; Col. 6: integrated radio flux density at 1.4 GHz according to the FIRST catalogue; Col. 7: APS E magnitude corrected on Galactic extinction; Col. 8: Balnicity Index (BI) as defined in Weymann et al. (1991); Col. 9: BAL classification as given in literature; Col. 10: reference for classification defined in Col. 9.

ID	RA (hh:mm:ss.s)	DEC (dd:mm:ss.s)	r_ρ (arcsec)	z	$S_{1.4}$ (mJy)	E	BI (km/s)	Type	Reference
0039−00	00:39:23.2	−00:14:52.6	0.22	2.233	21.20	19.50	0	HiBAL	1
0135−02	01:35:15.2	−02:13:49.0	0.31	1.820	22.40	16.79	400	HiBAL	3
0256−01	02:56:25.6	−01:19:12.1	0.66	2.491	27.60	18.57	4100	HiBAL	3
0728+40	07:28:31.6	+40:26:16.0	0.33	0.656	16.80	15.27	0	LoBAL	2
0837+36	08:37:49.6	+36:41:45.4	0.20	3.416	27.10	19.16	1200	LoBAL	6
0957+23	09:57:07.4	+23:56:25.2	0.12	1.995	140.50	17.64	3500	HiBAL	2
1053−00	10:53:52.9	−00:58:52.7	0.14	1.550	24.66	18.03	300	LoBAL	4
1159+01	11:59:44.8	+01:12:06.9	0.07	1.989	268.48	17.30	1300	HiBAL	1
1213+01	12:13:23.9	+01:04:14.7	0.13	2.836	22.93	19.69	0	HiBAL	1
1228−01	12:28:48.2	−01:04:14.5	0.27	2.653	30.81	17.74	1500	HiBAL	4
1312+23	13:12:13.6	+23:19:58.6	0.10	1.508	44.10	17.13	6700	HiBAL	2
1413+42	14:13:34.4	+42:12:01.7	0.10	2.810	18.74	17.63	600	HiBAL	2
1603+30	16:03:54.1	+30:02:08.6	0.28	2.028	54.20	17.61	0	HiBAL	2
1624+37	16:24:53.5	+37:58:06.6	0.05	3.377	56.44	17.62	0	HiBAL	5
1625+48	16:25:59.9	+48:58:17.5	0.02	2.724	25.45	17.41	0	HiBAL	6

References: 1 - Menou et al. (2001); 2 - Becker et al. (2000); 3 - Becker et al. (2001); 4 - Reichard et al. (2003); 5 - Holt et al. (2004); 6 - Identified directly from SDSS-DR3 database.

Table 4.2: Comparison sample characteristics. Col. 1: source ID; Col. 2,3: optical coordinates in J2000.0; Col. 4: optical spectroscopic redshift; Col. 5: integrated radio flux density at 1.4 GHz according to the FIRST catalog.

ID	RA hh:mm:ss.s	DEC dd:mm:ss.s	z	$S_{1.4}$ (mJy)
1415+340	14:15:36.9	34:04:41.9	2.476	16.15
1501+340	15:01:49.4	34:08:31.7	3.362	18.91
1510+340	15:10:37.1	34:02:20.4	2.675	27.03
1644+340	16:44:17.3	34:22:54.4	2.859	23.80
2207+010	22:07:08.3	01:01:25.6	2.911	16.71
2217+003	22:17:59.4	00:30:54.7	3.099	20.90
2323+003	23:23:55.4	00:35:50.3	2.286	16.89

Table 4.3: Details of the observations collected for this work. In the last column: RBQ=RBQ sample, C=comparison sample.

Date (year)	Telescope (Config.)	Frequencies (GHz)	Samples observed
2005	Effelsberg	4.8, 8.4, 10.4	RBQ+C
2006	VLA(A)	8.4, 14, 22, 43	RBQ
2006	Effelsberg	2.6	RBQ+C
2008	VLA (CnB)	8.4, 22	RBQ
2009	VLA (B-CnB)	8.4, 22	RBQ
2009	Effelsberg	2.6, 4.8, 8.4, 10.4	RBQ+C

12 years. Five sources were in common with the list of Becker et al. (2000) who observed these objects at 1.4 and 8.4 GHz with the VLA in D and A configuration in November 1997 and January 1998, respectively. In one case (1624+37) data recorded in 2004 at different frequencies were available from Benn et al. (2005). The FIRST Survey provides 1.4-GHz flux densities for all sources observed with the VLA in B configuration. Supplementary data are given by the NVSS Survey Condon et al. (1998) which provides 1.4-GHz flux densities from the D-configuration VLA with a resolution of 45″. Our measurements at the VLA were performed with an integration time sufficient to reach high signal-to-noise ratio in order to guarantee high-quality measurements even in case of significantly smaller flux density due to variability. The flux density calibration was also performed by using 3C286 as primary calibrator (on the Baars et al. 1977 scale). Observations at Effelsberg were performed with standard cross scans of 40 s subscan duration. Although the set of radio observations spans a wide range of angular resolutions, the measured flux densities can be directly compared, since all sources present point-like structure at all resolutions. Details on the observation method as well as calibration and data reduction are described in Montenegro-Montes et al. (2008a). The flux densities of the RBQ sample measured at different epochs at 1.4, 2.6, 4.8, 8.4, 10.4 and 22 GHz are given in Tab. 4.7, 4.8, 4.9, 4.11, 4.10 and 4.12. When more than 2 data points were available (i.e. at 8.4 and 22 GHz) the source flux density as a function of time was also plotted (Fig. 4.1).

Data for the comparison sample were collected at 2.6, 4.8, 8.4 and 10.4 GHz during two observational sessions performed at Effelsberg in 2005-2006 and 2009 (see Table 4.3), whereas data at 1.4 GHz were derived from the FIRST and NVSS surveys. The comparison sample was originally composed of 12 sources, however technical problems occurred during the observation of 5 sources in 2009 caused the reduction of the sample to 7 objects. The flux densities of the comparison sample measured at the two epochs at each frequency are given in Tab. 4.13, 4.14, 4.15, 4.16 and 4.17.

4.3 Methods

Flux density variability of different classes of radio sources has been studied by several authors. In the literature, there is a large number of criteria used to study the source variability, depending on the class of sources of sources and on the available data to perform such an investigation. Jauncey et al. (2003), analyzing Gigahertz Peaked Spectrum (GPS) sources, mention a source to "exhibit strong variability" when it doubles its flux density within a year. Hovatta et al. (2007) studied the time scale variability of AGN at high radio frequencies. They found that smaller variations occur on short time scales of 1-2 years, but larger outbursts happen quite rarely, with an average of approximately one every six years.

In this work we used the fractional variability index Tornikoski et al. (1993);

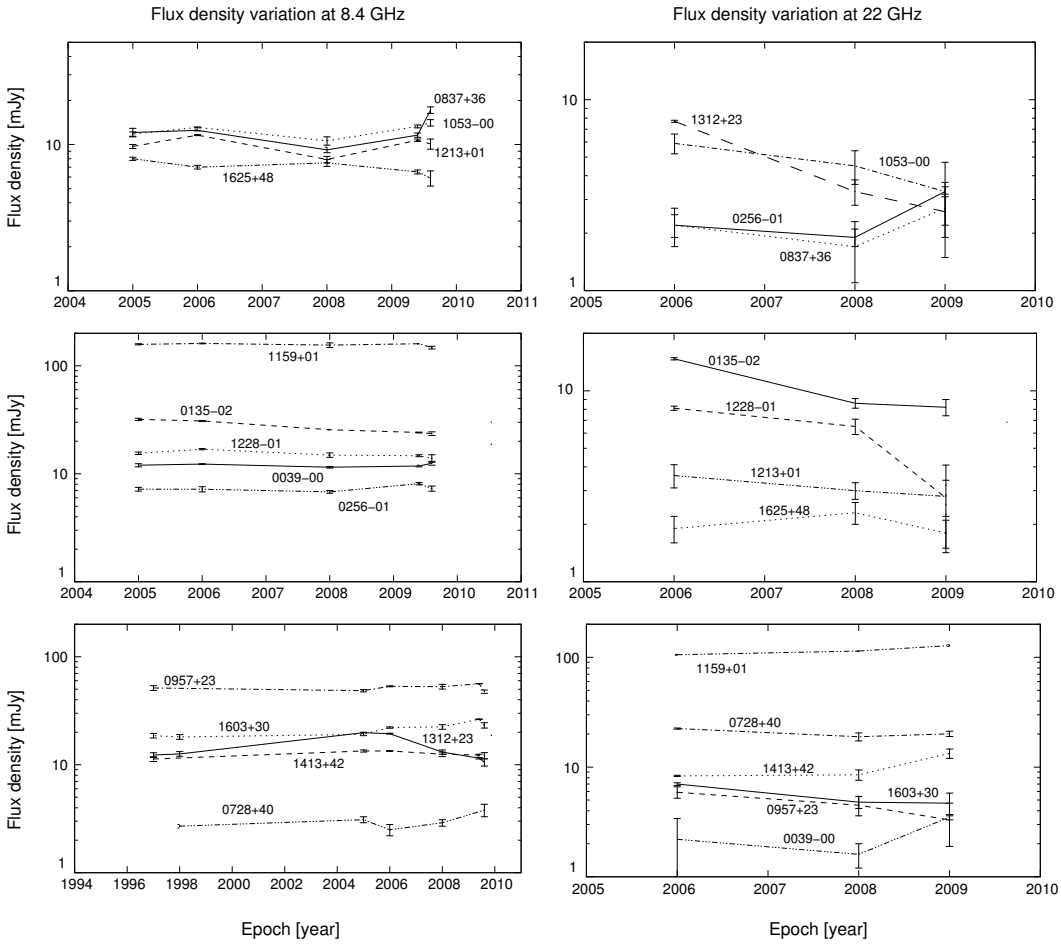

Figure 4.1: RBQ sample flux density variation in time at 8.4 and 22 GHz.

Tornianien et al. (2005) to calculate the flux density variation between two observations:

$$Var_{\Delta S} = \frac{S_{max} - S_{min}}{S_{min}} \tag{4.1}$$

where S_{max} and S_{min} are the maximum and minimum radio flux densities measured in a time interval at a given frequency. This value is the most suited for characterizing sources with few measurements or flaring behavior collected over long time periods, whereas other criteria, investigating for instance the standard deviation of the light curve Gaensler & Hunstead (2000), are more appropriate to detect stochastic variability in large data sets. An estimate of the statistical significance of the source variability was evaluated by calculating the σ_{Var} parameter, defined in Zhou et al. (2006):

$$\sigma_{Var} = \frac{|S_2 - S_1|}{\sqrt{\sigma_2^2 + \sigma_1^2}} \tag{4.2}$$

where S_1 and S_2 are the integrated radio flux densities at the first and second epoch, and σ_1, σ_2 are the corresponding uncertainties, respectively. Equivalent criteria were adopted by different authors. Zhou et al. (2006) utilize the variability ratio $V = S_{max}/S_{min}$ to build a sample of variable QSOs from FIRST and NVSS catalogs. Similarly, Bannister et al. (in preparation) verify the low frequency radio-variability of a sample of Galactic and extragalactic radio sources over a time period of 12 years by using the expression: $V = (S_{max} - S_{min})/(S_{max} + S_{min})$. In our work the fractional variability index and the corresponding significance were calculated for each pair of measurements at each frequency. Since we are interested in the maximum amount of variability that a source can have, only the highest values of $Var_{\Delta S}$ and the corresponding σ_{Var} were considered in the analysis.

4.4 Results

Table 4.4 summarizes the largest value of $Var_{\Delta S}$ and the corresponding σ_{Var} for the RBQ sample at frequencies 1.4, 2.6, 4.8, 8.4, 10.4 and 22 GHz. For some sources we could not determine the radio variability at each frequency because either data were not available in the literature or measurements failed to provide a good estimate of the flux density. Similar values were calculated for the comparison sample at frequencies 1.4, 2.6, 4.8, 8.4 and 10.4 GHz (Table 4.5). According to Table 4.4, if we consider as variability borderline values those adopted by Tornianien et al. (2005) $Var_{\Delta S} > 3$ and $\sigma_{Var} > 3$, no source of the RBQ sample results to be variable at any frequency over at least four years. Similarly, none of the remaining 7 sources of the comparison sample exhibits variability indices greater than 3 with a significance above 3.

The variability condition $Var_{\Delta S} > 3$ implies that the observed flux densities have at least to quadruplicate over the time range between two observations. The fact that both RBQ and comparison sample do not show any variability,

Table 4.4: Maximum fractional variability index and the corresponding significance for the RBQ sample. Superscripts indicate observational frequencies in GHz. (n.a.= not available).

ID	$Var_{\Delta S}^{1.4}$	$\sigma_{Var}^{1.4}$	$Var_{\Delta S}^{2.6}$	$\sigma_{Var}^{2.6}$	$Var_{\Delta S}^{4.8}$	$\sigma_{Var}^{4.8}$	$Var_{\Delta S}^{8.4}$	$\sigma_{Var}^{8.4}$	$Var_{\Delta S}^{10.5}$	$\sigma_{Var}^{10.5}$	$Var_{\Delta S}^{22}$	σ_{Var}^{22}
0039−00	0.09	1.34	n.a.	n.a.	0.05	0.59	0.09	1.88	0.16	1.89	1.19	4.25
0135−02	0.02	0.25	n.a.	n.a.	0.11	1.52	0.36	6.87	0.69	5.66	0.79	7.88
0256−01	0.24	6.51	n.a.	n.a.	0.11	1.36	0.19	4.53	0.40	2.98	0.74	4.95
0728+40	0.02	0.65	n.a.	n.a.	0.25	1.55	0.52	2.35	0.16	0.25	1.00	2.83
0837+36	n.a.	n.a.	0.17	2.65	0.20	1.86	0.87	7.74	0.40	2.46	0.59	1.28
0957+23	0.03	0.88	0.09	2.23	0.08	1.27	0.19	5.23	0.06	0.69	0.19	2.15
1053−00	0.09	1.77	0.43	1.42	0.23	2.52	0.32	3.35	0.00	0.01	0.79	1.66
1159+01	0.03	1.09	0.07	2.43	0.05	0.79	0.09	3.05	0.08	2.21	0.21	8.45
1213+01	0.28	0.75	0.04	0.26	0.02	0.20	0.47	8.97	0.41	1.35	0.29	1.02
1228−01	0.06	1.69	0.03	0.19	0.06	0.81	0.21	2.85	0.02	0.10	1.95	3.94
1312+23	0.05	1.71	0.10	0.89	0.59	7.12	0.88	11.1	0.39	3.10	1.97	4.62
1413+42	0.12	3.14	0.58	1.01	n.a.	n.a.	0.19	3.13	0.47	2.69	0.49	2.06
1603+30	0.01	0.06	0.50	3.21	0.35	4.12	0.46	9.00	0.24	2.44	0.60	3.83
1624+37	0.02	0.49	0.08	0.68	0.05	0.58	0.34	5.07	0.38	3.86	0.90	3.43
1625+48	0.02	0.60	0.31	1.23	0.07	0.55	0.37	2.83	n.a.	n.a.	0.28	1.18

Table 4.5: Maximum fractional variability index and the corresponding significance for the comparison sample. Superscripts indicate observational frequencies in GHz. (n.a.= not available).

ID	$Var_{\Delta S}^{1.4}$	$\sigma_{Var}^{1.4}$	$Var_{\Delta S}^{2.6}$	$\sigma_{Var}^{2.6}$	$Var_{\Delta S}^{4.8}$	$\sigma_{Var}^{4.8}$	$Var_{\Delta S}^{8.4}$	$\sigma_{Var}^{8.4}$	$Var_{\Delta S}^{10.5}$	$\sigma_{Var}^{10.5}$
1415+340	n.a.	n.a.	0.01	0.05	0.69	4.56	0.02	0.25	0.02	0.04
1501+340	0.04	0.94	0.34	1.78	0.07	0.76	0.27	2.31	0.34	1.24
1510+240	0.06	1.82	0.11	0.60	0.16	1.77	0.02	0.19	0.03	0.07
1644+340	0.00	0.04	0.38	1.56	0.55	3.55	0.47	3.09	0.22	0.40
2207+010	n.a.	n.a.	0.85	4.20	0.33	2.87	0.71	5.88	0.93	4.18
2217+003	n.a.	n.a.	0.00	0.01	n.a.	n.a.	0.25	1.76	0.30	0.50
2323+003	n.a.	n.a.	0.25	0.90	0.13	1.46	n.a.	n.a.	n.a	n.a

if this condition is applied, may indicate that this value is too high to reveal any possible flux density fluctuation in our sample. We therefore approached the question of how active a source must be to be considered variable and, in particular, which values $Var_{\Delta S}$ and σ_{Var} have to be assumed in order to provide a reliable variability threshold for our sources. After analyzing the set of fractional variability indices and the statistical significances collected in our sample, we chose a borderline of $Var_{\Delta S} > 0.25$ for the fraction of sources showing $\sigma_{Var} > 4$ de Vries et al. (2004). This limit correspond to variations of the flux density greater than 25%. This estimation of the variability threshold likely includes weak variations of the flux density that may occur in the fainter sources of our sample. In order to distinguish measurement errors from real variability, we only selected those sources where both conditions are satisfied at least at two frequencies. By using these criteria we intended to avoid flux density variations due to possible instrumental effects that seems to be more evident at 8.4 GHz (which is the only frequency where variability indexes are calculated by mixing data coming from different instruments: Effelsberg and VLA in different configurations).

These selection criteria lead to the determination of three variable BAL QSOs in the RBQ sample (0135−02, 1312+23 which is also the most variable source according to Montenegro-Montes et al. 2008a and 1603+30), plus one variable object (2207+010) in the comparison sample.

4.5 Discussion

4.5.1 BAL vs. non-BAL QSOs variability

About 20% of the sources of the RBQ sample showed (modest) radio flux density variability. This percentage is comparable to the fraction of variable sources found in the comparison sample (∼14%). This result seems to indicate that variability is not peculiar to BAL QSOs. Among the 15 objects contained in the RBQ sample, 12 are HiBAL QSOs and 3 are LoBAL QSOs. All three variable sources are HiBAL QSOs. While based on a rather small sample these percentages are not in agreement with those found by Ghosh & Punsly (2007) who discovered an inordinately large fraction of LoBAL QSOs (8/47=17% compared to 4/69=6% of HiBAL QSOs) in their sample of variable BAL QSOs. According to these authors these properties should be expected under the assumption that LoBAL QSOs mostly occur when the line of sight is close to the polar axis, where the outflow density is the highest.

4.5.2 Radio spectra

One way to obtain indications about the orientation of BAL QSOs consists in investigating their spectral index distribution. In particular, the relativistic beaming model for radio sources Orr & Browne (1982) unifies core-dominated (flat spectrum) and lobe-dominated (steep spectrum) radio sources by means

Table 4.6: RBQ sample spectral indices. Values were derived from observations performed in June 2009 at the VLA (8.4 and 22 GHz), and in July 2009 at Effelsberg (2.6, 4.8 and 10.4 GHz).

ID	$\alpha_{2.6}^{4.8}$	$\alpha_{4.8}^{8.4}$	$\alpha_{8.4}^{10.4}$	$\alpha_{10.4}^{22}$
0039−00	-0.06	-0.68	-1.88	-1.17
0135−02	-0.62	-0.45	-1.38	-1.01
0256−01	-1.17	-0.69	0.58	-1.23
0728+40	-	-0.52	1.65	-
0837+36	-0.80	-1.33	0.29	-2.55
0957+23	-0.55	-0.77	-0.56	-0.99
1053−00	-0.02	-0.57	-0.61	-1.75
1159+01	-0.14	0.20	-0.26	-0.11
1213+01	-0.58	-0.76	0.65	-1.90
1228−01	-0.11	-0.42	-0.23	-2.10
1312+23	-0.79	-0.76	0.43	-1.99
1413+42	-	-	-1.59	-0.81
1603+30	0.06	-0.76	-0.51	-0.59
1624+37	-0.64	-0.75	-0.49	-1.47
1625+48	-1.35	-0.97	-	-

of orientation: core-dominant objects are those viewed close to the jet axis (face-on), while lobe-dominant objects are those viewed at larger angles (edge-on). Possible correlations between the radio variability and the source spectral indices were examined in the RBQ sample by calculating $\alpha_{2.6}^{4.8}$, $\alpha_{4.8}^{8.4}$, $\alpha_{8.4}^{10.4}$ and $\alpha_{10.4}^{22}$ from the flux densities collected in 2009 (Table 4.6). The resulting values confirm spectral shapes found by Montenegro-Montes et al. (2008a) in 2006. All sources (except for the brightest QSO of the sample, 1159+01) show steep spectra (i.e. $\alpha > 0.5$) at high frequencies with a flattening below 4.8 or 8.4 GHz. Fig. 4.2 shows the spectral energy distribution (SED) for the three candidate variable BAL QSOs of the RBQ sample. In one case (the source 0135-02) even though the shape of the SED does not vary over time, the peak of the distribution clearly shifts towards lower frequencies. These characteristics lead to the conclusion that, in spite of the almost convex spectrum, this source may not be classified as genuine GPS or HFP since these objects usually keep the peak frequency fixed. For comparison, the spectrum of the candidate variable non-BAL QSO 2207+010 is plotted in Fig. 4.3. In this case, within errors the spectrum is flat reminding the typical behaviour of a core dominated, flat spectrum, variable QSO. These results appear inconsistent with a simple orientation scenario in which a variability due to face-on geometry would lead to expect flat spectrum core-dominated radio emission.

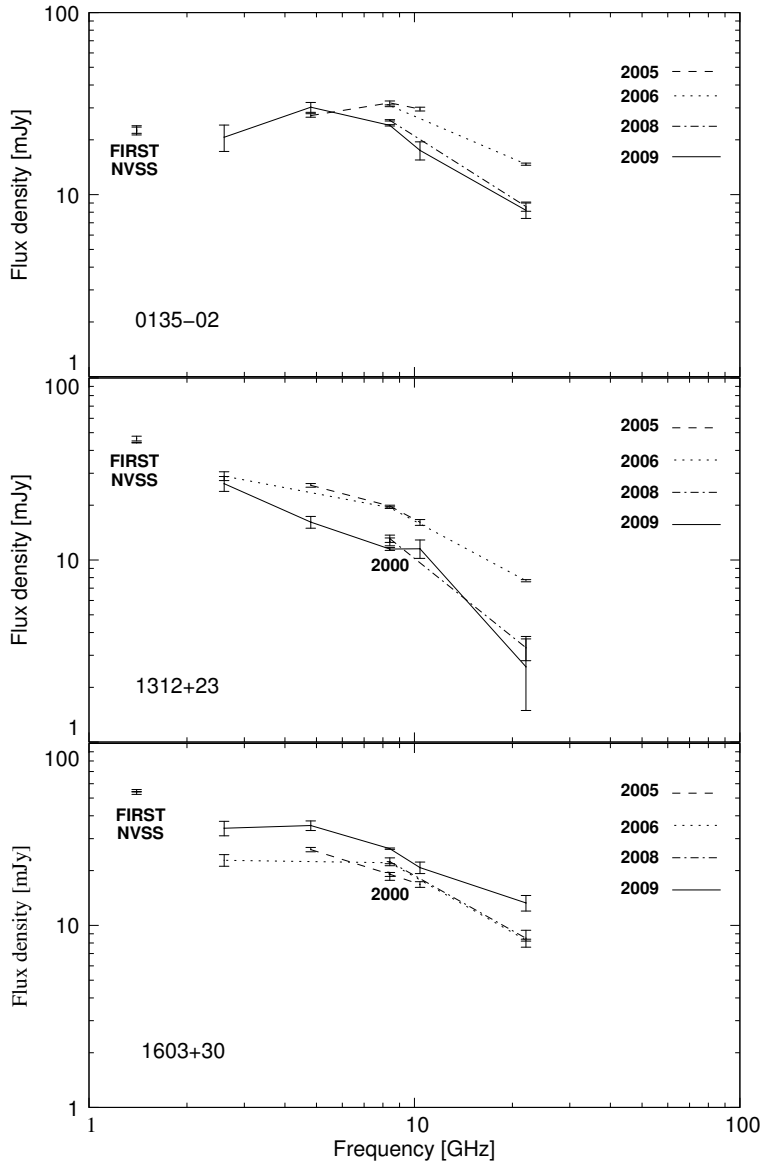

Figure 4.2: From the top: radio spectral energy distribution of the BAL QSOs 0135−02, 1312+23 and 1603+30.

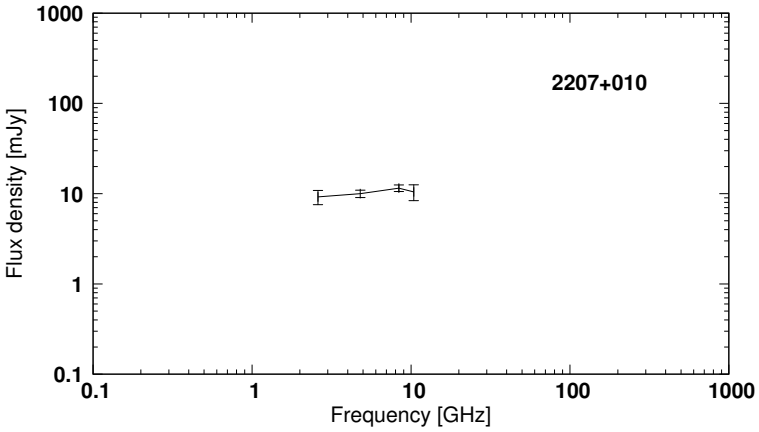

Figure 4.3: Radio spectrum of the non-BAL QSOs 2207+010. Values were collected in 2009.

4.5.3 Radio morphologies

The FIRST data at 1.4 GHz find compact component at a resolution of ∼5 arcsec for all the sources included in the RBQ sample. The only exception is given by the source 1053-00 that shows two faint components with 5 and 8σ detections. VLA (A configuration) maps at higher frequencies were produced by Montenegro-Montes et al. (2008a) who confirmed the point-like morphologies at 8.4 and 15.0 GHz and did not detect any side-lobe component in 1053−00 at these frequencies. Due to the very low flux density of the sources at high frequencies (close to the 1 mJy level) these authors could only perform an appropriate image processing for the brightest sources: 0957+23, 1159+01 and 1312+23. While the first two appeared point-like in the 43-GHz maps, the weighted maps of 1312+23 at 43 and 22 GHz revealed a northward extension coming from the central unresolved component.

Our maps at 8.4 and 22 GHz obtained from observations performed at the VLA in CnB and B configuration also showed compact structures for all sources, as expected from resolutions lower than the previous ones. Point-like structures were also found by Benn et al. (2005), who observed the source 1624+37 with the VLA at 8.4 and 22 GHz in C configuration. Very Long Baseline Interferometry (VLBI) observations of 0957+23 and 1312+23 were carried out by Jiang & Wang (2003) at 1.6 GHz. With a restoring beam of only 18.5×6.86 mas, 0957+23 appeared point-like, whereas the source 1312+23 was resolved showing a symmetric double morphology with a central core and two components covering a total extension of ∼ 150 mas (i.e. about 1 kpc) in agreement with the northern feature detected by Montenegro-Montes et al. (2008a) in their VLA maps. Recently, Montenegro-Montes et al. (2008b) observed the sources 0135−02, 0837+36, 1159+01 and 1624+37 with the VLBA at 4.8 and 8.4 GHz. The first two BAL QSOs still appear point-like at milliarcsecond-scale with linear sizes of approximately 30 × 8 pc and 19 × 8 pc respectively. The remaining two sources display extended structures at both frequencies.

The BAL QSO 1159+01 shows a compact and bright component associated with the flat spectrum radio core and at least three faint steep spectrum extended emission components that reach projected linear sizes of approximately 0.85 kpc. The source 1624+37 clearly shows a core-jet structure at both frequencies. The separation between the emission peaks of the two components is 8 mas. The variety of morphologies found for the entire RBQ sample (mainly compact geometries that in some cases appear resolved if observed at higher resolutions) is difficult to explain with a simple orientation scenario for the BAL QSOs. The reduced dimensions could be actually due either to projection effects or to intrinsically small sizes of the objects.

4.6 Conclusions

We have investigated the radio variability at different frequencies of 15 radio-loud BAL QSOs selected from the FIRST survey. The sample includes 12 HiBAL QSOs and 3 LoBAL QSOs.

- Only a small percentage of the sample shows modest radio variability and only at higher frequencies over a time range of at least four years. Variable sources are only HiBAL QSOs and all of them show steep spectra.

- Most of them display compact radio morphologies at kpc-scale (VLA and single-dish) resolution. High resolution (pc-scale) VLBI and VLBA maps show in one case an extended lobe-dominated structure. The morphological and spectral properties at radio wavelengths of the variable sources do not provide any certain indication of the orientation of these objects. At least there is no evidence of beaming effects due to jets that are strongly aligned towards the observer's line of sight.

- This results leads to exclude a simple orientation scenario in which a variability due to face-on geometry is expected to be associated with a flat spectrum core-dominated radio emission Van der Laan (1966). This does not exclude the possibility that funnel-shaped outflows coming from the accretion disks might be responsible for the BAL features if they are observed at proper (but not polar) inclination angles (Elvis 2000). However the evolutionary model proposed for instance by Becker et al. (2000) could still be valid for these objects.

The lack of predominant variability for BAL QSOs allows reliable short-time monitoring of the flux densities, and fulfills the requirement of radio stability for the determination of their spectral energy distribution. Further observations are planned to implement the data contained in this paper, and improve the variability monitoring of these objects.

Acknowledgements

The work presented in this chapter has been carried out together with Dr. E. Salerno, and will soon be submitted to MNRAS (Salerno et al. 2012).

Table 4.7: RBQ sample flux densities at 1.4 GHz. All flux densities are in mJy. Col. 1: source ID; Col. 2,3: integrated flux density and local noise estimate at 1.4 GHz according to the FIRST catalogue; Col. 4,5: integrated flux density and mean error at 1.4 GHz according to the NVSS catalogue; Col. 6,7: fractional variability index and corresponding significance.

ID	S (NVSS)	±	S (FIRST)	±	$Var_{\Delta S}$	σ_{Var}
0039−00	19.50	0.70	21.20	1.06	0.09	1.34
0135−02	22.80	1.10	22.40	1.12	0.02	0.25
0256−01	22.30	0.80	27.60	0.15	0.24	6.52
0728+40	17.20	0.60	16.80	0.13	0.02	0.65
0837+36	-	-	27.10	0.17	-	-
0957+23	136.90	4.10	140.50	0.14	0.03	0.88
1053−00	22.70	1.10	24.66	0.15	0.09	1.77
1159+01	275.60	8.30	268.48	0.14	0.03	0.86
1213+01	27.50	0.90	22.93	1.08	0.20	3.14
1228−01	29.10	1.00	30.81	0.14	0.06	1.69
1312+23	46.50	1.40	44.10	0.13	0.05	1.71
1413+42	16.80	0.60	18.74	0.15	0.12	3.14
1603+30	54.10	1.70	54.20	0.14	0.00	0.06
1624+37	55.60	1.70	56.44	0.14	0.02	0.49
1625+48	26.00	0.90	25.45	0.14	0.02	0.60

Table 4.8: RBQ sample flux densities at 2.6 GHz. All flux densities are in mJy. Col. 1: source ID; Col. 2,3: integrated flux density and corresponding uncertainty measured in June 2006 at the Effelsberg telescope; Col. 4,5: integrated flux density and corresponding uncertainty measured in July 2009 at the Effelsberg telescope; Col. 6,7: fractional variability index and corresponding significance.

ID	S (2006)	±	S (2009)	±	$Var_{\Delta S}$	σ_{Var}
0039−00	-	-	19.03	3.13	-	-
0135−02	-	-	20.68	3.41	-	-
0256−01	-	-	22.16	7.50	-	-
0728+40	6.70	1.50	-	-	-	-
0837+36	50.40	1.60	58.99	2.82	0.17	2.65
0957+23	93.70	2.40	102.32	3.03	0.09	2.23
1053−00	13.60	1.60	19.49	3.82	0.43	1.42
1159+01	133.90	2.00	142.97	3.14	0.07	2.43
1213+01	23.00	1.70	22.13	2.86	0.04	0.26
1228−01	19.40	1.60	18.79	2.80	0.03	0.19
1312+23	28.90	1.60	26.27	2.46	0.10	0.89
1413+42	7.60	2.90	11.98	3.24	0.58	1.01
1603+30	22.80	1.70	34.16	3.11	0.50	3.21
1624+37	33.50	1.60	36.19	3.64	0.08	0.68
1625+48	17.60	1.50	23.02	4.16	0.31	1.23

Table 4.9: RBQ sample flux densities at 4.8 GHz. All flux densities are in mJy. Col. 1: source ID; Col. 2,3: integrated flux density and corresponding uncertainty measured from January to October 2005 at the Effelsberg telescope; Col. 4,5: integrated flux density and corresponding uncertainty measured in July 2009 at the Effelsberg telescope; Col. 6,7: fractional variability index and corresponding significance. Observation performed in 2003 Benn et al. (2005)

ID	S (2005)	±	S (2009)	±	$Var_{\Delta S}$	σ_{Var}
0039−00	19.30	0.60	18.37	1.44	0.05	0.60
0135−02	27.20	0.60	30.22	1.89	0.11	1.53
0256−01	12.00	0.50	10.80	0.73	0.11	1.36
0728+40	6.40	0.70	5.10	0.46	0.25	1.55
0837+36	30.20	2.30	36.22	2.27	0.20	1.86
0957+23	78.70	1.10	72.97	4.38	0.08	1.27
1053−00	15.70	0.60	19.28	1.29	0.23	2.51
1159+01	137.80	1.70	131.25	8.07	0.05	0.79
1213+01	15.20	0.50	15.46	1.18	0.02	0.20
1228−01	18.60	0.50	17.58	1.15	0.06	0.82
1312+23	25.70	0.60	16.15	1.20	0.59	7.11
1413+42	8.80	0.70	-	-	-	-
1603+30	26.10	0.70	35.34	2.13	0.35	4.13
1624+37	23.30	1.10	24.47	1.68	0.05	0.58
1625+48	9.40	0.70	10.08	1.02	0.07	0.55

Table 4.10: RBQ sample flux densities at 10.4 GHz. All flux densities are in mJy. Col. 1: source ID; Col. 2,3: flux density and corresponding uncertainty measured from January to October 2005 at the Effelsberg telescope; Col. 4,5: integrated flux density and corresponding uncertainty measured in July 2009 at the Effelsberg telescope; Col. 6,7: fractional variability index and corresponding significance. Observation performed in 2004 Benn et al. (2005)

ID	S (2005)	±	S (2009)	±	$Var_{\Delta S}$	σ_{Var}
0039−00	9.70	0.40	8.39	0.57	0.16	1.89
0135−02	29.50	0.70	17.50	2.00	0.69	5.66
0256−01	5.90	0.40	8.28	0.69	0.40	2.98
0728+40	1.60	0.30	1.85	0.97	0.16	0.25
0837+36	13.00	0.40	18.26	2.10	0.40	2.46
0957+23	39.80	1.20	42.10	3.13	0.06	0.69
1053−00	12.30	0.60	12.29	1.44	0.00	0.01
1159+01	150.60	3.70	139.30	3.53	0.08	2.21
1213+01	8.20	0.50	11.60	2.46	0.41	1.35
1228−01	13.50	0.70	13.26	2.35	0.02	0.10
1312+23	16.10	0.60	11.54	1.34	0.39	3.10
1413+42	12.70	0.40	8.66	1.45	0.47	2.69
1603+30	16.80	0.60	20.77	1.51	0.24	2.44
1624+37	10.50	0.80	14.47	0.65	0.38	3.86
1625+48	6.30	0.20	-	-	-	-

Table 4.11: RBQ sample flux densities at 8.4 GHz. All flux densities are in mJy. Col. 1: source ID; Col. 2,3: flux density and assumed 5 per cent error as measured in October 1997 at the VLA in D configuration Becker et al. (2000); Col. 4,5: flux density and assumed 5 per cent error as measured in January 1998 at the VLA in A configuration Becker et al. (2000); Col. 6,7: flux density and corresponding uncertainty measured in March 2004 Benn et al. (2005); Col. 8,9: flux density and corresponding uncertainty measured from January to October 2005 at the Effelsberg telescope; Col. 10,11: flux density and corresponding uncertainty measured from February to March 2006 at the VLA in A configuration; Col. 12,13: flux density and corresponding uncertainty measured in February 2008 at the VLA in CnB configuration; Col. 14,15: flux density and corresponding uncertainty measured in June 2009 at VLA in B CnB configuration; Col. 16,17: flux density and corresponding uncertainty measured in July 2009 at the Effelsberg telescope; Col. 18,19: maximum fractional variability index and corresponding significance.

ID	S (1997)	±	S (1998)	±	S (2004)	±	S (2005)	±	S (2006)	±	S (2008)	±	S (2009)	±	S (2009)	±	$Var_{\Delta S}^{max}$	σ_{Var}
0039−00	-	-	-	-	-	-	12.00	0.40	12.30	0.10	11.50	0.20	11.80	0.20	12.55	0.52	0.09	1.88
0135−02	-	-	-	-	-	-	31.90	0.80	30.80	0.40	25.60	0.20	24.03	0.20	23.52	0.92	0.36	6.87
0256−01	-	-	-	-	-	-	7.20	0.30	7.20	0.40	6.80	0.20	8.08	0.20	7.32	0.43	0.19	4.53
0728+40	-	-	2.70	0.14	-	-	3.10	0.20	2.50	0.30	2.90	0.20	-	-	3.81	0.47	0.52	2.35
0837+36	-	-	-	-	-	-	12.10	0.80	12.50	0.10	9.20	0.40	11.57	0.40	17.18	0.95	0.87	7.74
0957+23	51.30	2.57	-	-	-	-	48.50	1.20	53.20	0.50	52.80	2.60	56.30	0.20	47.46	1.68	0.19	5.23
1053−00	-	-	-	-	-	-	11.80	0.40	13.10	0.10	10.60	0.70	13.30	0.30	14.01	0.74	0.32	3.35
1159+01	-	-	-	-	-	-	158.00	2.00	160.80	1.20	155.20	7.70	159.90	0.50	147.20	4.29	0.09	3.05
1213+01	-	-	-	-	-	-	9.70	0.30	11.60	0.10	7.90	0.40	10.70	0.20	10.10	0.77	0.47	8.97
1228−01	-	-	-	-	-	-	15.50	0.40	16.90	0.20	14.90	0.70	14.70	0.30	13.91	1.03	0.21	2.85
1312+23	12.30	0.62	12.60	0.63	-	-	19.80	0.20	19.40	0.20	13.10	0.60	11.50	0.20	10.54	0.81	0.88	11.10
1413+42	11.30	0.57	-	-	-	-	13.40	0.30	13.40	0.10	12.50	0.60	12.30	0.20	12.15	0.78	0.19	3.13
1603+30	18.60	0.93	18.10	0.91	-	-	19.10	0.50	22.10	0.30	22.40	1.10	26.40	0.20	23.16	1.29	0.46	9.00
1624+37	-	-	-	-	15.00	0.09	-	-	-	-	20.10	1.00	18.00	0.20	16.07	0.92	0.34	5.07
1625+48	-	-	-	-	-	-	8.00	0.20	7.00	0.20	7.50	0.40	6.50	0.20	5.86	0.73	0.37	2.83

Table 4.12: RBQ sample flux densities at 22 GHz. All flux densities are in mJy. Col. 1: source ID; Col. 2,3: flux density and corresponding uncertainty measured in March 2004 Benn et al. (2005); Col. 4,5: flux density and corresponding uncertainty measured from February to March 2006 at the VLA in A configuration; Col. 6,7: flux density and corresponding uncertainty measured in February 2008 at the VLA in CnB configuration; Col. 8,9: flux density and corresponding uncertainty measured in June 2009 at the VLA in B CnB configuration; Col. 10,11: maximum fractional variability index and corresponding significance.

ID	S (2004)	±	S (2006)	±	S (2008)	±	S (2009)	±	$Var_{\Delta S}^{max}$	σ_{Var}
0039−00	-	-	2.20	1.20	1.60	0.40	3.50	0.20	1.19	4.25
0135−02	-	-	14.70	0.20	8.60	0.50	8.20	0.80	0.79	7.88
0256−01	-	-	2.20	0.30	1.90	0.20	3.30	0.20	0.74	4.95
0728+40	-	-	0.80	0.06	0.40	0.10	-	-	1.00	2.83
0837+36	-	-	2.20	0.50	1.70	0.60	2.70	0.50	0.59	1.28
0957+23	-	-	22.40	0.30	18.90	1.60	20.10	1.10	0.19	2.15
1053−00	-	-	5.90	0.70	4.50	0.90	3.30	1.40	0.79	1.66
1159+01	-	-	105.50	1.10	113.70	0.90	127.80	2.40	0.21	8.45
1213+01	-	-	3.60	0.50	3.00	0.30	2.80	0.60	0.29	1.02
1228−01	-	-	8.10	0.20	6.50	0.60	2.75	1.33	1.95	3.94
1312+23	-	-	7.70	0.10	3.30	0.50	2.59	1.10	1.97	4.62
1413+42	-	-	7.00	0.20	4.80	0.60	4.70	1.10	0.49	2.06
1603+30	-	-	8.30	0.10	8.50	0.90	13.30	1.30	0.60	3.83
1624+37	5.40	0.02	-	-	9.10	0.60	4.80	1.10	0.90	3.43
1625+48	-	-	1.90	0.30	2.30	0.30	1.80	0.30	0.28	1.18

Table 4.13: Comparison sample flux densities at 1.4 GHz. All flux densities are in mJy. Col. 1: source ID; Col. 2,3: integrated flux density and local noise estimate at 1.4 GHz according to the FIRST catalogue; Col. 4,5: integrated flux density and mean error at 1.4 GHz according to the NVSS catalogue; Col. 6,7: fractional variability index and corresponding significance.

ID	S (NVSS)	±	S (FIRST)	±	$Var_{\Delta S}$	σ_{Var}
1415+340	-	-	16.05	0.14	-	-
1501+340	19.2	0.70	18.91	0.15	0.02	0.41
1510+340	24.6	0.80	27.03	0.14	0.10	2.99
1644+340	23.4	0.80	23.80	0.14	0.02	0.49
2207+010	-	-	16.71	0.13	-	-
2217+003	-	-	20.90	0.10	-	-
2323+003	-	-	16.89	0.11	-	-

Table 4.14: Comparison sample flux densities at 2.6 GHz. All flux densities are in mJy. Col. 1: source ID; Col. 2,3: integrated flux density and corresponding uncertainty measured in June 2006 at the Effelsberg telescope; Col. 4,5: integrated flux density and corresponding uncertainty measured in July 2009 at the Effelsberg telescope; Col. 6,7: fractional variability index and corresponding significance.

ID	S (2006)	±	S (2009)	±	$Var_{\Delta S}$	σ_{Var}
1415+340	10.00	0.50	9.92	1.72	0.01	0.05
1501+340	14.50	0.73	10.78	1.95	0.34	1.78
1510+340	16.50	0.83	14.88	2.56	0.11	0.60
1644+340	13.40	0.67	18.49	3.20	0.38	1.56
2207+010	17.00	0.85	9.20	1.65	0.85	4.20
2217+003	10.00	0.50	10.03	3.12	0.00	0.01
2323+003	15.50	0.78	12.43	3.31	0.25	0.90

Table 4.15: Comparison sample flux densities at 4.8 GHz. All flux densities are in mJy. Col. 1: source ID; Col. 2,3: integrated flux density and corresponding uncertainty measured from January to October 2005 at the Effelsberg telescope; Col. 4,5: integrated flux density and corresponding uncertainty measured in July 2009 at the Effelsberg telescope; Col. 6,7: fractional variability index and corresponding significance.

ID	S (2005)	±	S (2009)	±	$Var_{\Delta S}$	σ_{Var}
1415+340	7.60	0.38	4.48	0.57	0.69	4.56
1501+340	11.70	0.59	12.51	0.89	0.07	0.76
1510+340	10.9	0.55	12.67	0.84	0.16	1.77
1644+340	8.10	0.41	12.53	1.18	0.55	3.55
2207+010	13.30	0.67	10.00	0.94	0.33	2.87
2217+003	5.50	0.28	-	-	-	-
2323+003	15.30	0.77	13.56	0.92	0.13	1.46

Table 4.16: Comparison sample flux densities at 8.4 GHz. All flux densities are in mJy. Col. 1: source ID; Col. 2,3: integrated flux density and corresponding uncertainty measured from January to October 2005 at the Effelsberg telescope; Col. 4,5: integrated flux density and corresponding uncertainty measured in July 2009 at the Effelsberg telescope; Col. 6,7: fractional variability index and corresponding significance.

ID	S (2005)	±	S (2009)	±	$Var_{\Delta S}$	σ_{Var}
1415+340	4.30	0.22	4.20	0.35	0.02	0.25
1501+340	9.50	0.48	7.50	0.73	0.27	2.31
1510+340	7.40	0.37	7.27	0.63	0.02	0.18
1644+340	5.10	0.26	7.51	0.74	0.47	3.09
2207+010	19.70	0.99	11.54	0.98	0.71	5.88
2217+003	3.10	0.16	3.88	0.42	0.25	1.76
2323+003	15.10	0.76	-	-	-	-

Table 4.17: Comparison sample flux densities at 10.4 GHz. All flux densities are in mJy. Col. 1: source ID; Col. 2,3: flux density and corresponding uncertainty measured from January to October 2005 at the Effelsberg telescope; Col. 4,5: integrated flux density and corresponding uncertainty measured in July 2009 at the Effelsberg telescope; Col. 6,7: fractional variability index and corresponding significance.

ID	S (2005)	±	S (2009)	±	$Var_{\Delta S}$	σ_{Var}
1415+340	3.90	0.20	3.83	1.69	3.83	1.69
1501+340	9.00	0.45	12.04	2.41	12.04	2.41
1510+340	6.70	0.34	6.93	3.10	6.93	3.10
1644+340	4.50	0.23	5.48	2.42	5.48	2.42
2207+010	20.20	1.01	10.46	2.10	10.46	2.10
2217+003	2.70	0.14	3.51	1.61	3.51	1.61
2323+003	15.20	0.76	-	-	-	-

Chapter 5

Morphology at high angular resolution scale

5.1 Introduction

In this chapter we present the results of an extensive observational campaign to determine the pc-scale structure and morphology of the sample of radio-loud BAL QSOs presented in chapter 2, and which SEDs were shown in chapter 3. The VLBI technique is an important tool for this kind of study, allowing one to reach the necessary resolution and sensitivity to study distant objects like BAL QSOs. This approach offers different indicators of the morphology of the radio source: (1) the detection of radio jets and lobes can give clues about the age and possibly the orientation of the QSO; (2) the projected linear size determination for compact sources can give information about the age of the radio source (Dallacasa et al. 2000); (3) the spectral index analysis allows us to discriminate between core-jet or double structure; (4) Variability with respect to the total flux density already measured with the VLA can give an extimate of the activity of the QSO, and help in determining if a compact source is seen from the polar line of sight. Thus the aim of this chapter is to help in discriminating which of the presented models could be the most probable to explain the BAL phenomenon.

5.2 Radio observations

We performed VLBI observations for 11 sources among the brightest at 1.4 GHz in the sample. We divided the sources among the VLBA and EVN, using the first (with a lower sensitivity) for the brightest ones and the latter for the faintest. Thus, in 2010 seven objects were observed with the VLBA at 5 and 8.4 GHz (C and X-band, respectively) with a total bandwidth of 64 MHz, in C and X band with an average on-source time of 1 and 2 hours respectively. Other 4 sources were observed with the EVN (JB, WB, EF, ON, MC, TR, SH, UR, NT, YS, DA, KN) at 5 GHz, with a total bandwidth of 64 MHz and an

Table 5.1: Summary of the observations.

Run	Date	Telescope	Frequencies (GHz)
1	25−26 Oct 2009	EVN	4.8
2	19, 22, 26, 28 Feb 2010	VLBA	5, 8.4
3	04, 07, 23, 26 Apr - 01, 02 May 2011	VLBA	5, 8.4

Table 5.2: Sample of 11 radio-loud BAL QSOs studied in this work. Column 2,3 and 4 are respectively RA, DEC and redshift as measured from the SDSS.

Name	RA (J2000)	DEC (J2000)	z
(1)	(2)	(3)	(4)
0044+00	00 44 44.06	+00 13 03.5	2.28
0756+37	07 56 28.24	+37 14 55.6	2.51
0816+48	08 16 18.99	+48 23 28.4	3.57
0849+27	08 49 14.27	+27 57 29.7	1.73
1014+05	10 14 40.35	+05 37 12.6	2.01
1102+11	11 02 06.66	+11 21 04.9	2.35
1237+47	12 37 17.44	+47 08 07.0	2.27
1304+13	13 04 48.06	+13 04 16.6	2.57
1327+03	13 27 03.21	+03 13 11.2	2.83
1406+34	14 06 53.84	+34 33 37.3	2.56
1603+30	16 03 54.15	+30 02 08.7	2.03

average on-source time of 2 hours.

In 2011 we obtained additional observing time at the VLBA, and we observed other 3 sources among the brightest not yet observed in the previous runs, in C and X band, with an average on-source time of 3 and 4 hours respectively.

The data collected with the VLBA during 2010 were correlated at the VLBA correlator in Socorro, while in 2011 the new DiFX software correlator was available (Deller et al. 2011). The data obtained with the EVN were correlated at the JIVE correlator in Dwingeloo. A summary of the observations is reported in Table 5.1, while in Table 5.2 we report some basic information on the 11 BAL QSOs presented here. Given that most of the objects are quite weak, phase referencing has been used with a nearby calibrator chosen from the VLBA calibrator list.

If we also consider the two sources (1159+01 and 1624+37) already presented by Montenegro-Montes et al. (2008b), we end up with a total of 13 out of 25 BAL QSOs in the whole sample with known parsec-scale radio images.

5.3 Data analysis and results

Both EVN and VLBA data underwent to standard calibration procedures for phase referencing observations. All the data reduction and image analysis have been performed by means of the AIPS software, following usual procedures once editing of raw visibilities and of system temperature measurements were carried out. The calibration flux density scale accuracy can be estimated to be within ±5%. Solutions for reference sources were transferred to the appropriate target and an initial wide field (typically 1" wide) was imaged in order to find the target source. Once this happened, a smaller field was considered with the application of appropriate shifts in RA and DEC to have the radio emission at the centre. Then a few iterations of phase self-calibration were performed. The final images are shown in Figures 5.1.

Once final images were obtained, we carried out a 2-D Gaussian fitting solving for component position, flux density, size and position angle. The resulting information is reported in Table 5.3. The centroids of the single components fits were used to calculate the total projected linear size of the source.

In the following we are going to briefly describe each individual source. The overall radio-spectrum of the sources can be found in chapter 3.

5.3.1 Results from VLBA observations

In this section, the pc-scale structure of the BAL QSOs observed with the VLBA is briefly discussed. The typical resolution of the image is ∼4 mas and ∼2 mas at 5 and 8.4 GHz respectively. The spectral indices for the single components have been calculated using the integrated flux density from the gaussian fit.

0044+00

This source presents a resolved structure in both C and X-band images. In the first one, three non-aligned components are present: while for A and B a Gaussian fit was possible, for C it did not converge, and only an estimation of the flux density with IMSTAT was possible. In X-band only components A and C are visible, suggesting a steep spectral index for B that makes drop the flux density under the significance level. Component A has a rather flat spectral index (-0.52 ± 0.27) and could be classified like the core. For components A and C we obtained major and minor axes of respectively 2.7 mas (23 pc) and 1.3 mas (11 pc) for A and 3.6 mas (30 pc) and 1.1 mas (9 pc) for C, extracted from the gaussian fits of the X-band image, while for component B we performed a fit in of the C-band image, obtaining major and minor axes of 6.0 mas (50 pc) and 2.3 mas (19 pc). The total dimesion of the source, calculated as the distance between the centroids of A and C components in X-band, is 5.6 mas, corresponding to 48 pc.

Table 5.3: The 11 radio-loud BAL QSOs studied in this work. In column 2 the component is specified, column 3 and 4 are flux densities measured with the VLBA or EVN, column 5 is the spectral index for the components, column 6 and 7 are the VLA flux densities as presented in chapter 3, column 8 is the projected linear size in pc of the source, column 9 the morphology classification (CJ: core-jet; D: double; S: symmetric; U: unresolved) and column 10 the telescope used for the observations. Superscripts in the last column indicate the run number of the VLBA observations, according to the key in Table 5.1.

Name	comp.	$S_{4.8}^{VLBI}$	$S_{8.4}^{VLBI}$	SI	$S_{4.8}^{VLA}$	$S_{8.4}^{VLA}$	Proj. LS	Morphology	Telescope
(1)	(2)	(3)	(4)	(5)	(6)	(7)	(8)	(9)	(10)
0044+00		33.0±2.6	20.8±1.9	-	34.2±1.8	25.5±0.6	48	CJ	VLBA[3]
	A	25.0±2.5	19.0±1.9	−0.52±0.27					
	B	6.5±0.8	-	-					
	C	1.5±0.3	1.8±0.2	0.35±0.44					
0756+37		147.4±10.6	121.0±8.6	-	226.2±2.0	142.1±1.8	17	D	VLBA[2]
	A	88.2±8.8	72.2±7.2	−0.38±0.27					
	B	59.2±5.9	48.8±4.8	−0.37±0.27					
0816+48		26.9±2.7	-	-	31.4±0.5	19.5±0.5	<51	CJ	EVN
0849+27		14.8±1.3	11.8±0.2	-	-	-	33	CJ	VLBA[3]
	A	2.2±0.3	-	-					
	B	12.6±1.3	11.8±0.2	−0.12±0.20					
1014+05		22.1±1.7	-	-	34.5±0.6	25.1±0.5	222	S	EVN
	A	10.3±1.1	-	-					
	B	7.4±1.0	-	-					
	C	2.7±0.6	-	-					
	D	1.7±0.5	-	-					
1102+11		38.8±3.4	16.9±1.8	-	39.8±0.8	19.9±0.7	35	D	VLBA[2]
	A	28.1±3.0	16.9±1.8	−0.97±0.29					
	B	10.7±1.7	-	-					
1237+47		54.4±4.5	84.6±6.6	-	62.3±1.0	61.6±1.6	40	S	VLBA[2]
	A	37.8±4.0	46.9±5.0	0.41±0.29					
	B	5.2±1.2	16.1±2.6	2.15±0.54					
	C	11.4±1.7	-	-					
	C1	-	14.3±2.9	-					
	C2	-	7.3±1.7	-					
1304+13		20.1±1.6	15.1±0.5	-	24.6±0.5	17.1±0.5	44	CJ	VLBA[3]
	A	7.2±0.7	3.2±0.3	−1.54±0.26					
	B	12.9±1.4	11.2±0.3	−0.27±0.21					
	C	-	0.7±0.3	-					
1327+03		80.6±8.0	-	-	79.5±1.7	56.5±0.7	<48	U	EVN
1406+34		81.2±11.4	195.1±20.6	1.7±0.3	312.8±3.1	276.3±3.0	<24	U	VLBA[2]
1603+30		43.3±2.6	-	-	34.5±2.4	26.9±0.6	80	S	EVN
	A	18.1±1.8	-	-					
	B	8.8±1.0	-	-					
	C	16.4±1.6	-	-					

The composite morphology of this source could suggest a re-oriented jet, like suggested in Kunert-Bajraszewska et al. (2007) to explain another case of peculiar BAL QSO. The whole radio-spectrum presents flattening at ∼5 GHz, but no clear peak in the GHz range is present, so a classification as a young GPS source is not possible. Maybe intermittent activity can be an issue in this case.

0756+37

In both VLBA images in C and X-bands we resolve the radio source into two components, separated by 2.0 mas in X-band (17 pc at the redshift of the object) in p.a. $\sim 7°$. Gaussian fits gave major axes of 1.9 mas (16 pc) and 1.8 mas (15 pc) and minor axes of 0.8 (7 pc, for both) for the West and East component respectively. By taking into account the integrated flux densities (see Table 5.3) both components have a rather flat spectral index (-0.38 ± 0.27 and -0.37 ± 0.27) and therefore none of them can be classified as the core. They could be two mini-hotspots of a very compact and young radio-source. This is consistent with the total radio spectrum, showing a peak at 8.7 GHz in the rest-frame, typical of young GPS sources.
The flux densities measured with the VLA in both bands are significantly bigger (∼54% in C band and ∼17% in X band): this is generally ascribable to a diffuse emission not detectable with the sensitivity threshold of these VLBI observations. No low-frequency components are present in the overall radio spectrum of this source that could be responsible for this emission.

0849+27

This source was already resolved in the FIRST survey (VLA at 1.4 GHz, see chapter 3) showing three components with a projected linear size of 382 kpc. The VLBA provides information on the central and most compact component: it is resolved into two components well visible in C-band (A and B) separated by 3.8 mas (33 pc). In X-band only B could be detected, with major and minor axis of 4.1 mas (35 pc) and 2.6 mas (22 pc), and a spectral index of -0.12 ± 0.20 (flat) conferming the previous classification of this component as the core. We can extract major and minor axes for the A component from the C band map, resulting in 4.5 mas (39 pc) and 1.3 mas (11 pc) respectively.

1102+11

A double structure is visible in C-band for this source, with a strong component in the centre (A) and a fainter component toward NE (B), separated by 4.1 mas (35 pc). The first has a major and minor axes in this last band of 2.9 mas (24 pc) and 1.2 mas (10 pc), while the second is present only in C band with a major and minor axes of 4.1 mas (34 pc) and 2.2 mas (18 pc). The spectral index is -0.97 ± 0.29 for the A component, that thus could be a lobe,

while the B component probably has an even steeper spectral index, since the flux density is smaller than the 3-σ significance signal in X band, and could be a second lobe.
The source presents a convex spectrum in the radio domain, but more observations at low frequencies are needed to clearly identify the turn-over frequency. If a peak was present in the GHz range, this object could be a GPS, probably young, source.

1237+47

This source shows a three-components structure in C band, with the strongest in the centre (A) and the other two toward NW (B) and SE (C). In X band, component C is resolved in two sub components (C1 and C2), both aligned with A and B. Component A has a flat spectral index (0.41±0.29) and thus could be interpreted as the core, while B and C1 are elongated emissions starting from A, with similar flux density in X band, and could be the inner part of the jets, with an additional lobe (C2) visible in the direction of C1. The projected linear size from X band is 4.7 mas (40 pc). Major and minor axes of the 4 components are 3.2 mas (27 pc) and 1.2 mas (10 pc) for A, 3.1 mas (26 pc) and 1.7 mas (15 pc) for B, 3.9 mas (33 pc) and 1.8 mas (15 pc) for C1, 3.6 mas (31 pc) and 1.1 mas (9 pc) for C2.
From our previous radio observations of this source we know that it presents a convex spectrum, with a peak at 11 GHz in the rest-frame: with this additional high-resolution observations we can catalogue this source as High Frequency Peaker (HFP) following the definition by Dallacasa et al. (2000), since dimensions are <0.1 kpc and the turn-over frequency is >5 GHz. This object is most probably a young radio source. Moreover, it presents a greater flux density in X band than in previous VLA measurements (∼27%): this could indicate an active phase in which new components are likely to be formed in short times, causing a variability in the flux density. The time interval between VLA and VLBA observations is ∼7 months, with a σ_{var}=3.4, following the definition of the variability significance from Zhou et al. (2006).

1304+13

It was possible to resolve this source both in C and X bands: two components are present in the former, A and B, connected by an elongation of the brightest one (B). In X band a third component (C) is visible, matching with the previous elongation, but the Gaussian fit did not converge in this case so we used IMSTAT to estimate the flux density. In X band the two fitted components A and B have major and minor axes of 1.9 mas (16 pc) and 1.0 mas (9 pc) in the first case, 1.9 mas (16 pc) and 1.2 mas (10 pc) in the second case. Component B, that still presents a faint elongation toward NE, has a flat spectrum and could be the core, while A a lobe. With an asymmetric structure, this source could present a Doppler boosted emission, typically resulting in

core-jet structures, and corresponding to viewing angles closer to the jet axis. The total projected linear size of the source is 5.4 mas (44 pc). The overall spectrum is steep, and does not present a peak in the investigated GHz range.

1406+34

This is a case of an unresolved source, with an upper limit to the linear size from the X band image of 24 pc of the major axis (2.9 mas) and 11 pc of the minor axis (1.3 mas). From the flux densities in the two bands we obtain an inverted spectral index equal to 1.7±0.3. In chapter 3 we have presented the complete radio-spectrum of this source, and the synchrotron emission peak lies at 19.2 GHz (rest-frame), thus the two frequencies observed with the VLBA lie in the absorbed part of the spectrum, where the spectral index is still positive. The first contour in C band seems to present a symmetric structure towards NW and SE, but since we have only a 3-σ signal for this structure it is not possible to give a clear interpretation.
It is worth to notice that the flux density measured with the VLA at 5 GHz is ∼4 times the one we obtained with the VLBA, and at 8.4 GHz it is ∼41% greater: this can suggest a diffuse emission that drops below the sensitivity limit at high resolution. An emission at 325 MHz from a low frequency component has been measured during the WENSS survey (de Bruyn et al. 2000) and can be related to the missing flux. This does not suggest a young age for this source, since low-frequency diffuse emission can be interpreted as old or remainder of a previous activity.

5.3.2 Results from EVN observations

In this section we discuss the different morphologies found through EVN observations in C-band. The typical resolution of these images is ∼7 mas.

0816+48

This source shows an elongation toward SE in C band. From the major and the minor axis of the Gaussian fit (6.8 and 4.7 mas) we can infer a projected linear size of 51 and 35 pc, respectively. It was not possible to catalogue the spectrum of this source from our previous observations, since abrupt changes in the SED did not allow a clear interpretation, but the VLA map at 8.4 GHz already showed an elongation toward SW, not matching with the one present here, with a major and minor axis of 29 and 14 arcsec, corresponding to 217 and 105 kpc respectively. This could be another case of intermittent activity with a change in the jet orientation between the two phases, but more observations at the intermediate VLA resolution are needed to confirm this hypothesis.

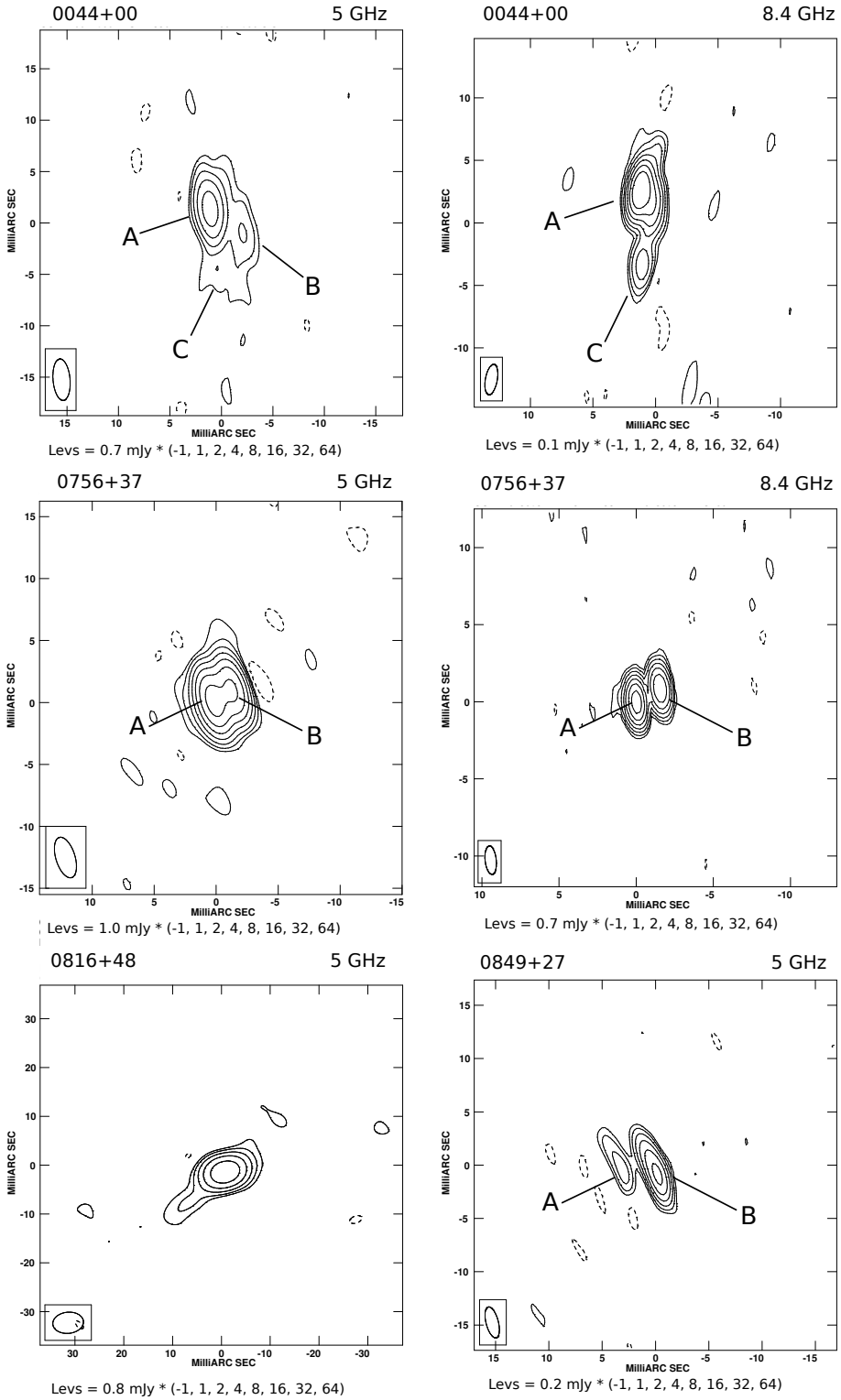

Figure 5.1: VLBI maps of the 11 BAL QSOs studied here. The synthesised beam size is shown in the lower left corner of each map. Levels are 3-σ multiples, according to the legend.

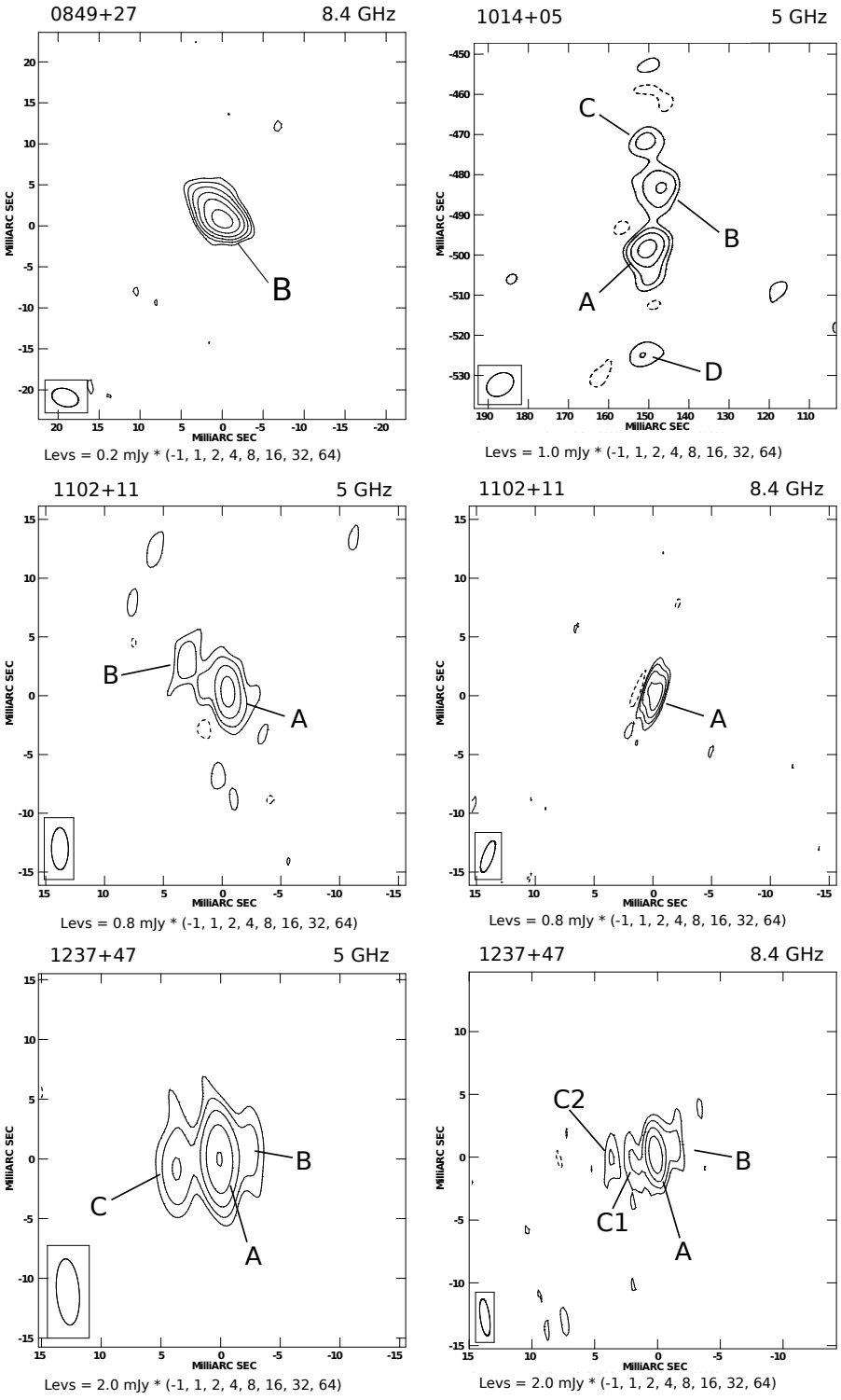

Figure 5.1: Continued.

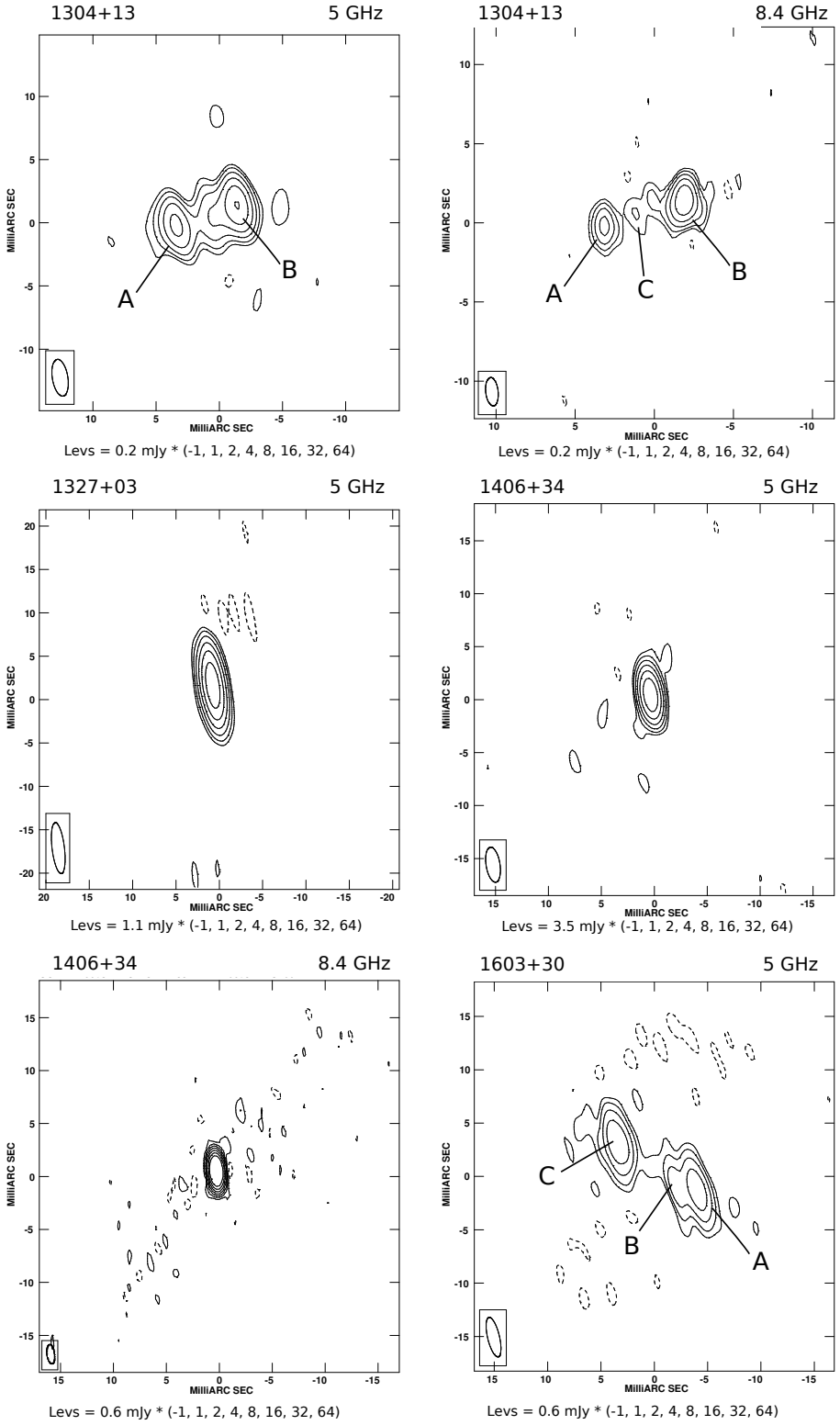

Figure 5.1: Continued.

1014+05

This source presents a complex morphology: the probable central core is clearly visible as the brightest component (A), while a second (B) and a third (C) component are present toward the north, and a fourth (D) symmetrically toward south. This could be interpreted as a core-triple lobe structure, with two older faint components (C and D) and a younger lobe (B) with a more visible emission (7.4±1.0 mJy). Major and minor axes of the components are 7.4 mas (63 pc) and 6.0 mas (51 pc) for A, 8.9 mas (75 pc) and 7.3 mas (62 pc) for B, 7.8 mas (66 pc) and 5.4 mas (46 pc) for C, 7.7 mas (65 pc) and 4.8 mas (40 pc) for D.
The distance between C and D components is 25.8 mas, with a corresponding projected linear size of 222 pc. We found a power law spectrum for this source, but more data below 1.4 GHz are needed to exclude any turn-over frequency in the MHz range.
Also in this case the flux density from the VLA is greater than the one from these observations (∼57%): but with no data in the MHz frequency range it is not possible to deduce an origin for this emission.

1327+03

This is an unresolved source. The measured flux density is 80.6±8.0 mJy. The upper limit for the linear size is 48 pc (6.0 mas) and 14 pc (1.7 mas), respectively on major and minor axis, but the beam is considerably elliptical in this map so this is just an indicative value. A power law spectrum down to 1.4 GHz does not show the turn-over frequency for this source.

1603+30

In this case a symmetric structure can be seen: this could be another example of a core-double-lobe BAL QSO, dominated by the lobes emission. The separation between A and C components is 9.3 mas, with a projected linear size of 80 pc. Major and minor axes for the three components are 4.5 mas (38 pc) and 1.8 mas (16 pc) for A, 4.4 mas (38 pc) and 1.9 mas (16 pc) for B, 4.4 mas (38 pc) and 1.9 mas (16 pc) for C. This source presents a convex radio spectrum, with a peak frequency at 4.2 GHz in the rest-frame and thus can be classified as a young GPS source.
The VLA map at 22 GHz showed already a core-lobe morphology, towards S, with an angular size of 2 arcsec, corresponding to 17 kpc: these dimensions are more typical of CSS sources (1-20 kpc), though the overall spectrum is typical of GPS sources. The structure seen with the EVN is not aligned with the one seen with the VLA, again a complex history seems to be present to justify the different morphologies of the same object at different scales.
This is another case of a young source with a greater flux density at VLBI resolution than in previous VLA observations (∼21%): the time-baseline between

the two measurements is ∼3 months, with a σ_{var}=2.5, thus not so statistically significant.

5.4 Discussion

A previous VLBI study by our group (Montenegro-Montes et al. 2008b), based on a fainter sample of radio-loud BAL QSOs presented in Montenegro-Montes et al. (2008a), underlines different morphologies and orientations, supporting the evolutionary scenario as the most consistent with the results. In that work a total of 5 sources were observed with the VLBA, resulting in 2 resolved sources (40%). In this work we have studied 11 sources and 9 present a resolved structure (∼82%) with different morphologies. Three of them (0816+48, 0849+27 and 1603+30) were already resolved at the intermediate angular resolution of our previous VLA observations, together with 1103+11 (not observed in this work) resulting in linear sizes up to hundreds of kpc. If we also consider the sources 1159+01 and 1624+37, published in Montenegro-Montes et al. (2008b) and part of our sample, we end up with a total of 11 resolved sources out of 13 (∼85%). In 1159+01 a central core is present with two faint symmetric extensions and another two components toward SW, while in the case of 1624+37 a core-jet structure has been detected. This confirms the variety of geometries we have found in the present work, and suggest a variety of orientation with respect to the line of sight, in agreement with the results from chapter 2.

Considering the literature, 33 BAL QSOs have been observed until now at VLBI resolution by other authors (Jiang & Wang 2003; Kunert-Bajraszewska et al. 2007; Liu et al. 2008; Montenegro-Montes et al. 2008b; Gawrónski & Kunert-Bajraszewska 2011): with this work we add further 11 sources, improving the statistics about morphology. In previous works 8 sources out of 33 (∼24%) resulted unresolved, while the remaining show a variety of morphology, including core-jet, symmetrical or complex. In some cases a re-orientation or jet-precession scenario have been proposed (Kunert-Bajraszewska et al. 2007; Gawrónski & Kunert-Bajraszewska 2011) to explain the peculiar morphology. These results, as a whole, are in agreement with the findings of this work, both in term of the fraction of the unresolved sources and of the possible morphologies and orientations present in our sample.

After a decade of VLBI observations, BAL QSOs do not seem to be predominantly unresolved, or to present an univocal morphology. In some cases these sources can be compact, with a projected linear size under 20 kpc, or even extremely compact, under 1 kpc, but there are examples of extended sources (hundreds of kpc), like 0849+27, presenting BAL features, or cases of BAL QSOs with traces of diffuse emission, probably related to a low frequency component, so the interpretation of BAL QSOs as young sources seems to be over-simplistic. On the other hand, the variety of orientation found does not allow one to explain this particular sub-sample of QSOs as likely to be seen

from a particular line of sight, as suggested by the orientation model (Elvis 2000). The outflows at the origin of the BAL features should thus be present at various orientations with respect to the jet-axis, and in various phases of the QSO evolutionary track. Maybe more answers can be found investigating the complex nuclear activity of these objects, directly linked to the physical conditions of the central environment.

5.5 Conclusions

We present the results of EVN and VLBA observations of the brightest radio-loud BAL QSOs of our sample. 11 sources were observed and a pc-scale mapping together with a spectral analysis of their components were realized. We can summarise our conclusions as follows:

- 9 of 11 sources (82%) present a resolved structure, and various morphologies are visible: double, core jet and symmetric structures have been found, so different orientations can be argued. The percentage of resolved sources is comparable with the general results from previous works in the literature.

- The projected linear sizes at this scale are between tens and hundreds of parsecs, but some sources already showed a resolved structure in our previous VLA observations, increasing the upper limit for dimensions of BAL QSOs to hundreds of kpc, comparable with the dimensions of common radio sources.

- The missing flux density between VLA and VLBI observations can suggest in some cases a diffuse emission too faint to be detected with these observations. In one case (1406+34) it can be due to a low-frequency component, probably the remnant of a previous activity of the AGN. A complex history can be supposed also for other sources, when a re-oriented jet seems to be at the origin of the complex morphology.

- The variety of dimensions and spectral characteristics found in this VLBI observations and from our previous work (see chapter 3, Bruni et al. 2012) seems to exclude a simple explanation for all BAL QSOs as young, compact, objects. At the same time, given the variety of morphologies that can be found, a particular orientation is unlikely to be present: the outflows originating the BAL features are then likely to be present both in young and older QSOs, at various orientations with respect to the jet axis.

Chapter 6

The dust component in the mm-wavelength domain

6.1 Dust in young radio sources

The continuum emission of dust, in the rest-frame Far Infrared domain (FIR) , can be detected at mm-wavelength for objects with z$\sim$2. Objects enshrouded by gas and dust can host star-formation regions, and thus show high star-formation rates, that may indicate a young age of the galaxy. A flux density excess in the FIR could be an indicator of a different age for BAL QSOs with respect to the non-BAL QSO population, and thus help in discriminating between the orientation and the evolutionary models.

There are two major works presenting (sub)mm observations on samples of BAL QSOs. Willott et al. (2003) showed SCUBA measurements on a sample of 30 radio-quiet BAL QSOs and conclude that there is no difference between BAL QSOs and a comparison sample of non-BAL QSOs. On the other hand, Priddey et al. (2007) based on SCUBA observations of 15 BAL QSOs find tentative evidence for a dependence of submm flux densities on the equivalent width of the characteristic CIV BAL which *'suggests that the BAL phenomenon is not a simple geometric effect (...) but that other variables, such as evolutionary phase, (...) must be invoked'*.

The main difference of the above samples compared to our target sample is the radio-loudness of our sources. With the radio-data presented in chapter 3 we were able to determine the synchrotron spectra of our sources and thus to study the peak frequency and spectral index distributions with respect to the 'normal' QSO population. Also an upper limit to the synchrotron emission at mm-wavelengths can be constrained.

A recent search for High-Frequency Peakers, i.e. the youngest known radio sources with the highest turnover frequencies, shows only a very small percentage of sources with peak frequencies close to 20 GHz (Dallacasa et al. 2000) with the most extreme case at 25 GHz, leading to a formal age of some 50 years only (Orienti & Dallacasa 2008). As any upturn towards an even higher peak frequency would be visible in our spectra we can safely assume that the ex-

trapolated synchrotron emission reflects its true contribution at 250 GHz and that any observed excess emission can be attributed to the presence of cold dust. Moreover, the variability study presented in chapter 3 and 4 excludes any possible significant variability even at high frequencies over a 3 years time scale.

6.2 Observations and reduction

Up to 2012 we have observed half of the RL BAL QSO sample at mm-wavelength. We observed these targets with the IRAM-30m single dish located in Granada and for the equatorial fraction of the sources we implemented these data with the Atacama Pathfinder EXperiment (APEX) single dish, located in Chile. The two observations were planned to detect any possible power-law slope (250 GHz) and the peak (850 GHz) of the grey-body dust emission.

IRAM-30m single dish

We observed 12 sources at 250 GHz with the IRAM-30m telescope during the 2010 summer pool-session. We used the MAMBO2 117-pixels bolometer in ON/OFF mode, since all of our sources are point-like for this telescope (HPBW=11 arcsec). With average atmospheric conditions the detector can reach a noise of $\sim$1 mJy/beam in $\sim$40 min of observing time: we observed each source for this duration in order to obtain a detection or a 3-σ upper limit. Skydip, calibration and pointing scans were regularly performed during the runs and every time the observing direction in the sky significantly changed in elevation. Focus was repeated at sunrise and sunset. A standard reduction was done using the MOPSIC script provided by IRAM.

APEX

In 2010-2011 we have obtained observing time at APEX for 6 southern sources of the sample with the SABOCA bolometer (850 GHz, HPBW=8 arcsec). One source was observed also with the LABOCA bolometer, at 345 GHz (HPBW=19 arcsec). Observations were carried out in service mode, with an integration time of 1 hr per source in ON/OFF mode, in order to reach an RMS of 20 mJy/beam. A standard reduction was done using the CRUSH script from ESO.

6.3 Results

From the IRAM-30m data we obtained detections ($\geq 3\sigma$) in 3/11 cases (0756+37, 1237+47, 1406+34) and 3σ upper limits for the remaing ones. No source detection were possible from APEX observations, resulting only in upper limits for the flux densities. Results are presented in table 6.1.

Table 6.1: Results for the 14 BAL QSOs observed in the mm-band: 250 GHz flux densities from IRAM-30m, 345 and 850 GHz from APEX. We give 3-σ upper limits in case of non-detection.

Name	S_{250} (mJy)	S_{345} (mJy)	S_{850} (mJy)
0044+00	-	<260	<75
0756+37	2.0±0.5	-	-
0816+48	<1.8	-	-
0842+06	-	-	<75
0849+27	<2.4	-	-
1014+05	<3.0	-	-
1102+11	<3.0	-	-
1159+01	-	-	<51
1159+06	<6.0	-	<110
1229+09	<3.3	-	<42
1237+47	4.6±1.0	-	-
1304+13	<3.0	-	-
1327+03	<3.6	-	<60
1406+34	9.3±0.8	-	-

Best et al. (1998) presented a study of the grey-body dust emission of the radio-galaxy 3C 324 (z=1.206). They implemented radio observations in the GHz range with sub-mm data from SCUBA (JCMT, Hawaii). The continuum emission in this band is related with the dust mass by the following formula:

$$S(\nu_{obs}) = \frac{M_d(1+z)k_d(\nu_{rest})B(\nu_{rest}, T_d)}{D_L^2} \tag{6.1}$$

where S is the observed flux density, ν_{obs} and ν_{rest} are the observed and rest-frame frequencies, D_L is the luminosity distance, z is the redshift, k_d is the mass absorption coefficient, B is the black-body Planck function, and T_d is the dust grain temperature. In Fig 6.1 the resulting SED from their work is presented as an example of expected dust emission. The curve is modeled for a temperature of 30, 50 and 70 K.

Using formula 6.1, and assuming a single dust component with $M_d = 2{\times}10^8$ $M_\odot$ at a temperature of 60 K, we expected a flux density of ∼130 mJy at z = 2.3 (the median redshift of our sample). In these calculations we assumed k_d=0.067(ν_{rest}/250 GHz)$^\beta$ m^2 kg^{-1} with β=2 and a standard cosmology with H_0 = 71 km s^{-1} Mpc^{-1}, Ω_Λ = 0.73 and Ω_M = 0.27.

In Fig. 6.2 we plot the flux densities in the radio-band, already presented in chapter 2, superimposing the new data from the mm-band. Among the three cases of detected sources at 250 GHz, in two of them the emission is most probable due to the synchrotron component (1237+47, 1406+34), and the new flux density could be included in the same dataset we used for the fit in chapter 2. The same curve type used to fit the previous radio flux densities

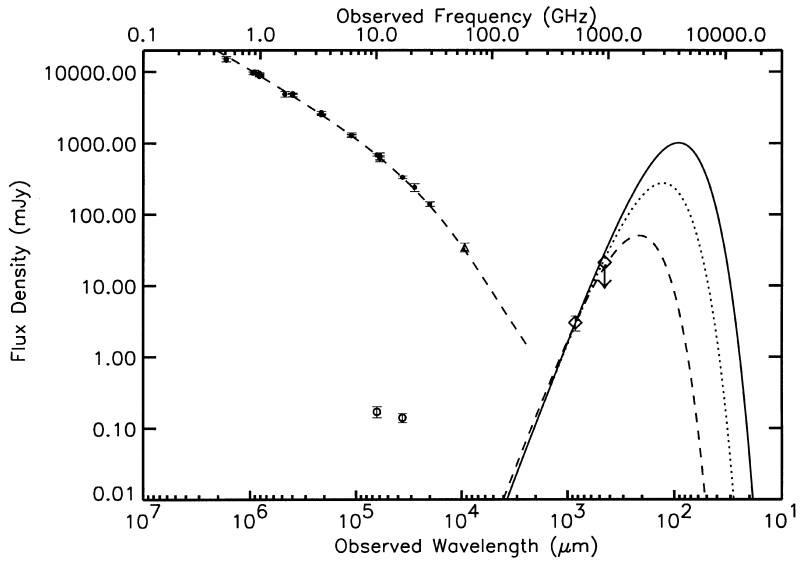

Figure 6.1: The spectral energy distribution of the radio-galaxy 3C 324 from Best et al. (1998). The open diamonds represent the SCUBA data at mm-wavelength, and the solid, dotted and dashed lines represent isothermal grey-body emission with an emissivity index β=2 for dust at temperatures of 70, 50 and 30 K respectively.

were successfully used in these two cases.

For 0756+37 we found a significant excess of emission at 250 GHz (2.0±0.5 mJy), with respect to the expected contribution of the synchrotron emission at the same frequency. In fact an upper limit of 8.4 mJy on the 43-GHz flux density determine a sufficient steepening of the synchrotron emission to give an expected flux density at 250 GHz <0.1 mJy. Thus we can consider this emission as most probable due to the grey-body dust emission, although with these data we cannot confirm this result with a measurement of the same emission at higher frequencies. Thanks to future observations of the peak emission it will be possible to derive the dust mass of this object.

The upper limit derived from non-detections were not included in the fits datasets, only resulting in constraints for the dust emission. Given that an expected peak flux density of ∼130 mJy would be above the upper limits, and moreover would be reflected into an emission of ∼10 mJy at 250 GHz, we can reasonably conclude that no other of the observed sources contain a dust component with the previously discussed characteristics ($M_d = 2{\times}10^8 M_\odot$ and $T = 60$ K). A dust component with the same mass assumed before, but at a temperature T=30 K, could still result in a flux density of ∼27 mJy at 850 GHz, and ∼2 mJy at 250 GHz. Both these values are below the upper limits from our observations. Also mass play a role, since the flux density is directly proportional to it: a mass of only $10^8 M_\odot$ would reflect in half the flux density expected from the previous calculation.

Omont et al. (2003) presented the results of 250-GHz observations of 35 optically luminous RQ QSOs ($M_B < -27.0$), with a redshift 1.8<z<2.8, performed with the MAMBO bolometer. They found that 26±9% of the sources present an emission at that frequency. They obtained an RMS similar to our observations, so we can compare our results with this percentage: only 1 out of 14 (7±7%) of our sources presents dust emission, a substantially smaller fraction than the one found by Omont et al. (2003). Observations of the remaining 11 sources from our sample could allow us to find other cases of dust-emission, giving a final fraction of dusty sources more similar to the results from Omont et al. (2003). Despite the small statistics we can conclude that RL BAL QSOs do not show a dust-rich fraction of objects larger than the QSO population.

6.4 Conclusions

We performed observations in the mm-band of 14 RL BAL QSOs from our sample. The radio spectra were already known, so the contribution of the synchrotron emission can be well determined from the results of chapter 2. The conclusions are the following:

- Only 1 out of 14 sources (∼7%) presents a clear contribution at 250 GHz from the dust grey-body emission. In the other cases 3σ upper limits have been derived.
- Comparing our results with the fraction of dust-rich QSOs found by Omont et al. (2003), resulting in a percentage of ∼26%, we found that RL BAL QSOs does not present a larger fraction of dust-rich objects with respect to the QSO population.
- Since the amount of dust can be connected to star-formation and thus to the age of the host-galaxy, this results suggest that RL BAL QSOs are not a younger population of QSOs.

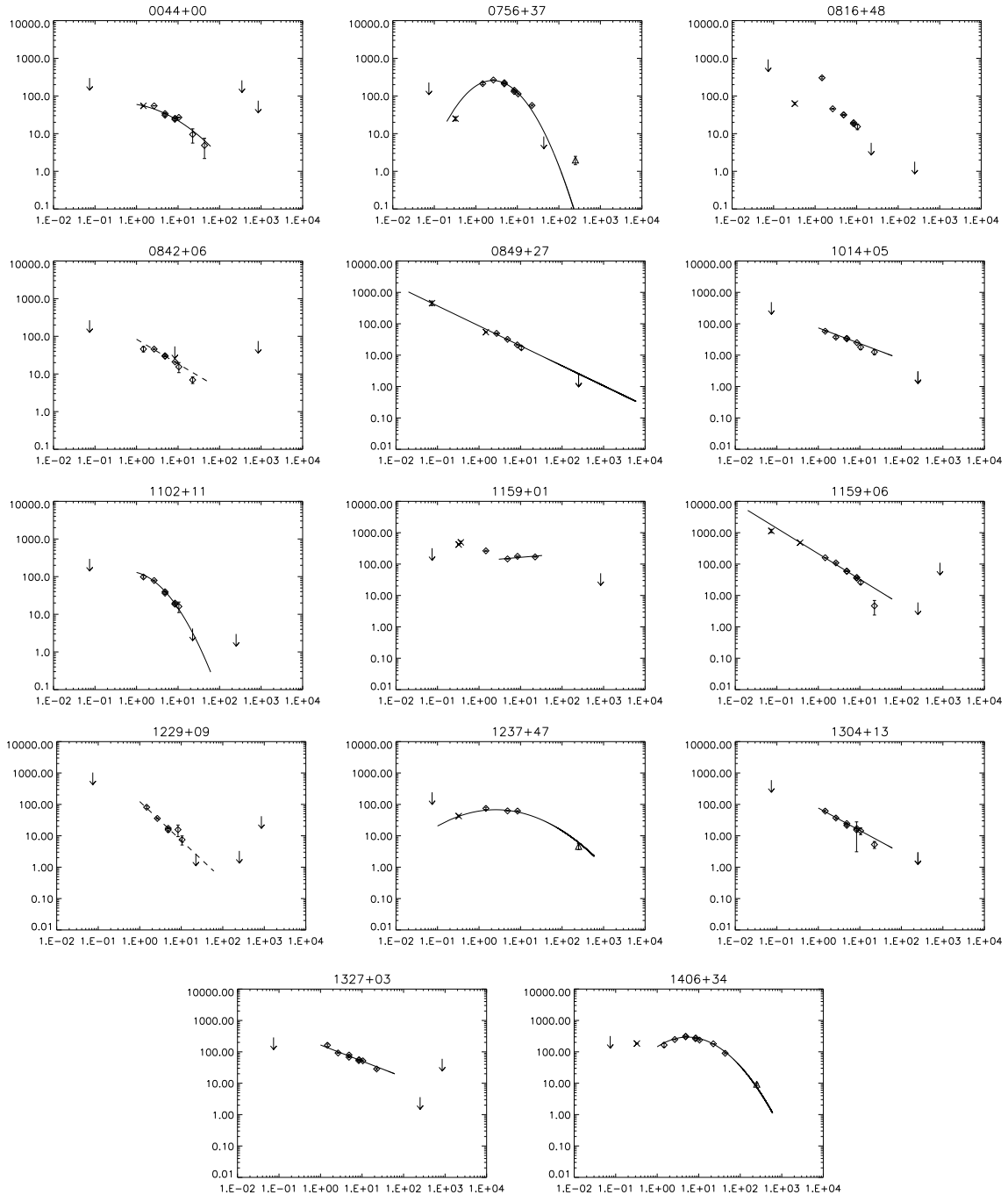

Figure 6.2: Spectra of 14 BAL QSOs observed in the mm-band (x-axis: GHz; y-axis: mJy). 250 GHz flux densities from IRAM-30m, 345 and 850 GHz from APEX (triangles). Flux densities at lower frequencies are taken from chapter 2 (crosses, $\nu < 1.4$ GHz: literature; rhombi, $\nu \geq 1.4$ GHz: our observational campaign).

Chapter 7

The central kpc: Near-Infrared spectroscopy

7.1 Introduction

In the Near Infrared (NIR) domain, with a redshift between ∼2.5 and ∼3.5, it is possible to observe the UV-Optical part of the QSO spectrum. In this range the Broad Absorption Line can be observed at the blue-side of the Mg II emission line. The C IV emission line usually presents a stronger BAL but falls in the optical window. We collected low-resolution NIR spectra (0.9 – 2.4 microns) of a sample of optically-bright 21 Radio-Loud BAL quasars, and a matched comparison sample of the 23 optically-bright Radio-Quiet BAL quasars (r<19.5) aiming at investigating the possible differences introduced by radio-loudness: Becker et al. (2001) estimated that BAL QSOs are four times less common amongst quasars with $\log R_* > 2$ than amongst quasars with $\log R_* < 1$ (where R_* is the k-corrected ratio $S_{5\mathrm{GHz}}/S_B$). Hewett & Foltz (2003) noted that optically-bright BAL quasars are half as likely as non-BAL QSOs to have $S_{1.4\mathrm{GHz}} > 1$ mJy, leaving the reason for the dependence of the BAL QSO fraction on R_* still unveiled.

From the analysis of the principal lines in our range (Mg II, Hβ) and of the continuum emission it is possible to study some characteristics of the QSO:

- FWHM of Mg II and Hβ can be indicative of the central BH mass, according to the scaling relations given by Vestergaard et al. (2006) and Vestergaard & Osmer (2009)

- The Eddington ratio of the central BH can be estimated from the luminosity at 5100 A, like sugggested by Kaspi et al. (2000).

- Also the size of the Broad Line Region can be related to the luminosity at 5100 A (Kaspi et al. 2000, 2005; Bentz et al. 2006).

7.2 The optically-bright sample

The spectroscopic study presented in this chapter has been carried out using a third sample of BAL QSOs, different from the RBQ sample by Montenegro-Montes et al. (2008a) studied in chapter 4, and from the main sample used for this thesis, presented in chapter 2.

We built a sample composed of the 21 optically brightest Radio-Loud BAL QSOs and a comparison sample composed of the 23 optically brightest Radio-Quiet BAL QSOs from the SDSS DR4. As a first step, we selected all the QSOs from the SDSS DR4 with a redshift z>2.5, in order to observe the main optical emission lines in the chosen NIR window. Then, we set an additional upper limit of r<19.5 to the magnitude in r-band. All the spectra of the objects satisfying these criteria were visually inspected, and classified as BAL or non-BAL QSOs: this results in 209 BAL QSOs.

The resulting list of BAL QSOs was cross-correlated with the FIRST survey, in order to divide them into Radio-Loud (RL, $S_{1.4\mathrm{GHz}} > 0$) and Radio-Quiet (RQ, $S_{1.4\mathrm{GHz}} = 0$). From each of these two sub-sample, we selected the 21 RL BAL QSOs and the 23 RQ BAL QSOs with the brightest luminosity in r-band.

The final list of RL and RQ BAL QSOs studied here is presented in Tab. 7.1 and 7.2.

7.3 NIR observations and data reduction

These observations were obtained with the Near Infrared Camera Spectrograph (NICS) at the 3.58m Telescopio Nazionale Galileo (TNG). NICS (Baffa et al. 2001) offers a unique, high sensitivity and low resolution observing mode which uses an Amici Prism as a dispersing element (Oliva 2003). In this mode it is possible to get a spectrum from 0.8 to 2.4 microns in a single exposure with a very high throughput. Spectral resolution with 1" slit (our default setup) is R$\sim$50 or $\sim$6000 Km/s. This observing mode is appropriate to study typical BAL QSOs with broad (>4000Km/s) emission lines and absorption systems.

Observations were carried out in five observing runs during the 2008 ITP (International Time La Palma): Jan 25, Mar14, Mar15, Jun25 and Jun26. A total of 44 QSOs were observed with a non-repetitive "ABBA" nodding pattern along the slit; typical integration time was 24min per target. Data reduction was performed with a semi-automatic pipeline. This takes as input the QSO spectrum, that of a telluric standard star (FV-GV) taken at similar airmass (to remove the telluric absorption features) and a look-up table for the wavelength calibration.

The atmospheric transparency is a free parameter that is changed manually in order to take into account any variation of the sky transparency along the night. This allows the atmospheric residuals in the final spectrum to be minimized. Also, small shifts in the wavelength calibration solution can be

Table 7.1: Sample of 21 Radio-Loud BAL QSOs studied in this work. Column 4 is the redshift as measured from the SDSS.

Name	RA (J2000)	DEC (J2000)	z	FIRST (mJy)	Obs. Date
(1)	(2)	(3)	(4)	(5)	(6)
0844+05	08 44 01.96	+05 03 57.9	3.34	7.2	25/01/2008
1106+57	11 06 57.18	+57 51 22.9	2.72	34.5	25/01/2008
1110+42	11 10 38.46	+42 17 15.7	2.57	2.8	14/03/2008
1137+54	11 37 22.84	+54 41 55.3	2.75	2.5	14/03/2008
1144+09	11 44 36.65	+09 59 04.9	3.15	12.8	15/03/2008
1152+04	11 52 05.41	+04 29 52.9	3.35	1.9	15/03/2008
1159+41	11 59 47.10	+41 36 59.1	2.94	2.5	15/03/2008
1214+51	12 14 20.10	+51 49 24.8	2.63	3.7	15/03/2008
1228−01	12 28 48.21	−01 04 14.5	2.65	29.4	14/03/2008
1236+45	12 36 51.28	+45 33 34.5	2.56	1.9	15/03/2008
1307+04	13 07 56.73	+04 22 15.5	3.02	14.3	15/03/2008
1327+03	13 27 03.22	+03 13 11.3	2.82	60.7	14/03/2008
1359+47	13 59 09.93	+47 08 26.5	2.53	2.2	26/06/2008
1413+42	14 13 34.38	+42 12 01.7	2.81	17.8	26/06/2008
1422+44	14 22 43.02	+44 17 21.5	3.54	1.2	26/06/2008
1426+44	14 26 10.59	+44 11 24.0	2.67	6.8	15/03/2008
1459+42	14 59 10.14	+42 52 13.2	2.96	12.8	14/03/2008
1516+43	15 16 01.51	+43 09 31.5	2.63	1.3	26/06/2008
1624+37	16 24 53.48	+37 58 06.6	3.38	56.1	25/06/2008
1625+48	16 25 59.90	+48 58 17.5	2.72	25.3	25/06/2008
1637+32	16 37 50.37	+32 23 13.8	2.99	5.1	26/06/2008

Table 7.2: Sample of 23 Radio-Quiet BAL QSOs studied in this work. Column 4 is the redshift as measured from the SDSS.

Name	RA (J2000)	DEC (J2000)	z	Obs. Date
(1)	(2)	(3)	(4)	(5)
0316+00	03 16 09.84	+00 40 43.2	2.92	25/01/2008
0735+37	07 35 35.45	+37 44 50.4	2.75	15/03/2008
0746+30	07 46 28.72	+30 14 19.0	3.11	25/01/2008
0800+44	08 00 06.32	+44 35 55.6	2.50	15/03/2008
0913+44	09 13 07.83	+44 20 14.4	2.93	25/01/2008
0958+36	09 58 58.14	+36 23 18.9	2.67	14/03/2008
1020+10	10 20 09.99	+10 40 02.8	3.16	25/01/2008
1023+51	10 23 25.32	+51 42 51.0	3.44	14/03/2008
1024+58	10 24 24.58	+58 57 56.1	2.95	14/03/2008
1059+12	10 59 04.69	+12 10 24.0	2.50	15/03/2008
1319+53	13 19 12.41	+53 47 20.6	3.09	14/03/2008
1347+46	13 47 22.84	+46 54 28.6	2.93	15/03/2008
1400+41	14 00 06.89	+41 21 42.6	2.76	15/03/2008
1407+40	14 07 45.50	+40 37 02.3	3.2	25/06/2008
1425+54	14 25 43.32	+54 06 19.4	3.24	14/03/2008
1503+36	15 03 32.18	+36 41 18.0	3.26	26/06/2008
1525+51	15 25 53.90	+51 36 49.3	2.88	25/06/2008
1537+58	15 37 15.74	+58 29 33.8	2.59	25/06/2008
1559+48	15 59 12.35	+48 28 20.0	3.42	25/06/2008
1612+38	16 12 50.25	+38 40 30.8	2.92	25/06/2008
1638+22	16 38 20.04	+22 06 20.5	3.08	26/06/2008
1641+38	16 41 51.84	+38 54 34.2	3.77	26/06/2008
1642+44	16 42 19.89	+44 51 24.0	2.88	25/06/2008

Table 7.3: Data from literature for the Radio-Loud (first 21 objects) and Radio-Quiet (second 23) BAL QSO samples: magnitudes in g, r and i bands from the SDSS DR4, magnitudes in J, H and K bands from the 2MASS Point Source Catalogue.

Name	g	r	i	J	H	K
	(mag)	(mag)	(mag)	(mag)	(mag)	(mag)
(1)	(2)	(3)	(4)	(5)	(6)	(6)
0844+05	19.09	18.19	17.40	15.386	14.928	14.19
1106+57	18.63	18.49	18.36	17.087	15.84	15.702
1110+42	19.56	18.70	18.26	16.073	15.406	14.562
1137+54	19.12	18.95	18.75	-	-	-
1144+09	19.15	18.66	18.49	16.674	15.787	15.485
1152+04	19.72	19.08	18.88	-	-	-
1159+41	19.20	18.97	18.83	-	-	-
1214+51	19.69	18.88	18.55	16.843	16.371	15.945
1228−01	18.63	18.49	18.27	16.363	15.385	14.833
1236+45	18.35	18.11	17.90	16.418	15.788	14.975
1307+04	18.63	18.39	18.04	15.923	15.881	15.101
1327+03	19.69	19.26	18.89	16.748	15.577	15.062
1359+47	19.70	19.09	18.90	-	-	-
1413+42	19.30	18.98	18.69	16.614	16.231	15.54
1422+44	19.7	18.43	17.89	15.81	15.207	14.463
1426+44	19.33	18.98	18.73	-	-	-
1459+42	18.58	18.40	18.32	16.705	16.295	15.844
1516+43	19.29	18.79	18.47	16.389	15.887	15.241
1624+37	19.42	18.74	18.48	16.89	16.287	15.571
1625+48	18.52	18.31	18.02	16.626	15.989	15.06
1637+32	19.43	19.15	18.92	-	-	-
0316+00	19.23	18.98	18.8	-	-	-
0735+37	19.04	18.89	18.67	-	-	-
0746+30	19.62	18.81	17.99	16.059	15.541	15.152
0800+44	19.59	18.95	18.7	16.602	15.764	15.266
0913+44	18.88	18.34	17.88	16.001	15.455	14.887
0958+36	18.3	18.15	17.94	16.201	15.044	14.645
1020+10	18.57	18.14	18.02	16.634	15.49	15.322
1023+51	18.82	18.09	17.95	16.296	15.841	15.367
1024+58	18.27	18.1	17.96	15.97	15.62	15.078
1059+12	18.07	17.85	17.78	16.246	15.351	15.044
1319+53	18.65	18.26	18.09	16.096	15.646	15.289
1347+46	18.88	18.3	17.93	16.343	15.735	15.156
1400+41	18.73	18.39	18.08	16.434	15.907	15.45
1407+40	19.55	18.82	18.09	15.967	15.397	14.631
1425+54	18.53	18.04	17.78	16.061	15.501	15.244
1503+36	18.96	18.22	17.73	15.872	15.667	15.01
1525+51	17.41	17.19	16.95	15.138	14.492	14.019
1537+58	18.08	17.61	17.4	15.883	15.095	14.706
1559+48	18.80	18.10	18.00	16.457	16.062	15.505
1612+38	18.57	18.26	17.91	16.122	15.648	14.989
1638+22	18.9	18.63	18.59	-	-	-
1641+38	20.78	18.88	18.88	16.797	16.177	15.333
1642+44	18.62	18.24	17.75	16.017	15.514	14.91

introduced at this point of the process to perfectly match the broad telluric absorptions features of the standard and the QSO. Absolute flux calibration was obtained by scaling the spectrophotometric flux of the QSO to that of the telluric standard at H-band. To improve this calibration we renormalized the spectra comparing with the flux density of the SDSS at 9000 Å, the scaling factor varying in a range of ∼0.3 to ∼3.

7.4 Results

We analysed the spectra using the SPLAT[1] package from the European Virtual Observatory. We fitted the continuum using a second or third grade polynomial function, and the emission lines using a Gaussian with free parameters after performing the continuum subtraction. Standard UV and Optical line identifiers were used.

Our primary target was to extract the FWHM of the Mg II and Hβ emission lines, in order to estimate the central black hole masses of the two samples. In the wavelength range from 0.8 to 2.4 microns there are two critical intervals because of very low atmospheric transmittance: 1.35 - 1.44 microns and 1.81 - 1.94 microns. When one of the lines fell in these ranges it was not possible to perform the fit, because of superposition with the atmospheric features. The measured FWHM are presented in Tab. 7.4 and 7.5, together with the continuum luminosity at 3000 and 5100 Å. Mg II can present a double peaked emission: in this case we performed a double Gaussian profile fit and combined the two FWHM via quadratic sum.

In the following we will show the methods we adopted and the results we obtained following the various relations present in literature, useful to infer different properties of the RL and RQ BAL QSO samples.

7.4.1 Black-hole mass estimation

As a first step we tried to infer different properties of the two groups of BAL QSOs through the estimation of the central black hole mass. If they would be intrinsically different group of objects, different physical properties could be present, and the central black hole mass can be an important variable for the dynamics of the central environment of the AGN.

In literature various relations are present to infer the mass of the central BH from single epoch spectra: these are empirical relations, derived from Reverberation Mapping (RM, see Peterson 2011 for a review), related to the FWHM of the strong UV emission lines in the optical-UV domain (C IV, Mg II, Hβ) and with the continuum luminosity at a given wavelength. These relations are applicable with the caveats that no absorption is present in the line profile, and a good signal to noise (S/N) ratio is available from measurements, otherwise the low-precision FWHM measurement can introduce errors or even systematic

[1] http://www.euro-vo.org/pub/

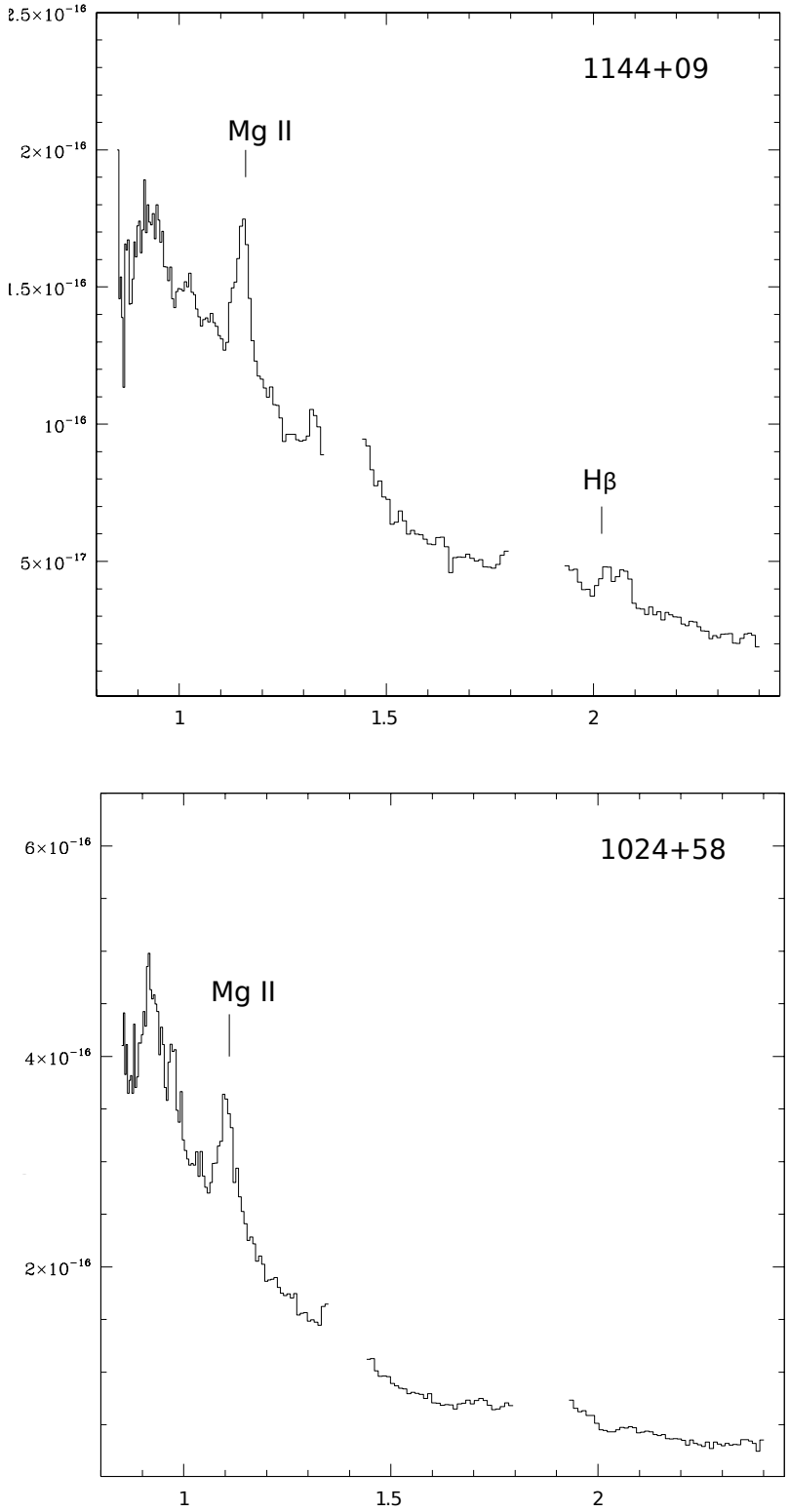

Figure 7.1: Spectra of a RL (top panel) and a RQ (bottom panel) BAL QSO from our observations. Regions were atmospheric transmittance become critical have been blanked (1.35 - 1.44 microns and 1.81 - 1.94 microns, see Sec. 7.4).

biases in the final estimate. For this reason (and also because at our redshift range only Mg II and Hβ are present in the NIR window) we decided to discard the C IV line from this kind of analysis, since it presents the BALs feature, and avoid the use of SDSS data for that line.

Another important condition to perform a good estimate through scaling relations, is that the chosen formula are on the same mass-scale: nowadays the only sets of relations for Hβ and Mg II with this property are those presented by Vestergaard et al. (2006) and Vestergaard & Osmer (2009) respectively. Thus, the two relations we used for our estimate are the following:

$$M_{\rm BH}\ [M_\odot] = 10^{6.86} \left[\frac{\rm FWHM(MgII)}{1000\ km\ s^{-1}}\right]^2 \left[\frac{\lambda L_\lambda(3000\,\text{Å})}{10^{44}\rm erg\ s^{-1}}\right]^{0.50} \tag{7.1}$$

from Vestergaard & Osmer (2009), where $L_\lambda(3000\,\text{Å})$ is the rest-frame luminosity at 3000Å. This relation is given with a 1-σ scatter of 0.55 dex.

The second estimator we use is derived by Vestergaard et al. (2006), and related with the Hβ line:

$$M_{\rm BH}\ [M_\odot] = 10^{6.91} \left[\frac{\rm FWHM(H\beta)}{1000\ km\ s^{-1}}\right]^2 \left[\frac{\lambda L_\lambda(5100\,\text{Å})}{10^{44}\rm erg\ s^{-1}}\right]^{0.50} \tag{7.2}$$

where $L_\lambda(5100\,\text{Å})$ is the rest-frame luminosity at 5100Å. This relation is given with a 1-σ scatter of $\pm$0.43 dex.

These relations take advantage of the most recent updated analysis of the reverberation mapping sample (Peterson et al. 2004) and of the improved radius-luminosity (R-L) relations between the BLR size and continuum luminosity (Kaspi et al. 2005; Bentz et al. 2006). Results are presented in Tables 7.4 and 7.5, together with the FWHM of the lines as extracted from the spectra and the continuum luminosity. We applied the K-correction both to the continuum and the FWHM.

Masses can span in more than one order of magnitudes for both samples and for both the estimators used. The average values obtained for the two distributions are $10^{10.02} M_\odot$ ($\sigma = 10^{0.40}$) and $10^{9.91} M_\odot$ ($\sigma = 10^{0.56}$) respectively for RL and RQ BAL QSOs. Estimates from the Hβ emission line give a similar range of masses, with an average value of $10^{9.66} M_\odot$ ($\sigma = 10^{0.23}$) for RL and $10^{9.68} M_\odot$ ($\sigma = 10^{0.55}$) for RQ objects. We do not see any significative difference between the BH masses estimated for RL and RQ BAL QSOs.

It is worth noting that the scatter in both relations 7.1 and 7.2 of respectively 0.55 dex and 0.43 dex is an important constraint when comparing masses. Considering this large error, a discrepancy of at least 3-σ between the two means would be necessary to indicate an intrinsic difference between the distributions of BH masses for the two groups of BAL QSOs.

7.4.2 The Eddington ratio

From the continuum luminosity we can derive another quantity useful to test the differences between the two group of BAL QSOs: the Eddington ratio.

Table 7.4: Measured quantities (rest-frame) for the sample of 21 RL BAL QSOs

Name	FWHM Mg II (km/s)	FWHM Hβ (km/s)	log(λL_{3000}) (erg/s)	log(λL_{5100}) (erg/s)	log(M_{BH}^{MgII}) ($M_\odot$)	log($M_{BH}^{H\beta}$) ($M_\odot$)	BLR radius (light-days)	L_{Bol}/L_{Edd}
(1)	(2)	(3)	(4)	(5)	(6)	(7)	(8)	(9)
0844+05	9110±1380	3610±1380	47.42	47.35	10.48±0.57	9.54±0.54	1060	6.18
1106+57	-	-	46.70	46.48	-	-	389	2.27
1110+42	13530±1680	-	46.80	46.36	10.49±0.56	-	336	1.96
1137+54	6400±1600	-	46.57	46.05	9.70±0.59	-	235	1.37
1144+09	9600±1440	5000±1440	46.83	46.48	10.18±0.57	9.55±0.50	389	2.27
1152+04	5350±1380	-	46.55	46.28	9.53±0.59	-	309	1.80
1159+41	5450±1520	-	46.59	46.19	9.55±0.60	-	279	1.62
1214+51	7780±1650	4150±1650	46.78	46.55	9.94±0.58	9.39±0.55	419	2.44
1228−01	7410±1640	9290±1640	46.89	46.35	10.00±0.58	9.99±0.46	335	1.95
1236+45	12970±1680	6667±1680	46.98	46.72	10.51±0.56	9.83±0.48	513	2.99
1307+04	7990±1490	-	47.00	46.69	10.05±0.57	-	491	2.86
1327+03	9860±1570	-	46.54	46.19	10.04±0.57	-	279	1.62
1359+47	4250±1690	-	46.50	46.23	9.32±0.65	-	291	1.70
1413+42	5960±1570	-	46.72	46.45	9.62±0.60	-	374	2.18
1422+44	10550±1320	-	47.31	47.22	10.51±0.56	-	911	5.31
1426+44	-	7030±1630	46.69	46.62	-	9.91±0.47	455	2.65
1459+42	7520±1510	-	46.60	46.05	9.85±0.58	-	236	1.38
1516+43	5830±1650	4340±1650	46.77	46.56	9.64±0.60	9.39±0.54	426	2.48
1624+37	10850±1370	-	46.85	46.68	10.29±0.56	-	486	2.83
1625+48	15080±1610	-	46.91	46.67	10.67±0.56	-	484	2.82
1637+32	-	-	46.65	46.52	-	-	405	2.36

Table 7.5: Measured quantities (rest-frame) for the sample of 23 RQ BAL QSOs

Name	FWHM Mg II (km/s)	FWHM Hβ (km/s)	$\log(\lambda L_{3000})$ (erg/s)	$\log(\lambda L_{5100})$ (erg/s)	$\log(M_{BH}^{MgII})$ ($M_\odot$)	$\log(M_{BH}^{H\beta})$ ($M_\odot$)	BLR radius (light-days)	L_{Bol}/L_{Edd}
(1)	(2)	(3)	(4)	(5)	(6)	(7)	(8)	(9)
0316+00	-	-	46.54	46.18	-	-	274	1.60
0735+37	3510±1600	-	46.58	46.24	9.11±0.68	-	294	1.71
0746+30	-	-	47.01	46.77	-	-	543	3.16
0800+44	5030±1710	8910±1710	46.62	46.37	9.57±0.62	9.90±0.46	342	2.00
0913+44	6730±1520	1170±1520	47.06	46.90	9.94±0.58	8.36±1.21	630	3.67
0958+36	-	-	46.88	46.57	-	-	432	2.52
1020+10	-	-	46.90	46.74	-	-	522	3.04
1023+51	-	-	46.96	46.53	-	-	410	2.39
1024+58	12130±1520	-	46.90	46.40	10.47±0.56	-	354	2.06
1059+12	9090±1710	8750±1710	46.95	46.63	10.24±0.57	10.03±0.46	460	2.68
1319+53	9090±1470	-	46.74	46.34	10.14±0.57	-	331	1.93
1347+46	3120±1520	6380±1520	46.99	46.74	9.31±0.69	9.84±0.48	524	3.05
1400+41	-	-	46.88	46.55	-	-	420	2.45
1407+40	9270±1430	6720±1430	47.12	46.96	10.33±0.57	9.95±0.47	674	3.93
1425+54	12080±1410	-	46.93	46.50	10.48±0.56	-	397	2.32
1503+36	4610±1410	5070±1410	47.13	46.81	9.63 ±0.61	9.71±0.49	568	3.31
1525+51	8140±1540	-	47.41	47.22	10.37±0.57	-	909	5.30
1537+58	1360±1670	7740±1670	47.06	46.79	8.39 ±1.20	9.99±0.47	552	3.22
1559+48	6620±1350	-	46.99	46.59	9.91 ±0.58	-	441	2.57
1612+38	10470±1530	-	47.03	46.73	10.37±0.56	-	518	3.02
1638+22	-	-	46.70	46.31	-	-	317	1.85
1641+38	7280±1250	-	47.01	46.87	10.05±0.57	-	608	3.54
1642+44	9200±1540	-	47.05	46.77	10.29±0.57	-	544	3.17

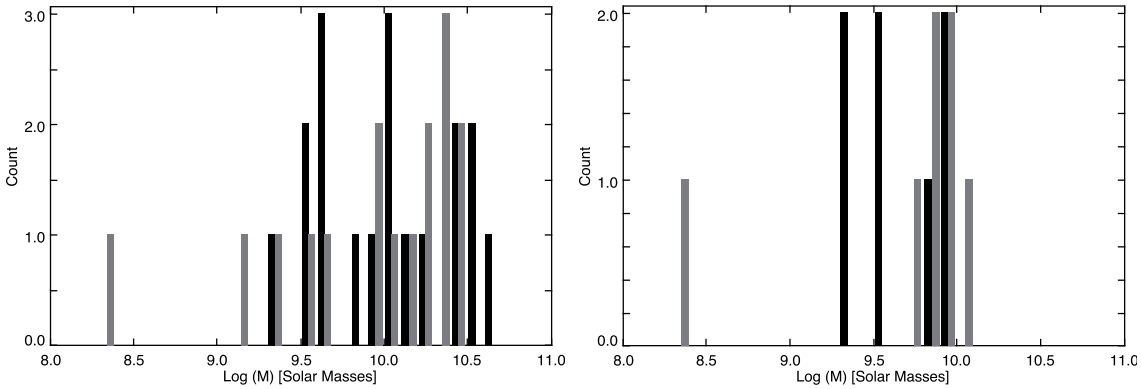

Figure 7.2: Distributions of the BH masses for the RL (black) and RQ (grey) QSO samples, estimated from the Mg II (left) and Hβ (right) lines.

Boroson et al. (2002) explain the observable spectral characteristics of QSOs as driven from two principal quantities: the Eddington ratio (L_{Edd}) and the accretion rate ($\dot{M}$). In his diagram BAL QSOs occupy a corner, being peculiar objects with both high $\dot{M}$ and L_{Edd}. From our data it is possible to study the distribution of this last quantity for RL and RQ BAL QSOs.

Kaspi et al. (2000) derived the following formula for the calculation of the Eddington ratio, roughly estimating the bolometric luminosity as $L_{bol} \approx 9\lambda L_{\lambda}(5100\text{Å})$:

$$\frac{L_{bol}}{L_{Edd}} \approx 0.13 \left(\frac{\lambda L_{\lambda}(5100\,\text{Å})}{10^{44}\,\text{ergs}\,\text{s}^{-1}} \right)^{0.5} \tag{7.3}$$

The Eddington ratios for the RL and RQ BAL QSOs are in Table 7.4 and 7.5. All the objects (both RL and RQ) results to have super-Eddington luminosities, with a mean value of respectively 2.52 and 2.80. This can be due to selection effect, since only the most luminous BAL QSOs in the optical band were considered for our sample, implying an higher luminosity also at NIR wavelengths. No significant difference is present between the two samples. We extend this study to an unbiased sample of BAL QSOs in Sec. 7.5.2.

7.4.3 Broad Line Region radius

Vestergaard et al. (2006) derived the relation 7.2 starting from the Broad Line Region (BLR) radius, obtained from RM, and from the velocity of the Hβ gas approximated from the FWHM of its broad emission line. It has been found that the BLR region is correlated to the continuum luminosity (Kaspi et al. 2000, 2005). Bentz et al. (2006) updated these results taking into account the contribution of the host galaxy starlight. This last version is consistent with the method of Vestergaard et al. (2006), and is the following:

$$R_{BLR} = A \cdot \left[\frac{\lambda L_{\lambda}(5100)}{10^{44}\text{erg}\ \text{s}^{-1}} \right]^{0.5} \ \text{lt} - \text{days} \tag{7.4}$$

where the coefficient A is the scaling factor. The main difference with respect to the formula proposed by Kaspi et al. (2005) is the value of the exponent of the luminosity, given as 0.69±0.5 in that work, and corresponding to the slope of the correlation in logarithmic scale. The value of A, as the value of the slope, depends on the method used to interpolate data (BCES or FITEXY, see Bentz et al. 2006 for further details): both authors use the two methods and compare the values obtained for the scaling factor. In this work we decided to use the mean value proposed by Kaspi et al. (2005) for the scaling factor (A=22.3±2.1), and apply the correction provided by Bentz et al. (2006) for the slope.

Also in this case no clear differences are present between RL and RQ BAL QSOs: we have obtained a mean BLR radius of 481 light-days for the first group (σ=142) and 433 for the second (σ=198), suggesting similar environments.

7.5 Results from the SDSS DR7 Quasar Catalogue

Shen et al. (2011) provides a catalogue of Quasars properties from the SDSS DR7 (Schneider et al. 2010), including BAL classification, Radio-Loudness parameter R, defined as $R = S_{5\mathrm{GHz}}/S_B$ (Stocke et al. 1992), and virial BH mass estimates based on different emission lines. With these data it is possible to study the spectroscopic properties of RL *vs* RQ BAL QSOs and BAL QSOs *vs* non-BAL QSOs with a better statistics. Since our combined samples of RL and RQ BAL QSOs are composed only from the brightest object in r band, we preferred not to compare with the catalogue BAL samples, in order to avoid biases due to the selection process.

Among the 105783 QSOs included in the catalogue, 6214 (∼6%) are classified as BAL QSOs and the remaining 99569 (∼94%) as non-BAL QSOs or objects with no sufficient wavelength coverage for BAL classification purposes; a fraction of BAL QSOs could still be hidden in this sub-sample (∼8%, restoring the ∼15% BAL fraction known from literature, see chapter 1). Among these BAL QSOs only 139 (∼2%) are RL while 5679 are RQ (∼91%), considering as RL all the BAL QSOs with $\log R > 2$ and RQ all the objects with $\log R < 0.5$ (Stocke et al. 1992). The remaining 7% has $0.5 < \log R < 2$. These percentages confirm the rarity of RL BAL QSOs, since in the whole catalogue 4819 objects (5%) are RL QSOs, more than two times the percentage found among BAL QSOs only.

7.5.1 Black Hole virial masses

The catalogue estimated masses are derived from UV and optical emission lines (C IV, Mg II, Hβ). They define a *fiducial* mass using different estimators for different redshift ranges (see the paper for further details). We used these estimates to extend the statistical study done with our NIR spectra to a bigger

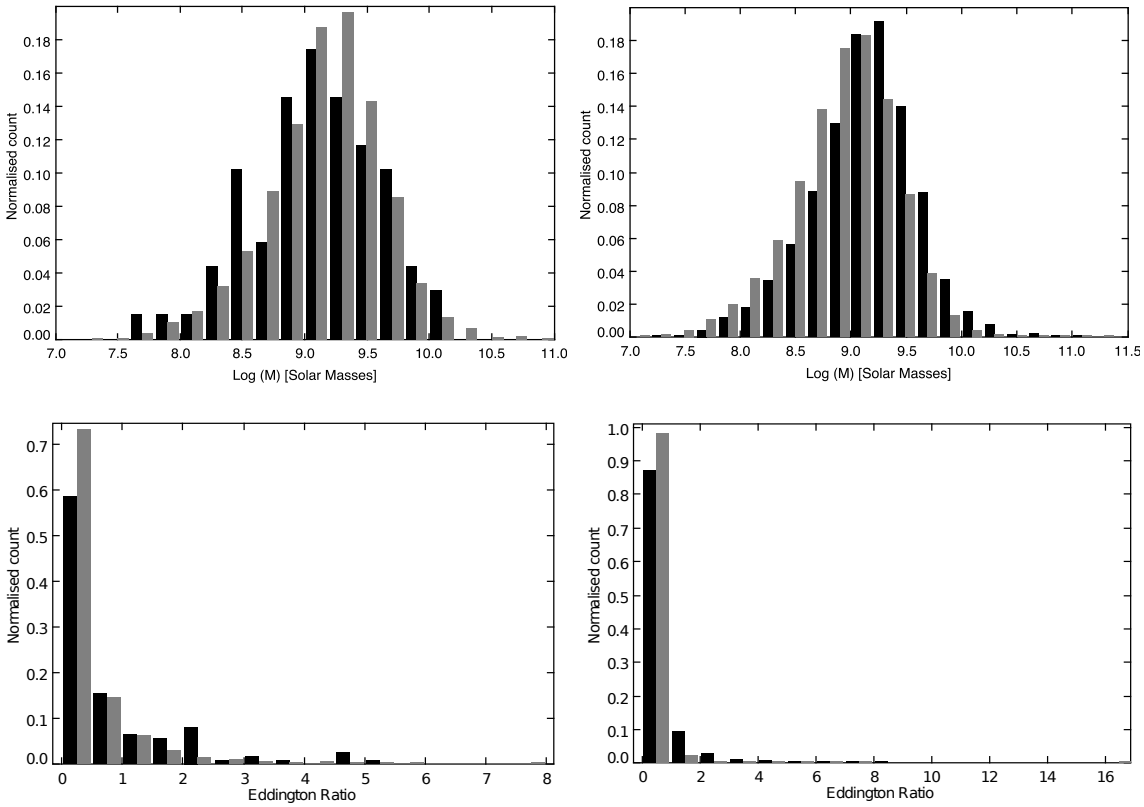

Figure 7.3: Top panels: normalised distributions of the BH masses for the RL (black) *vs* RQ (grey) BAL QSOs (left panel) and BAL (black) *vs* non-BAL (grey) QSOs (right panel), drawn from the SDSS DR7 QSO catalogue. Bottom panels: normalised distributions of the Eddington ratio for the RL (black) *vs* RQ (grey) BAL QSOs (left panel) and BAL (black) *vs* non-BAL (grey) QSOs (right panel), drawn from the SDSS DR7 QSO catalogue.

sample. In some cases the spectra did not allow to assign a fiducial mass: this reduces the number of RL and RQ BAL QSOs considered respectively to 69 and 3362 , while the number of BAL and non-BAL QSOs is reduced respectively to 3650 and 79650. Also the redshift range is reduced to a maximum value of 2.5 for both BAL and non-BAL QSOs.

Looking at the normalised distributions (Fig. 7.3) we do not find any significant difference in RL *vs* RQ BAL QSOs or in BAL *vs* non-BAL QSOs: the means for the first pair of distributions are 9.11 dex (σ=0.51) and 9.15 dex (σ=0.45), for the second pair we obtain 9.14 dex (σ=0.47) and 8.93 dex (σ=0.46), thus we can conclude the hypothesis that the two mean values are derived from samples with different properties can be rejected in both cases. This confirm the previous results from our NIR observations. The slightly smaller values for the mean BH mass of RL and RQ BAL QSOs are due to selection effects, as explained before, since we observed only the optically brightest objects.

7.5.2 Super-Eddington objects fraction

The catalogue provides also the Eddington ratios as calculated from the BH fiducial mass, thus only for some objects this quantity is present. We compared the Eddington ratio distributions for RL *vs* RQ BAL QSOs and BAL *vs* non-BAL QSOs (see Fig. 7.3): among BAL QSOs there is a significant higher fraction of objects with Edd>1 than among non-BAL QSOs (13% *vs* 2%). An analogous result has been found for RL *vs* RQ BAL QSOs (26% *vs* 13%).

BAL QSOs in general show a luminosity exceeding the Eddington limit, suggesting a more turbulent accretion activity, leading to a thick accretion disk. In this frame, subject of several studies in the past decades, the outflows could be generated from the accretion disk with an high rate, and reach high velocities, increasing the probability to see a BAL in the UV spectrum. The super-Eddington luminosity implies an high accretion rate: a rich environment could favour the presence of BAL QSOs, as seems to suggest a recent study about the fraction of BAL QSOs among high-redshift QSOs (Allen et al. 2011).

7.6 Conclusions

In this last chapter we investigated the spectral properties of RL *vs* RQ QSOs in the NIR domain, measuring the main emission lines and continuum, to estimate some physical quantities related to the central kpc of these objects. Our sample is composed only from optical bright BAL QSOs (r<19.5), so a comparison with other samples should consider this. We also used the last edition of the QSO catalogue from the SDSS DR7, to improve our statistics, and compare also BAL with non-BAL QSOs.

The results can be summarised as follows:

- the central BH masses does not show significant differences between RL and RQ BAL QSOs. The same analysis has been performed for the QSO catalogue, resulting in no significant differences neither for RL *vs* RQ BAL QSOs nor for BAL *vs* non-BAL QSOs. This exclude possible differences due to the BH mass to be at the origin of the rarity of RL BAL QSOs.

- The Eddington ratios derived from our samples of RL and RQ BAL QSOs are comparable and >1 for all the objects. This can be due to selection effects, since only the optically bright BAL QSOs have been included in our sample. A more interesting view have been obtained from the QSO catalogue: a significant difference in the fraction of super-Eddington objects is present between BAL (13%) and non-BAL (2%) QSOs, and between RL (26%) and RQ (13%) BAL QSOs. This could indicate a turbulent accretion process for RL BAL QSOs and for BAL QSOs in general, originating faster outflows detectable as BAL in the

UV-optical spectrum. A high accretion rate should be present to justify these super-Eddington luminosities: this could partially confirm the position occupied by BAL QSOs in the Boroson et al. (2002) diagram.

- We do not find any difference between the mean BLR radius of RL and RQ BAL QSOs, showing similar mean values (481 and 483 light-days). This implies a similar geometry and dynamic for the central region of RL and RQ BAL QSOs.

Chapter 8

Conclusions and future perspectives

"How often have I said to you that
when you have eliminated the impossible,
whatever remains, however improbable,
must be the truth?"

Sherlock Holmes - The Sign of the Four
Sir Arthur Conan Doyle

This thesis discussed the results of an extensive multi-wavelength observational campaign, from Radio to Near-Infrared, aiming at increasing the understanding of nature and origin of Broad Absorption Line Quasars. Using the radio emission as an additional investigation tool, we aimed at testing the different models proposed for BAL QSOs: the evolutionary and the orientation one.

This work started in 2008, after the pilot study from Montenegro-Montes et al. (2008a,b), with the selection of a new sample of RL BAL QSOs, with flux density >30 mJy in the FIRST radio-survey. With these radio-bright list of objects, plus a comparison sample of RL non-BAL QSOs, we planned and performed observations in the radio band, both at medium (kpc-scale) and high (pc-scale) resolution, to constrain the ages, the orientations and the morphological properties of the central radio sources. We used the most important and sensible radio-telescopes, including the VLA, the Effelsberg-100m single dish (see chapter 3 and 4) and continental-scale interferometers like the VLBA and the EVN (see chapter 5).

At the same time we collected data in the mm-wavelength domain, to test the hypothesis of the young ages of BAL QSOs (see chapter 6). We looked for an excess in the mm-band flux densities, probable hint of a redshifted FIR

emission from cold dust, present in young galaxies with an high star-formation rate.

Moreover, we used a sample of optically-bright RL and RQ BAL QSOs to investigate the central kpc of the AGN, looking for differences in size of the BLR or mass of the central black hole (see chapter 7).

All this information seems to confirm that very small difference is present between BAL and non-BAL QSOs, confirming the results presented by various authors in the literature. These objects can have different ages as inferred from the radio emission properties and dust abundance (however not in agreement with the youth scenario), they show different orientations and morphologies (not suggesting an orientation scenario) and the geometrical properties of the central region and central black hole mass are in the normal range found for the QSO population.

The most obvious conclusions arising from these different and heterogeneous findings is that, most probably, the broad absorption lines are not produced by a dusty cocoon being expelled by the central object (otherwise we would see the clear footprint of the grey-body dust emission in the SED), but are likely to be the result of absorption from an outflow, starting from the accretion disk, and with different possible angles with respect to the polar axis. This kind of ejection has been investigated in the last years through theoretical works (Proga & Kurosawa 2009) that successfully modelled the ejection of matter and the collimation of outflows at different angles.

Then BAL outflows should be present at different evolutionary stages of the QSO activity, both in the radio-loud and radio-quiet phase, and seen only when they intercept the line of sight of the observer. This last point would constrain the outflow solid angle to a fraction of steradians, in order to justify the observed fraction of BAL QSOs among the QSO population as an effect of the covering factor. Another hypothesis could be a combination of small solid angles with the sporadic emission of outflows, that would not be always present in the QSO.

Spectroscopy allowed us to find a tentative evidence of over-abundance of super-Eddington objects among BAL QSOs, that could partially confirm the position occupied in the Boroson et al. (2002) diagram.

In summary, the actual knowledge about BAL QSOs is really an image as seen through a negative. It seems we can only state what these objects *are not*, deducing their nature through the exclusion of the improbable.

Future perspectives

There are still some aspects to be explored in different bands, and with the advent of the new generation of radio telescopes new observable windows can be considered to improve our view on BAL QSOs and the AGN population as a whole. Here we report some open questions on BAL QSOs that could find a definitive answer thanks to these new facilities:

- **Are BAL QSOs more common among restarting radio-sources?**
  At low radio frequencies (< 100 MHz) LOFAR will for the first time realise an all-sky survey, with the highest resolution and sensitivity ever achieved. At such frequency, with the capabilities of this array, it will be possible to investigate the presence of very steep-spectrum radio relics, remnants of earlier radio-loud phases.

- **Are physical conditions different in BAL QSOs?**
  With the collected radio data at hand we have already performed further observations to obtain polarization and Rotation Measures of the fainter BAL and non-BAL QSOs of the two samples (EVLA, Effelsberg-100m). With a better statistics it will be possible to test the environment of the AGN and in particular, through Rotation Measures, the amount of magnetized plasma along the line of sight. Moreover, with an accurate radio spectrum a synchrotron aging analysis can be done to test the age of the radio source. This will be easily achievable with the new EVLA capabilities.

- **Have BAL QSOs intrinsically different morphologies?**
  So far, about half of the sample have been observed with the VLBI technique. The completion of pc-scale imaging would be useful to test the central environment and compare the different morphologies with a comparison sample of non-BAL QSOs from catalogues.

- **Is there a faint dust emission?**
  Also the dust detection, performed only for 12 sources, needs more observations to increase statistics and allow a more accurate mass estimation from the grey-body distribution, to be compared with the fraction of dust-rich objects in the QSO population. ALMA has already started to collect data at the highest radio frequencies observable through the atmosphere and will provide the necessary sensibility to detect any faint dust emission. The Sardinia Radio Telescope, now under commissioning, will be useful to detect any high frequency tail of synchrotron emission, thanks to its extended frequency coverage (up to 100 GHz).

- **Are there particular physical conditions in the BAL-producing outflows?**
  Finally, by doing moderate-resolution optical spectroscopy (WHT) of the C IV absorptions in BAL QSOs we can infer properties of the outflows, such as the covering factor of the clouds, column density, number of outflow systems. This information, combined with infrared spectroscopy (to observe Mg II and the Fe II blue bump, already available from TNG), will allow us to compare radio-loud and radio-quiet BAL QSOs in a more complete way.

Thanks to these new observations, combined with the latest catalogues realised in different bands (like the FERMI point-source catalogue in the gamma

band), it will be possible to have a more complete, panchromatic view on the BAL QSO phenomenon, although the results of this thesis already suggests that these objects are not a distinct class of QSOs in the AGN scenario.

Bibliography

Adelman-McCarthy, J.K., Agüeros, M.A., Allam, S.S. et al. 2007, AJ Supplement Series, 172, 2, 634

Allen, J.T., Hewett, P.C., Maddox, N. et al. 2011, MNRAS, 410, 860

Alloin, D., et al. 1995, A&A, 293, 293

Baars, J.W.M., Genzel, R., Pauliny-Toth, I.I.K. et al. 1977, A&A, 61, 99

Baffa C., Comoretto G., Gennari S. et al., 2001, A&A, 378, 722

Barvainis, R., Lehár, J., Birkinshaw, M. et al. 2005, ApJ, 618, 108

Becker, R. H., White, R. L. & Helfand, D. J. 1995, ApJ, 450, 559

Becker, R.H., White, R.L., Gregg, M.D. et al. 2000, ApJ, 538, 72

Becker, R.H., White, R.L., Gregg, M.D. et al. 2001, ApJS, 135, 227

Benn, C.R., Carballo, R., Holt, J. et al. 2005, MNRAS, 360, 1455

Bentz, M.C., Peterson, B.M., Pogge et al. 2006, ApJ, 644, 133

Best, P.N., Rottgering, H.J.A., Bremer, M.N. et al. 1998, MNRAS, 301, L15

Boroson, T.A., 2002, ApJ, 565, 78

Boroson, T., Meyers, K.A., 1992, ApJ, 397, 442

Briggs, F. H., Turnsheck, D. A. & Wolfe M. 1984, ApJ, 287, 549

Bruni G., Mack K.-H., Salerno E., et al., 2012, A&A, (subm.)

Castor, J. I., Abbott, D. C., & Klein, R. I. 1975, ApJ, 195, 157

Cohen, A.S., Lane, W.M., Cotton, W.D. et al. 2007, AJ, 134, 1245

Condon, J. J., Cotton, W. D., Greisen, E.W. et al. 1998, AJ, 115, 1693

Crenshaw, D.M., Kraemer, S.B. & George, I.M., 2002, "Mass outflow in AGN: new perspectives", ASP conference Series, vol. 255

Dallacasa, D., Stanghellini, C., Centoza, M. et al. 2000, A&A, 363, 887

de Bruyn, G., Miley, G., Rengelink, R. et al. 2000, VizieR On-line Data Catalog VIII/62

de Kool, M., 1997, in "Mass Ejection from Active Galactic Nuclei", ASP Conference Series, vol. 128, p. 233

Deller et al., 2011, PASP, 123, 275

de Vries W.H., Becker R.H., White R.L., Helfand D.J., AJ, 127, 2565

Doi, A., Kawaguchi, N., Kono, Y. 2009, PASJ, 61, 6, 1389

Douglas, J.N., Bash, F.N. & Bozyan, F.A. 1996, AJ, 111, 5, 1945

Elvis, M. 2000, ApJ, 545, 63

Elvis, M., Wilkes, B.J., McDowell, J.C. et al. 1994, ApJS, 95, 1

Fanaroff, B.L. & Riley, J.M., 1974, MNRAS, 167, S.C., 31

Fanti, R., Fanti, C., Schilizzi, R. T. et al. 1990, A&A, 231, 333

Feigelson, E. D. & Nelson, P. I. 1985, ApJ, 293, 192

Ficarra, A., Grueff, G. & Tomasetti, G. 1984, A&AS, 59, 255

Gaensler B.M. & Hunstead R.W., 2000, PASA, 17, 72

Gawrónski, M.P. & Kunert-Bajraszewska, M. 2011, PoS (X EVN symposium) 037

Ghosh, K.K. & Punsly, B. 2007, ApJ, 661, 139

Gregg, M.D., Becker, R.H., Brotherton, M.S. et al., 2000, ApJ, 544, 142

Gupta, N., Salter, C. J., Saikia, D. J., Ghosh, T., Jeyakumar, S. 2006, MNRAS, 373, 972

Hewett, P.C. & Foltz, C.B. 2003, AJ, 125, 1784

Hales, S.E.G., Baldwin, J.E. & Warner, P.J. 1988, MNRAS, 234, 919

Hall, P. B., Anderson, S. F., Strauss, M. A. et al. 2002, ApJS, 141, 267

Holt J., Benn C.R., Vigotti M., Pedani M., Carballo R., González-Serrano J.I., Mack K.-H., García B., 2004, MNRAS, 348, 857

Hovatta T., Tornikoski M., Lainela M., Lehto H.J., Valtaoja E., Torniainen I., Aller M.F., Aller H.D., 2007 A&A, 469, 899

Jauncey, D.L., King, E.A., Bignall, H.E. et al., 2003, PASA, 20, 151

Jiang D.R. & Wang T.G., 2003, A&A, 397, L13

Jiang D.R., Wang T.G., 2003, A&A, 397, L13

Kaspi S., Smith P.S., Netzer H., Maoz D., Jannuzi B.T., Giveon U., 2000, ApJ, 533, 631

Kaspi, S., Maoz, D., Netzer, H., Peterson, B. M., Vestergaard, M., & Jannuzi, B. T. 2005, ApJ, 629, 61

Kato, T., Tabara, H., Inoue, M. et al. 1987, Nat, 329, 223

Kelly, B.M., Vestergaard, M., Fan, X. 2010, ApJ, 719, 1315

Klein, U., Mack, K.-H., Gregorini, L. et al. 2003, A&A, 406, 579

Korista K.T., Voit G.M., Morris S.L., Weymann R.J., 1993, ApJS, 88, 357

Kovalev, Y. Y. 1996, in Extragalactic radio sources, ed. R. D. Ekers, C. Fanti, & L. Padrielli., IAU Symp. 175, Kluwer, Dordrecht, p. 95.

Kunert-Bajraszewska M. and Marecki A., 2007, A&A, 391, 246

Kunert-Bajraszewska M., Siemiginowska A., Katarzyński K., Janiuk A., 2009, APJ, 705, 1356

Lípari, S.L. & Terlevich, R.J. 2006, MNRAS, 368, 1011

Liu Y., Jiang D.R., Wang T.G., Xie F.G., 2008, MNRAS, 391, 246

Marscher A.P. & Gear W.K., 1985, ApJ, 298, 114

McLure M.J., Jarvis M.J., 2004, MNRAS, 353, 45

Menou K., et al., 2001, APJ, 561, 645

Mignone, A., Rossi, P., Bodo, G. et al., 2010, MNRAS, 402, 1

Miller, L., Peacock, J.A. & Mead, A.R.G. 1990, MNRAS, 244, 207

Montenegro-Montes, F.M., Mack, K.-H., Vigotti, M. et al. 2008a, MNRAS, 388, 1853 (MM08)

Montenegro-Montes, F.M., Mack, K.-H., Benn, C. et al. 2008b, PoS (IX EVN Symposium) 019

Montenegro-Montes, F.M., Mack, K.-H., Dallacasa, D. et al. 2012 (in prep.)

Morganti, R., 2008, in Extragalactic Jets: Theory and Observation from Radio to Gamma Ray, ed. Rector, T. A., De Young, D. S., Girdwood, Alaska, Astronomical Society of the Pacific Conference Series, Vol. 386, p. 210

Murray, N., Chiang, J., Grossman, S.A., Voit, G.M., 1995, ApJ, 451, 498

O'Dea, C.P & Baum, S.A. 1997, AJ, 113, 148.

O'Dea, C.P. 1998, PASP, 110, 493

Oliva E., 2003, Mem Soc. Astron. It., 74, 118

Omont, A., Beelen, A., Bertoldi, F. et al., 2003, A&A,398, 857

Orienti, M. & Dallacasa, D., 2008, A&A, 477, 807

Orr, M.J.L. & Browne, I.W.A. 1982, MNRAS, 200, 1067

Peterson, B.M. 2004, ApJ, 613, 682

Peterson, B.M., 2011, PoS(NLS1)032

Proga, D., Kurosawa, R., 2002, AIP Conference Proceedings, Vol. 1171, p. 295

Punsly, B. 1999a, ApJ, 527, 609

Punsly, B. 1999b, ApJ, 527, 624

Pollack, L.K., Taylor, G. B. & Zavala, R. T., 2003, ApJ, 589, 733

Priddey, R.S., Gallagher, S.C., Isaak, K.G. et al., 2007, MNRAS, 374, 867

Reichard T.A., Richards G., Hall P., Schneider D., 2003, AJ, 125, 1711

Sadler, E. M., Ricci, R., Ekers, R. D. et al. 2006, MNRAS, 371, 898

Salerno E., Mack K.-H., Bruni G. et al., 2012, (in prep.)

Sameshima H., Kawara K., Matsuoka Y., Oyabu S., Asami N., Ienaka N., 2011, MNRAS, 410, 1018

Sanders D. M., ASP conference series, Vol 284, 2002

Schneider et al. 2005, AJ 130, 367

Schneider, D.P., Hall, P. B., Richards, G. T. et al 2007, AJ, 134, 102

Schneider, D. P., Richards, G.T., Hall P.B. et al., 2010, AJ, 139, 2360

Shen, Y., Richards, G.T., Strauss M.A. et al., 2011, ApJ, 194, 45

Snellen I.A.G., Schilizzi R.T., de Bruyn A.G., Miley G.K., 1998, A&A, 333, 70

Stocke, J.T., Morris, S.L., Weymann, R.J. et al. 1992, ApJ, 396, 487

Taylor, A.R., Stil, J.M. & Sunstrum, C., 2009 ApJ 702, 1230

Torniainen, H., Tornikoski, M., Terasranta, H. et al. 2005, A&A, 435, 839

Tornikoski M., Valtaoja E., Teräsranta H., Lainela M., Bramwell M., Botti L.C.L., 1993, AJ, 105, 1680

Trump, J. R., Hall, P. B., Reichard, T. A. et al. 2006, ApJS, 165, 1

Urry, C.M. and Padovani, P., 1995, PASP, 107, 803

van Breugel, W., Miley, G. & Heckman, T. 1984, AJ, 89, 5

Van der Laan H., 1966, Nature, 211, 1131

Vestergaard M., Peterson B.M., 2006, ApJ, 641, 689

Vestergard, M. & Osmer, P.S. 2009, ApJ, 699, 800

Vigotti, M., Grueff, G., Perley, R. et al. 1989, AJ, 98, 419

Vigotti, M., Vettolani, G., Merighi, R. et al. 1997 A&AS 123, 219

Vigotti, M., Gregorini, L., Klein, U. et al. 1999, VizieR On-line Data Catalog: J/A+AS/139/359

Weymann, R.J., Morris, S.L., Foltz, C.B. et al. 1991, ApJ, 373, 23

White, R. L., Becker, R. H., Gregg, M. D. et al. 1997, American Astronomical Society, 191st AAS Meeting, #103.05; Bulletin of the American Astronomical Society, 29, 1373

Willott, C.J., Rawlings, S., Grimes, J.A., 2003, ApJ, 598, 909

Zavala, R. T. & Taylor, G. B., 2004, ApJ, 612, 749

Zhou, H., Wang, T., Wang, H. et al. 2006, ApJ, 639, 716

Acknowledgements

Getting a PhD is both a professional and a personal experience. During the last 3 years I've met many people, sometimes only for a few days during a school, sometimes for longer periods. Every time it has been amazing to see in other young researchers the same passion for Astronomy, and to feel part of a vibrant community, specially for Radio-Astronomy in these days.

I want to say thank you to my supervisor, Dr. Karl-Heinz Mack, for having encouraged me to give the best during these years, and for having shared with me both professional and personal experiences. Thank you to my advisor, Prof. Daniele Dallacasa, for giving me meaningful suggestions, coming from his vast experience in interferometry. Thank you also to my Spanish advisor, Prof. José Ignacio González-Serrano for supporting me during my stay in Santander, and for introducing me to spectroscopy. I am also grateful to the other components of my research group: Chris Benn, Ruth Carballo, Emma Salerno, Joanne Holt, Francisco Montenegro-Montes and Florencia Jiménez-Luján, for all the suggestions that has improved my thesis work.

In Bologna I shared the most of my time with many friends and colleagues that helped me during hard times, so I want to thank all of them for the nice moments spent together: Arturo, Giulia, Annalisa, Franco, Elisabetta, Francesca, Rossella, Gabriele, Andrea, Viviana, Jeremie, Rosita, Rashmi e Roberto. SID!

During my stay in Spain I met a lot people, and some of them are now my colleagues: Diego, Zayra, Simon, Pier, Daniel, José, Abel, Paki, Serena. Muchas gracias y hasta luego!

Finally, I want to say *goodbye* to my grandfather Giacomo, who passed away last November. He was the first person who introduced me to Astronomy, and who gave me the will to look above and understand the Universe. He could only see the beginning of my career, but from now on he will see the rest from the stars. Grazie!